Department of Physics and Astronomy

University of Heidelberg

Master thesis

in Physics

submitted by

Lisa Ringena

born in Emden

2016

Optimization of ^{39}Ar-ATTA with new Laser System and a Double-Frequency Magneto-Optical Trap

This Master thesis has been carried out by Lisa Ringena

at the

Kirchhoff-Institut für Physik

under the supervision of

Prof. Dr. Markus K. Oberthaler

Optimization of ^{39}Ar-ATTA with new Laser System and a Double-Frequency Magneto-Optical Trap

The Atom Trap Trace Analysis (ATTA) apparatus in Heidelberg offers the unique ability to count the rare argon isotope ^{39}Ar by addressing optical transitions in the atom by laser light of narrow linewidth. The counting method utilizes the high amount of scattering processes in a magneto-optical trap (MOT) for a distinct capture of the desired isotope alone. In the course of this thesis, the design and realization of a new laser system for ATTA will be presented. Measurements conducted with small sample sizes demonstrated the stability and overall performance of the renewed ATTA apparatus. For the second part of this thesis, the MOT was examined under observation of the more abundant isotope ^{38}Ar. In order to maximize the fluorescence signal, the MOT trapping beams need to be near-resonant to the atomic transition which unfortunately results in a disadvantageous capture efficiency. The introduction of a second trapping laser with a stronger red-detuning, overlying the original MOT beams, improves the loading rate of the trap while maintining a high scattering rate for detection. For ^{38}Ar a loading rate enhancement of $\sim$20% compared to the single frequency configuration was achieved.

Optimierung von ^{39}Ar-ATTA mit neuem Laser System und eine Doppel-Frequenz Magneto-Optische Falle

Die Atom Trap Trace Analysis (ATTA) Apperatur in Heidelberg ermöglicht das Zählen des seltenen Argonisotops ^{39}Ar durch das Anregen von optischen Übergängen im Atom mit schmalbandigem Laserlicht. Die genutzte Zählmethode macht sich die hohe Anzahl von Streuprozessen in einer magneto-optischen Falle (MOT) für das eindeutige und alleinige Einfangen des gewünschten Isotops zunutze. Im Verlauf dieser Arbeit wird das Design und die Implementierung eines neuen Lasersystems erläutert. Messungen, die mit Proben kleines Volumens durchgeführt wurden, demonstrieren die Stabilität und Leistungsfähigkeit der erneuerten ATTA Apperatur. Im zweiten Teil dieser Arbeit wurde die MOT, unter Beobachtung des häufigeren Isotops ^{38}Ar, charakterisiert. Zur Erhöhung des Fluoreszenzsignals benötigt man Laserlicht, welches nahe der atomaren Resonanz ist, was jedoch in einer unvorteilhaft niedrigen Einfangeffizienz resultiert. Die zusätzliche Verwendung eines zweiten Lasers mit einer stärkeren Rotverstimmung, welcher die urprünglichen MOT-Strahlen überlagert, erhöht die Laderate der Falle, während die Streurate für die Detektion hoch bleibt. Für ^{38}Ar wurde eine Erhöhung der Laderate von $\sim$20% im Vergleich zur Einzelfrequenz-Konfiguration erzielt.

Contents

1 Preface

Empty your mind, be formless. Shapeless, like water. You put water in a cup, it becomes the cup. You put water in a bottle, it becomes the bottle. You put water in a teapot, it becomes the teapot. Now, water can flow or it can crash. Be water, my friend.

Bruce Lee

Profound knowledge about aquifer systems is the key to a sustainable, ecological and effective water management. Water is the world's most important resource and a deeper understanding of oceanographic stream patterns and groundwater flowing speeds is of public interest and indispensible for a responsible handling of its supply. The dating of water plays a key role in reconstructing anthropogenic influences, residence times in sediments and recharge cycles and is therefore a crucial step to characterize a water sample [1], [2].

Age in this context refers to the timespan during which the sample has been enclosed from air. While in contact with the atmosphere, a gas interchange between the air and water surface is taking place where atmospheric atoms and molecules are incorporated into the water. From a taken water sample this gas can be extracted and examined [3].

Nowadays the analysis of environmental tracers is a standard procedure to obtain information on flow dynamics [5]. Environmental tracers are particles with known concentration in atmosphere or soil, which can be compared to a measured concentration of the sample. Adapted to each requirement of the physical model observed, there is a manifold of different environmental tracers used. Some of them are purely anthropogenic gases like chlorofluorocarbons (CFC's) generated mostly in the 1930's for use in refrigerators, some of them are inherent to the atmosphere, like cosmogenic tracers which are produced by cosmic radiation [6].

Another subgroup are radioactive tracers, whereas their lifetime predicts the application area being roughly 0.1 to 10 times the half-life [7]. Their relative concentration compared to the atmospheric concentration correlates over the lifetime to the age of the sample. Change in concentration of the desired tracer might also be caused by underground production in the sediment and could complicate the dating. One subgroup of radioactive tracers are radioactive isotopes of noble gases. Due to their structure noble gases are chemically inert, ensuring them to have negligible interaction with other particles in the water or sediment [8].

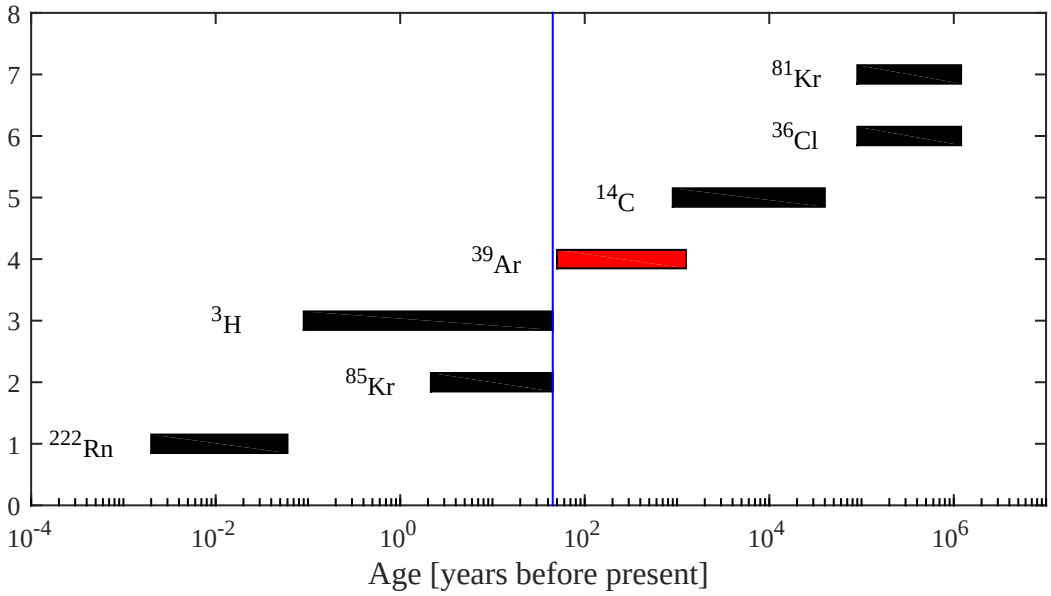

Figure 1.1: Dating ranges of radioisotopes used in water studies. The time window is defined by the specific half-life of the isotope, the blue line indicates the bomb peak marking nuclear bomb test in the 1950's where new radioisotopes were introduced in the atmosphere. ^{39}Ar fills the dating gap between ^{14}C and ^{3}H/^{85}Kr nicely. Figure taken from [4].

The isotope of our choice at the Heidelberg ATTA apparatus is ^{39}Ar which is mainly generated in the atmosphere by ^{40}Ar spallation due to cosmic rays. Its concentration was estimated to be very stable and can therefore be assumed to be constant [9]. Special about this radioisotope is its lifetime of 269 years that offers to date samples with ages in the range of 50 to 1000 years, which is comparable to natural circulation times of oceans [8]. Figure 1.1 shows the dating ranges for the most common radioactive tracers. Radioactive isotopes of argon and krypton are already used for dating ([10], [11], [12]), the challenge here lies in the low relative abundance of these isotopes. One liter of modern water typically contains ∼1000 ^{81}Kr and ∼6500 ^{39}Ar atoms, which is only a tiny fraction of the $\sim 10^{25}$ water molecules [10].

Radioisotopes of noble gases are of arousing interest for many scientific reasearch groups all over the world leading to different approaches towards measuring them. Current experiments implement the differentiation due to the atomic mass, the optical spectrum or the radioactivity of the isotope.

One very peculiar laboratory is the underground lab at the University of Bern at which different radioisotopes are observed with low-level counting (LLC, [13]). LLC seeks to count the decays of the studied isotope and draw conclusions on the age of the sample from the number of decays per time and the lifetime of that isotope. Special about this lab is its location 35 m below ground and its shielding made

from old shipwreck's ^{210}Pb- depleted lead, both in order to decrease the radiation background [13]. Depending on the isotope a measurement can take about three weeks. With this setup the group is able to measure a multitude of tracers, also ^{39}Ar [14]. A major drawback of this measurement scheme is the huge required sample size of up to ∼1000 liters since one liter of modern water produces only 17 ^{39}Ar decays per year [10].

Another approach is separating the isotopes by their mass using accelerator mass spectrometry (AMS). The atoms from the sample are ionized and accelerated to very high energies in the order of hundred MeV to remove ambiguities in seperation of ions with same mass [15]. They are deflected by magnets and counted at the end of the measurement region with a detector. AMS has been applied successfully on ^{81}Kr [16] and ^{39}Ar [10] for groundwater studies. Noble gas isotopes do not form negative ions, therefore positive ions have to be generated different from AMS studies of other tracers. The huge background of the stable isotope ^{39}K complicates the separation from ^{39}Ar significantly and requires the acceleration of the atoms to high energies. Therefore big and costly facilities are needed, making AMS a rather challenging experimental measure [10].

Atom Trap Trace Analysis selects the atoms by their unique optical properties. It makes use of the isotope specific atomic level structure by addressing them with narrowband laser light. This approach requires a cycling transition which can be driven by near resonant laser light. This is used to capture the atom inside a magneto-optical trap (MOT) whereas other atoms experience a neglicable effect [11]. Since an atom needs to scatter many photons in order to be trapped, it is impossible to capture an other isotope of argon. This high selectivity enables ATTA to extinguish the background of abundant isotopes.

2 Motivation

The ATTA apparatus seeks to count single ^{39}Ar atoms inside a sample of argon gas. In order to detect the atoms, atomic transitions, which differ significantly between the isotopes, are specifically addressed by laser beams. However, the scattering of only one photon does not clearly identify the ^{39}Ar atom, because the high amount of other isotopes also scatters single photons with a non zero probability. Single atoms are therefore spatially confined by illumination with laser beams from each direction in a MOT. While being captured, the atoms repeatedly scatter photons from these lasers, which is in this amount only possible for an atom which atomic resonance matches the laser frequency. The probability to be captured inside the trap is therefore zero for other isotopes when the laser light frequency is tuned to address ^{39}Ar.

The scattered light can be detected by a photodiode, a sudden increase of the photodiode signal indicates the capture of one atom. The relative concentration $^{39}\mathrm{Ar}_{\mathrm{sample}}/\mathrm{Ar}_{\mathrm{atmosph.}}$ is then determined by the comparison of the count rates for the sample and an atmospheric reference. A high count rate is desirable as it enables better statistical handling, shorter measurement times and scientific validity. However, the count rate is limited by various effects, so that currently approximately two atoms are captured per hour for an atmospheric sample. Different strategies have been tried and applied in order to increase the count rate for ^{39}Ar (see [17], [18], [19]).

Manipulating the isotopes to enhance the count rate requires a lot of different laser beams at various stages of the apparatus. The optical table of the experiment is spatially seperated from the apparatus so that the lasers and optomechanics are independent from the experimental chamber. After groundwater studies have been successfully conducted at the Heidelberg ATTA apparatus [12] we saw the neccessity of redesigning the whole laser setup since it suffered from instabilities regarding laser powers and frequencies. Beside this, the setup as such evolved over the past five years and could have been built in a more compact and decoupled way. The generation and guidance of the laser beams for the new setup should be one topic of this thesis.

The efficiency of the trapping strongly depends on the properties of the laser beams. Especially the detuning of the laser which is defined as the difference between the atoms internal transition frequency and the laser frequency is a parameter which highly affects the performance of capture and detection. The current choice of detuning is a trade-off between different demands of the experiment. On the one hand a small detuning yields a high scattering rate, since the laser frequency is near the atomic resonance. The fluorescence signal is therefore sufficiently higher and single atoms stick out well distinguishable from the background signal. On the

other hand a small detuning is not adequate to capture atoms of high velocity due to their Doppler shifted atomic transition. Therefore, a high detuning is necessary to trap fast atoms, as will be shown in the course of this thesis. The current detuning of the MOT is a compromise between these two requirements.

An additional set of laser beams with larger detuning from the atomic transition could be helpful to collect fast atoms that would not be captured by the original beams alone. Effectively, the trap would be large and far detuned for fast atoms and small and resonant for slow atoms, therefore fast atoms can be captured and still the scattering rate stays high as soon as the atoms are resonant with the beam of small detuning. The theoretical investigation and experimental application of this two-frequency MOT should be the second topic of this thesis.

3 Fundamentals

Throughout the experiment, atoms are manipulated with laser beams of certain wavelength and power. Each individual beam acts on the atoms differently and various effects can be observed. In this chapter, the behavior of atoms in radiative fields is mathematically described giving an introduction towards the experimental approach. Besides this, the influence of external magnetic fields on the atoms internal energy structure should be discussed, leading towards the capture of atoms.

3.1 Interaction of Atoms with Light

3.1.1 The Rabi Problem

This derivation of the Rabi Problem will mainly be geared to [20]. The root of the time evolution of the atomic system is the time-dependent Schrödinger equation (TDSE)

$$\mathcal{H}\left|\Psi(\vec{r},t)\right\rangle = i\hbar\frac{\partial\left|\Psi(\vec{r},t)\right\rangle}{\partial t} \tag{3.1}$$

with the atomic wavefunction $|\Psi(\vec{r},t)\rangle$ and the electron sited at position $\vec{r}$. Concerning its time dependency, the Hamilton Operator $\mathcal{H}$ is subdivided into the atomic, time-independent part $\mathcal{H}_0$ and the time-dependent part $\mathcal{H}'(t)$ which includes the atom-light interaction, so that $\mathcal{H}(t) = \mathcal{H}_0 + \mathcal{H}'(t)$. The field-free $\mathcal{H}_0$ already gives us a complete set of eigenfunctions $|\Phi_k(\vec{r})\rangle$ with eigenenergies $E_k = \hbar\omega_k$. Due to this, we can express the time-dependent wavefunction $|\Psi(\vec{r},t)\rangle$ as a linear combination of the vectors $|\Phi_k(\vec{r})\rangle$ and introduce the time dependency through the time evolution operator $\mathcal{U}(t) = e^{-i\frac{\mathcal{H}_0}{\hbar}t}$ and the time-dependent coefficients $c_k(t)$

$$\left|\Psi(\vec{r},t)\right\rangle = \sum_k c_k(t)\left|\Phi_k(\vec{r})\right\rangle e^{-i\omega_k t}. \tag{3.2}$$

We can insert this expansion of the wavefunction into eq. 3.1. Multiplication with the complex conjugate of the eigenstate $\langle\Phi_j(\vec{r})|$ and integrating over $\vec{r}$ then yields

$$i\hbar\frac{\mathrm{d}c_j(t)}{\mathrm{d}t} = \sum_k c_k(t)\mathcal{H}'_{jk}(t)e^{i\omega_{jk}t} \tag{3.3}$$

with $\mathcal{H}'_{jk}(t) := \langle\Phi_j|\,\mathcal{H}'(t)\,|\Phi_k\rangle$ and $\omega_{jk} := \omega_j - \omega_k$. This equation fully describes the atom-light system but is unfortunately unsolveable unless approximations are made. For our application of a narrowband laser excitation it is common to make the assumption of a two level system, leaving only the ground state $|g\rangle$ and the

excited state $|e\rangle$ of the atom. This extinguishes all terms in the sum of eq. 3.3 but two and the resulting two coupled ordinary differential equations (ODEs) can be solved directly. Isidor Isaac Rabi (1898-1988 [21]) was the first person to study this problem giving it the name Rabi-problem. In his solution, first the diagonal elements of the matrix $\mathcal{H}'$ are absorbed into $\mathcal{H}_0$, leaving these differential equations for the time-dependent off-diagonal elements

$$\begin{aligned} i\hbar\frac{\mathrm{d}c_g(t)}{\mathrm{d}t} &= c_e(t)\mathcal{H}'_{ge}(t)e^{-i\omega_a t} \\ i\hbar\frac{\mathrm{d}c_e(t)}{\mathrm{d}t} &= c_g(t)\mathcal{H}'_{eg}(t)e^{i\omega_a t} \end{aligned} \tag{3.4}$$

with the atomic resonance frequency $\omega_a = \omega_{eg}$. As we treat the atom-light interaction classically, the Hamiltonian $\mathcal{H}'_{eg}(t)$ is found to be $\mathcal{H}'_{eg}(t) = -e\vec{\mathcal{E}}(\vec{r},t)\cdot\vec{r}$. Here a narrowband laser excitation is considered using the electric field operator

$$\vec{\mathcal{E}}(\vec{r},t) = E_0\hat{\varepsilon}\cos(kz-\omega_l t) \tag{3.5}$$

for a plane wave traveling in positive z-direction with amplitude E_0, frequency ω_l and the unit polarization vector $\hat{\varepsilon}$. $\mathcal{H}'_{eg}(t)$ then forms to

$$\mathcal{H}'_{eg}(t) = \hbar\Omega\cos(kz-\omega_l t) \tag{3.6}$$

as the coupling of light field and atomic system. The strength of this coupling is denoted by the Rabi frequency

$$\Omega := -\frac{eE_0}{\hbar}\langle e|\, r\,|g\rangle\,. \tag{3.7}$$

For this result the dipole approximation has been made, assuming that the electric field stays constant over the spatial integral of $\mathcal{H}'_{eg}(t)$. Due to the scale of a wavelength being several times larger than the expansion of an atom this approximation is valid.

Plugging the new expression of the Hamiltonian into the differential equations in eq. 3.4 yields

$$\begin{aligned} i\hbar\frac{\mathrm{d}c_g(t)}{\mathrm{d}t} &= c_e(t)\hbar\Omega^* cos(\omega_l t)e^{-i\omega_a t} = \frac{\hbar\Omega^*}{2}c_e(t)(e^{i(\omega_l-\omega_a)t}+e^{-i(\omega_l+\omega_a)t}) \\ i\hbar\frac{\mathrm{d}c_e(t)}{\mathrm{d}t} &= c_g(t)\hbar\Omega cos(\omega_l t)e^{-i\omega_a t} = \frac{\hbar\Omega}{2}c_g(t)(e^{-i(\omega_l-\omega_a)t}+e^{i(\omega_l+\omega_a)t}). \end{aligned} \tag{3.8}$$

Considering the high frequency $(\omega_l+\omega_a)$ the $e^{-i(\omega_l+\omega_a)t}$-term oscillates with, it can be neglected when compared the $e^{i(\omega_l-\omega_a)t}$-term (Rotating Wave Approximation). Further we introduce the detuning $\delta = \omega_l - \omega_a$ which will grow important in the course of this thesis. Eq. 3.8 simplifies to

$$\begin{aligned} i\hbar\frac{\mathrm{d}c_g(t)}{\mathrm{d}t} &= \frac{\hbar\Omega^*}{2}c_e(t)e^{i\delta t} \\ i\hbar\frac{\mathrm{d}c_e(t)}{\mathrm{d}t} &= \frac{\hbar\Omega}{2}c_g(t)e^{-i\delta t}. \end{aligned} \tag{3.9}$$

Differentiating the first equation and substituting c_e gives us

$$\frac{\mathrm{d}^2 c_g(t)}{\mathrm{d}^2 t} - i\delta \frac{\mathrm{d}c_g(t)}{\mathrm{d}t} + \frac{\Omega^2}{4} c_g(t) = 0 \tag{3.10}$$

and

$$\frac{\mathrm{d}^2 c_e(t)}{\mathrm{d}^2 t} + i\delta \frac{\mathrm{d}c_e(t)}{\mathrm{d}t} + \frac{\Omega^2}{4} c_e(t) = 0. \tag{3.11}$$

Solving this we obtain

$$c_e(t) = -i\frac{\Omega}{\Omega'} \sin(\frac{\Omega' t}{2}) e^{-i\delta t/2} \tag{3.12}$$

with $\Omega' := \sqrt{\Omega^2 + \delta^2}$ for the intial conditions $c_g(0) = 1$, $c_e(0) = 0$. Squaring the time-dependent coefficients directly yields the probability of the atom to be in the corresponding state. A time evolution of $|c_e(t)|^2$ for different detunings is shown in figure 3.1. We can observe that the probability for the atom to be in $|e\rangle$ oscillates over time and that a higher detuning increases the frequency of this oscillation and lowers its amplitude.

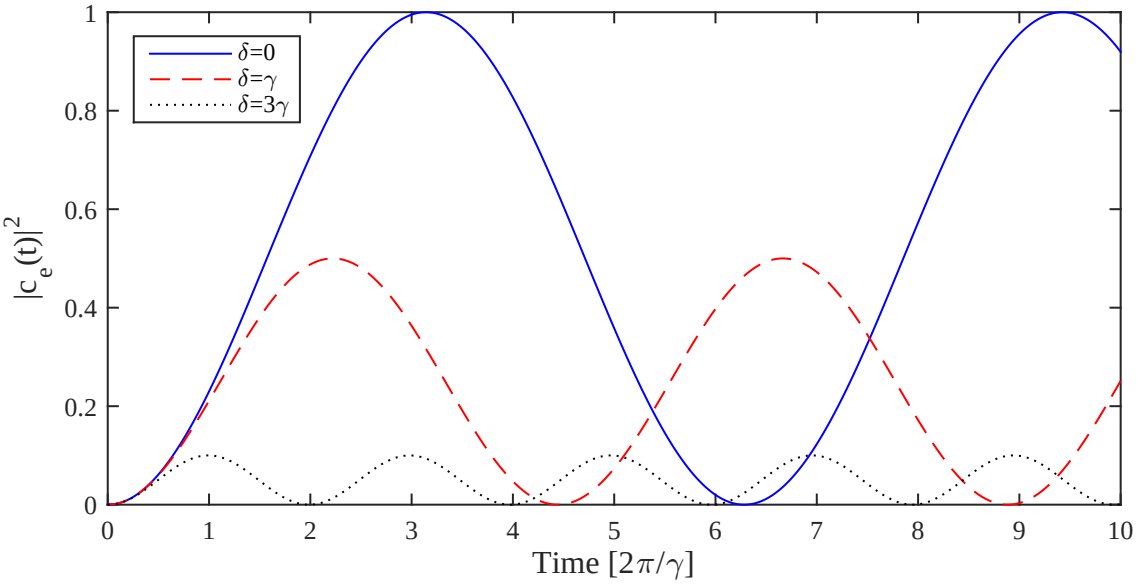

Figure 3.1: Rabi oscillations of the excited state $|e\rangle$ for detunings $\delta = 0$ (solid, blue), γ (dashed, red), 3γ (dotted, black).

3.1.2 The Density Matrix for a Single Laser Beam

Solving the Rabi Problem helps understanding the effect of a narrowband laser excitation on the atom. However, it is not possible to include the effect of spontaneous emission into this picture. With spontaneous emission the system is no longer in a

pure state i.e. in state $|e\rangle$ or $|g\rangle$, but in a mixture of $|e\rangle$ and $|g\rangle$. Another theoretical approach, the density matrix ρ, enables us to handle these mixed states. With all information about our system stored in its wavefunctions $|\Psi_n\rangle$ (n here denotes different pure states), ρ is defined as

$$\rho := \sum_n P_n \left|\Psi_n\right\rangle \left\langle\Psi_n\right| \tag{3.13}$$

with P_n the probability to be in state $|\Psi_n\rangle$. For a pure state only one P_n is not zero and therefore becomes $P_0 = 1$. The density matrix reduces to $\rho = |\Psi_0\rangle \langle\Psi_0|$ [22].

Considering the two-level atom as in the previous section the density matrix will write as

$$\rho = \begin{pmatrix} \rho_{ee} & \rho_{eg} \\ \rho_{ge} & \rho_{gg} \end{pmatrix} = \begin{pmatrix} c_e c_e^* & c_e c_g^* \\ c_g c_e^* & c_g c_g^* \end{pmatrix} \tag{3.14}$$

for the mixed state $|\Psi\rangle = c_e |e\rangle + c_g |g\rangle$ [23].

Now the evolution equations for the coefficients c_i from the Rabi-problem given in eq. 3.9 can be used here to get the evolution of the ρ_{ij}. It follows a differential equation for each matrix element similar to

$$\begin{aligned} \frac{\mathrm{d}\rho_{gg}}{\mathrm{d}t} &= \frac{\mathrm{d}c_g}{\mathrm{d}t} c_g^* + c_g \frac{\mathrm{d}c_g^*}{\mathrm{d}t} \\ &= i\frac{\Omega^*}{2} c_e e^{i\delta t} c_g^* - c_g i \frac{\Omega}{2} c_e^* e^{i\delta t} = i\frac{\Omega^*}{2}\tilde{\rho}_{eg} - i\frac{\Omega}{2}\tilde{\rho}_{ge} \end{aligned} \tag{3.15}$$

with the substitute $\tilde{\rho}_{ge} := \rho_{ge} e^{-i\delta t}$. Spontaneous emission losses can be added seperately as an exponential decay with a rate $\gamma/2$: $(\frac{\mathrm{d}\rho_{eg}}{\mathrm{d}t})_{spont.} = -\gamma/2\ \rho_{eg}$ [20].

We obtain the optical Bloch equations (OBEs):

$$\begin{aligned} \frac{\mathrm{d}\rho_{gg}}{\mathrm{d}t} &= \gamma\rho_{ee} + \frac{i}{2}(\Omega^*\tilde{\rho}_{eg} - \Omega\tilde{\rho}_{ge}) \\ \frac{\mathrm{d}\rho_{ee}}{\mathrm{d}t} &= -\gamma\rho_{ee} + \frac{i}{2}(\Omega\tilde{\rho}_{ge} - \Omega^*\tilde{\rho}_{eg}) \\ \frac{\mathrm{d}\tilde{\rho}_{ge}}{\mathrm{d}t} &= -(\frac{\gamma}{2} + i\delta)\tilde{\rho}_{ge} + \frac{i}{2}\Omega^*(\rho_{ee} - \rho_{gg}) \\ \frac{\mathrm{d}\tilde{\rho}_{eg}}{\mathrm{d}t} &= -(\frac{\gamma}{2} - i\delta)\tilde{\rho}_{eg} + \frac{i}{2}\Omega(\rho_{gg} - \rho_{ee}). \end{aligned} \tag{3.16}$$

Figure 3.2 shows a numerical solution of ρ_{ee}. The Rabi oscillation is now damped due to spontaneous emission and the steady state of $\rho_{ee} = 1/2$ is reached after short times. Introducing the restrictions $\rho_{gg} + \rho_{ee} = 1$ and $\rho_{eg} = \rho_{ge}^*$ and defining the population difference $w := \rho_{gg} - \rho_{ee}$ the OBEs shorten to

$$\begin{aligned} \frac{\mathrm{d}\rho_{eg}}{\mathrm{d}t} &= -(\frac{\gamma}{2} - i\delta)\rho_{eg} + \frac{i\omega\Omega}{2} \\ \frac{\mathrm{d}w}{\mathrm{d}t} &= -\gamma w - i(\Omega\rho_{eg}^* - \Omega^*\rho_{eg}) + \gamma. \end{aligned} \tag{3.17}$$

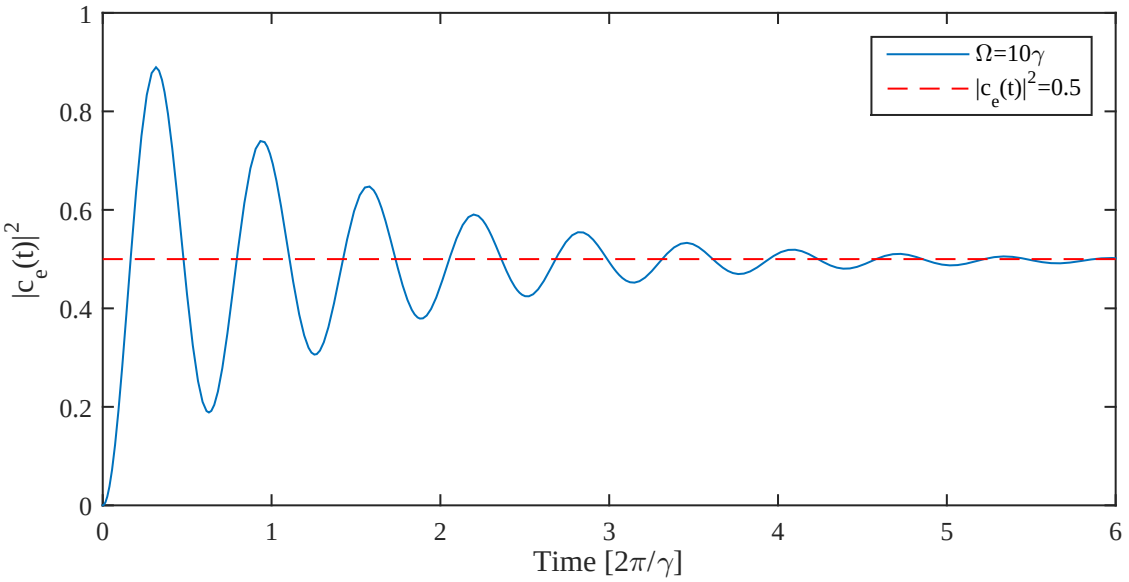

Figure 3.2: The solid (blue) curve shows the solution of a numerical calculation of ρ_{ee} with spontaneous emission included (from eq. 3.16). Here $\delta = 0$ and $\Omega = 10\gamma$ were chosen. The dotted (red) line displays the stationary solution $\rho_{ee} = 0.5$ which is reached after the oscillations of the solid curve are fully damped.

Setting all time derivatives to zero the steady state solution is found to be

$$w = \frac{1}{1+s} \qquad \text{and} \qquad s := \frac{2|\Omega|^2}{\gamma^2(1+(\frac{2\delta}{\gamma})^2)} := \frac{s_0}{1+(\frac{2\delta}{\gamma})^2} \tag{3.18}$$

with the newly defined saturation parameter s. The value of s can be calculated from the saturation intensity I_s or the on-resonance saturation parameter s_0

$$s_0 := \frac{2|\Omega|^2}{\gamma^2} = \frac{I}{I_s} \qquad \text{and} \qquad I_s := \frac{\pi h c}{3\lambda^3 \tau}. \tag{3.19}$$

With this we can finally derive the desired total scattering rate γ_p which is defined as

$$\gamma_p = \gamma\rho_{ee} = \frac{\gamma}{2}(1-w) = \gamma\frac{s_0/2}{1+s_0+(\frac{2\delta}{\gamma})^2}. \tag{3.20}$$

This derivation was mainly after [20]. The scattering rate is an important result at this point, since it gives a define number of how many absorption and emission cycles are driven by the light per time. During the course of this chapter this rate will be further used.

3.1.3 Density Matrix for Interaction with Two Laser Beams

During the course of this chapter, light generated forces acting on the atoms will be introduced and discussed. The principle of ATTA is based on these forces, whereas their optimal use depends on the choice of laser frequency and power. By addressing the atom with two different laser beams at the same time we might obtain forces which are more suited for our application than those a single laser beam would produce. This is the reason why the derivation of the scattering rate for the interaction with two laser beams is of interest for us.

The superpostion of two independent laser beams with each frequency tuned to drive the $|g\rangle \rightarrow |e\rangle$ transition has influence on the scattering rate. Up to eq. 3.9 this double frequency case is similar to that for the single laser frequency since we again examine a two-level system. The difference to the previous calculations lies in an additional interaction term. This needs to be added to the term for the single frequency interaction with the light frequency ω_{l1} and Rabi frequency Ω_1 in eq. 3.9. The second laser beam has a light frequency of ω_{l2} and Rabi frequency Ω_2. The resulting ODEs derived from 3.9 are

$$\begin{aligned} i\hbar\frac{\mathrm{d}c_g}{\mathrm{d}t} &= \frac{\hbar\Omega_1^*}{2}c_e e^{i\delta_1 t} + \frac{\hbar\Omega_2^*}{2}c_e e^{i\delta_2 t} \\ i\hbar\frac{\mathrm{d}c_e}{\mathrm{d}t} &= \frac{\hbar\Omega_1}{2}c_g e^{-i\delta_1 t} + \frac{\hbar\Omega_2}{2}c_g e^{-i\delta_2 t} \end{aligned} \tag{3.21}$$

where Rotation Wave Approximation has already been performed. Each beam i brings about a detuning $\delta_i = \omega_{li} - \omega_a$. Using the definition of the density matrix given in eq3.14, we can derive expressions for the matrix elements by inserting the coefficients from eq. 3.21:

$$\begin{aligned} &\frac{\mathrm{d}\rho_{gg}}{\mathrm{d}t} = \frac{\mathrm{d}c_g}{\mathrm{d}t}c_g^* + c_g\frac{\mathrm{d}c_g^*}{\mathrm{d}t} \\ \Leftrightarrow\ &\frac{\mathrm{d}\rho_{gg}}{\mathrm{d}t} = \frac{i}{2}[(\Omega_1^* e^{i\delta_1 t} + \Omega_2^* e^{i\delta_2 t})\rho_{eg} - (\Omega_1 e^{-i\delta_1 t} + \Omega_2 e^{-i\delta_2 t})\rho_{ge}] \end{aligned}$$

$$\begin{aligned} \frac{\mathrm{d}\rho_{ee}}{\mathrm{d}t} &= -\frac{i}{2}[(\Omega_1^* e^{i\delta_1 t} + \Omega_2^* e^{i\delta_2 t})\rho_{eg} - (\Omega_1 e^{-i\delta_1 t} + \Omega_2 e^{-i\delta_2 t})\rho_{ge}] \\ \frac{\mathrm{d}\rho_{ge}}{\mathrm{d}t} &= \frac{i}{2}[\Omega_1^* e^{i\delta_1 t}(\rho_{ee} - \rho_{gg}) + \Omega_2^* e^{i\delta_2 t}(\rho_{ee} - \rho_{gg})] \\ \frac{\mathrm{d}\rho_{eg}}{\mathrm{d}t} &= (\frac{\mathrm{d}\rho_{ge}}{\mathrm{d}t})^*. \end{aligned} \tag{3.22}$$

In order to obtain a result comparable to the OBEs we further simplify eq. 3.22 with defining a substitute to ρ_{ge} comparable to the previous $\tilde{\rho}_{ge}$. The new replacement is defined as

$$\begin{aligned} \tilde{\rho}_{ge} &:= \rho_{ge}(\Omega_1' e^{-i\delta_1 t} + \Omega_2' e^{-i\delta_2 t}) \\ \text{with} \qquad \Omega_i' &:= \frac{\Omega_i}{\Omega} \qquad \text{and} \qquad \Omega := \Omega_1 + \Omega_2. \end{aligned} \tag{3.23}$$

Using these substitutes and including spontaneous emission we get expressions which look exactly like the OBEs in eq. 3.16:

$$\begin{aligned}\frac{\mathrm{d}\rho_{gg}}{\mathrm{d}t} &= \gamma\rho_{ee} + \frac{i}{2}(\Omega^*\tilde{\rho}_{eg} - \Omega\tilde{\rho}_{ge}) \\ \frac{\mathrm{d}\rho_{ee}}{\mathrm{d}t} &= -\gamma\rho_{ee} + \frac{i}{2}(\Omega\tilde{\rho}_{ge} - \Omega^*\tilde{\rho}_{eg}).\end{aligned} \tag{3.24}$$

The time-derivative of $\tilde{\rho}_{eg}$

$$\frac{\mathrm{d}\tilde{\rho}_{eg}}{\mathrm{d}t} = \frac{\mathrm{d}\rho_{eg}}{\mathrm{d}t}(\Omega_1'^* e^{-i\delta_1 t} + \Omega_2'^* e^{i\delta_2 t}) + \rho_{eg}(\Omega_1'^* i\delta_1 e^{i\delta_1 t} + \Omega_2'^* i\delta_2 e^{i\delta_2 t}) \tag{3.25}$$

is more complicated, therefore we introduce $\Delta := \delta_1 - \delta_2$ as the difference between the two detunings and again the population difference $w := \rho_{gg} - \rho_{ee}$. Eq. 3.24 can now be rewritten in terms of w

$$\frac{\mathrm{d}w}{\mathrm{d}t} = -\gamma w + \gamma - i(\Omega\tilde{\rho}_{eg}^* - \Omega^*\tilde{\rho}_{eg}) \tag{3.26}$$

and

$$\frac{\mathrm{d}\tilde{\rho}_{eg}}{\mathrm{d}t} = -\frac{\gamma}{2}\tilde{\rho}_{eg} + \frac{iw}{2\Omega^*}[\Omega_1^2 + \Omega_2^2 + 2\Omega_1\Omega_2^* cos(\Delta t)] + \tilde{\rho}_{eg}\frac{i\delta_1\Omega_1'^* e^{i\delta_1 t} + i\delta_2\Omega_2'^* e^{i\delta_2 t}}{\Omega_1'^* e^{i\delta_1 t} + \Omega_2'^* e^{i\delta_2 t}} \tag{3.27}$$

with $\rho_{ee} + \rho_{gg} = 1$. These differential equations are already much more condensed and can be solved. Again we are searching for a steady state solution in which all time derivatives are zero. Solving Eq. 3.27 for $\tilde{\rho}_{eg}$ then yields

$$\tilde{\rho}_{eg} = \frac{iw(\Omega_1^2 + \Omega_2^2 + 2\Omega_1\Omega_2^*\cos(\Delta t))}{2\Omega^*(\frac{\gamma}{2} - \frac{i\delta_1\Omega_1'^* e^{i\delta_1 t} + i\delta_2\Omega_2'^* e^{i\delta_2 t}}{\Omega_1'^* e^{i\delta_1 t} + \Omega_2'^* e^{i\delta_2 t}})}. \tag{3.28}$$

This result is plugged into eq. 3.26 for the population difference and we can obtain an expression for w

$$w(t) = \frac{1}{1 + s(t)} \tag{3.29}$$

with

$$s(t) = \tag{3.30}$$
$$\frac{1}{\gamma}\left[\frac{(\Omega_1^2 + \Omega_2^2 + 2\Omega_1\Omega_2^* cos(\Delta t))[\gamma - \frac{i\delta_1\Omega_1'^* e^{i\delta_1 t} + i\delta_2\Omega_2'^* e^{i\delta_2 t}}{\Omega_1'^* e^{i\delta_1 t} + \Omega_2'^* e^{i\delta_2 t}} - \frac{i\delta_1\Omega_1' e^{-i\delta_1 t} + i\delta_2\Omega_2' e^{-i\delta_2 t}}{\Omega_1' e^{-i\delta_1 t} + \Omega_2' e^{-i\delta_2 t}}]}{2(\frac{\gamma}{2} + \frac{i\delta_1\Omega_1' e^{-i\delta_1 t} + i\delta_2\Omega_2' e^{-i\delta_2 t}}{\Omega_1' e^{-i\delta_1 t} + \Omega_2' e^{-i\delta_2 t}})(\frac{\gamma}{2} - \frac{i\delta_1\Omega_1'^* e^{i\delta_1 t} + i\delta_2\Omega_2'^* e^{i\delta_2 t}}{\Omega_1'^* e^{i\delta_1 t} + \Omega_2'^* e^{i\delta_2 t}})}\right]$$

It can easily be derived that $\rho_{ee} = \frac{1}{2}(1-w) = \frac{s}{2(1+s)}$ and after some rearranging this yields the total scattering rate:

$$\gamma_p(t) = \gamma\rho_{ee}(t) = \frac{[s_{01} + s_{02} + 2s'\cos(\Delta t) + \frac{\Delta}{\gamma}s'\sin(\Delta t)]\gamma/2}{1 + s_{01} + s_{02} + \frac{4}{\gamma^2}\frac{s_{01}\delta_1^2 + s_{02}\delta_2^2 + 2s'\delta_1\delta_2\cos(\Delta t) + \gamma\Delta s'\sin(\Delta t)}{s_{01} + s_{02} + 2s'\cos(\Delta t)} + 2s'\cos(\Delta t) + \frac{\Delta}{\gamma}s'\sin(\Delta t)}. \tag{3.31}$$

The on-resonance saturation parameter for the laser beams is given by $s_{01} = \frac{I_1}{I_s}$ and $s_{02} = \frac{I_2}{I_s}$ respectively. For simplicity the variable $s' = \sqrt{s_{01} s_{02}}$ was introduced in the above equation.

Eq. 3.31 can be simplified for the case of two beams of the same intensity $I_1 = I_2$ and therefore $\Omega_1 = \Omega_2$. The on-resonance saturation parameters are equal $s_{01} = s_{02}$ and we obtain this scattering rate:

$$\gamma_p(t) = \frac{[2s_{01}(1 + \cos(\Delta t)) + \frac{\Delta}{\gamma} s_{01} \sin(\Delta t)]\gamma/2}{1 + 2s_{01}[1 + \cos(\Delta t) + \frac{\Delta}{2\gamma} \sin(\Delta t)] + \frac{4}{\gamma^2} \frac{\delta_1^2 + \delta_2^2 + 2\delta_1\delta_2 \cos(\Delta t) + \gamma\Delta \sin(\Delta t)}{2 + 2\cos(\Delta t)}}. \quad (3.32)$$

For the special case of two equal detunings, we end up with the expected scattering rate for a single laser beam

$$\gamma_p = \frac{4s_{01}\gamma/2}{1 + 4s_{01} + \frac{4}{\gamma^2}\delta_1^2} = \frac{s_0\gamma/2}{1 + s_0 + (\frac{2\delta}{\gamma})^2}. \quad (3.33)$$

since $s_0 = 2\Omega^2/\gamma^2 = 2[2\Omega_1]^2/\gamma^2 = 8\Omega_1^2/\gamma^2 = 4s_{01}$.

The general form for the scattering rate in eq. 3.31 can be confusing at first sight, but splitting the terms might help understanding the physics behind it.

$$\gamma_p = \frac{[s_{01} + s_{02}]\gamma/2}{1 + s_{01} + s_{02} + \frac{4}{\gamma^2} \frac{s_{01}\delta_1^2 + s_{02}\delta_2^2}{s_{01} + s_{02}}}$$

This term of the scattering rate in eq. 3.16 looks very similar to the scattering rate for the single laser frequency case. It can be obtained from eq. 3.20 with a saturation parameter $s = s_{01} + s_{02}$ and a detuning defined by $\delta^2 = \frac{s_{01}\delta_1^2 + s_{02}\delta_2^2}{s_{01} + s_{02}}$ which might be seen as an addition of δ_1 and δ_2 weighted by the corresponding intensities and divided by the total intensity. The scattering rate increases with power until it saturates and it decreases with the detuning δ, similar to the single frequency case.

$$\gamma_p(t) = \frac{[s_{01} + s_{02} + 2s' \cos(\Delta t)]\gamma/2}{1 + s_{01} + s_{02} + 2s' \cos(\Delta t) + \frac{4}{\gamma^2} \frac{s_{01}\delta_1^2 + s_{02}\delta_2^2 + 2s'\delta_1\delta_2 \cos(\Delta t)}{s_{01} + s_{02} + 2s' \cos(\Delta t)}}$$

Considering the cosinus part additionally, the saturation intensity in the numerator becomes a term which strongly reminds of interference effects in classical optics. Leaving behind the $\gamma/2$ we obtain $s_{01} + s_{02} + 2\sqrt{s_{01} s_{02}} \cos(\Delta t)$ which looks identical to the interference term for two laser beams with intensitiy s_{01}, s_{02} and phase shift Δ. Besides the power, the detuning is also affected by the interference and δ gains an additional term depending on the phase $\Delta = \delta_1 - \delta_2$.

$$\frac{\frac{\Delta}{\gamma} s' \sin(\Delta t)\gamma/2}{\frac{\Delta}{\gamma} s' \sin(\Delta t) + \frac{4}{\gamma^2} \frac{\gamma\Delta s' \sin(\Delta t)}{s_{01} + s_{02} + 2s' \cos(\Delta t)}}$$

This term seems to be an additional interference term affecting power and detuning differently. For the saturation intensity the interference depends on the scaling

factor Δ/γ, which is in the order of one, whereas the detuning changes with the factor $\gamma \cdot \Delta$ which is $\sim 10^{-12}$ and therefore comparable to the other terms for the detuning.

It is important to note that the sinus and cosinus terms in eq. 3.31 are varying in time. The oscillations are in the order of $\Delta \approx 10$ MHz and therefore comparable to γ. As the atom undergoes many scattering processes during the interaction with the laser, we can neglect the oscillating terms of the scattering rate. The resulting time-independent scattering rate for the double frequency case writes as

$$\gamma_p = \frac{[s_{01} + s_{02}]\gamma/2}{1 + s_{01} + s_{02} + \frac{4}{\gamma^2}\frac{s_{01}\delta_1^2 + s_{02}\delta_2^2}{s_{01}+s_{02}}}. \tag{3.34}$$

3.2 Light Generated Forces

Deriving the scattering rates for the single and double laser detuning case was the first step towards determination of the laser induced forces acting on the atoms. As we would like to specifically address atoms by their optical properties, we want to examine which effects might affect these properties and how we can make use of those.

Each photon carries a momentum given by $\vec{p} = \hbar\vec{k}$ that is transferred on the atom in the absorption process. The atom is converted to the excited state and stays there until it deexcites by emission of another photon. In the case of spontaneous emission this radiation is distributed randomly over all spatial directions. Therefore the averaged recoil due to emission becomes zero for many cycles. However, as the momentum transfer direction for the absorbed photons is defined by the propagation direction $\vec{k}$ of the laser light a net force $\vec{F}$ can be observed:

$$\vec{F} = \hbar\vec{k}\gamma\rho_{ee}. \tag{3.35}$$

The magnitude of this force is denoted by the number of absorption-emission cycles happening per time given by the previously calculated scattering rate.
For the general case of one laser frequency we can rewrite eq. 3.35 with eq. 3.20:

$$\vec{F} = \hbar\vec{k}\gamma\frac{s_0/2}{1 + s_0 + (\frac{2\delta}{\gamma})^2}. \tag{3.36}$$

It is important to note that δ refers to the detuning between the laser frequency the atom experiences and the internal resonance frequency of the transition, therefore effects that might shift any of these frequencies need to be considered.

Doppler Shift

Atoms entering the apparatus through a source of high temperature have a broad velocity spread inside the chamber. The Doppler effect causes a frequency shift δ_D

dependent on the relative velocity between laser and atom. In the atom's rest frame the laser frequency appears to be shifted by

$$2\pi \cdot \delta_D = -\vec{k} \cdot \vec{v} \tag{3.37}$$

with the atom's velocity $\vec{v}$ and the wavevektor $\vec{k}$ [24].

Zeeman Shift

Regarding the total angular momentum, whether it might be $\vec{L}$, $\vec{J}$ or $\vec{F}$, each atom carries an intrinsic magnetic moment $\vec{\mu}$ which depends on the corresponding quantum number via $\vec{\mu}_J = -\mu_B g_J \vec{J}/\hbar$ with the Landé-factor g_J and the Bohr magneton μ_B (we take $\vec{\mu}_J$ as substitute for any magnetic moment $\vec{\mu}_{L,J,F}$). Under the presence of an external magnetic field $\vec{B}$ the magnetic moment $\vec{\mu}_J$ experiences a torgue $\vec{M} = \vec{\mu}_J \times \vec{B}$ which relates to a potential energy gain in the vicinity of this magnetic field. This is the so-called Zeeman effect.

For an external B-field in z-direction $\vec{\mu}_J$ can only have discrete projections on the z-axis which are denoted by the quantum number m_J. Therefore the z-component of the magnetic moment simplifies to $(\mu_J)_z = -\mu_B g_J m_J$ and the energy gain can be written as

$$\Delta E(J, m_J) = -(\mu_J)_z \cdot B = \mu_B g_J m_J \cdot B \tag{3.38}$$

whereas the derivation can be found in [25] or [26]. Since we often consider only energy differences between states we can use eq. 3.38 to calculate the detuning of a transition from $|g\rangle$ to $|e\rangle$ due to Zeeman splitting as

$$\delta_Z = \frac{1}{\hbar}[\Delta E(J_e, m_{J_e}) - \Delta E(J_g, m_{J_g})] = \mu_B(g_e m_e - g_g m_g)\frac{B}{\hbar} =: \frac{\mu'}{\hbar}B. \tag{3.39}$$

This result shows that with the Zeeman effect it is possible to introduce a detuning depending on an external field.

3.2.1 Optical Molasses

The in eq. 3.36 displayed force is commonly used for the manipulation of atoms. Mostly more than one laser beam has to be introduced, resulting in more complex effects. Considering a case in which the laser power is small enough, an atom might be excited by a laser beam but cannot be deexcited by stimulated emission due to another beam. This restriction to low powers enables us to calculate the total force acting on an atom by addition of the forces introduced by each laser beam.

In one dimension the total force on an atom of velocity $\vec{v}$ due to illumination by two counterpropagating laser beams with wavevectors $\vec{k}$ and $-\vec{k}$ can therefore be

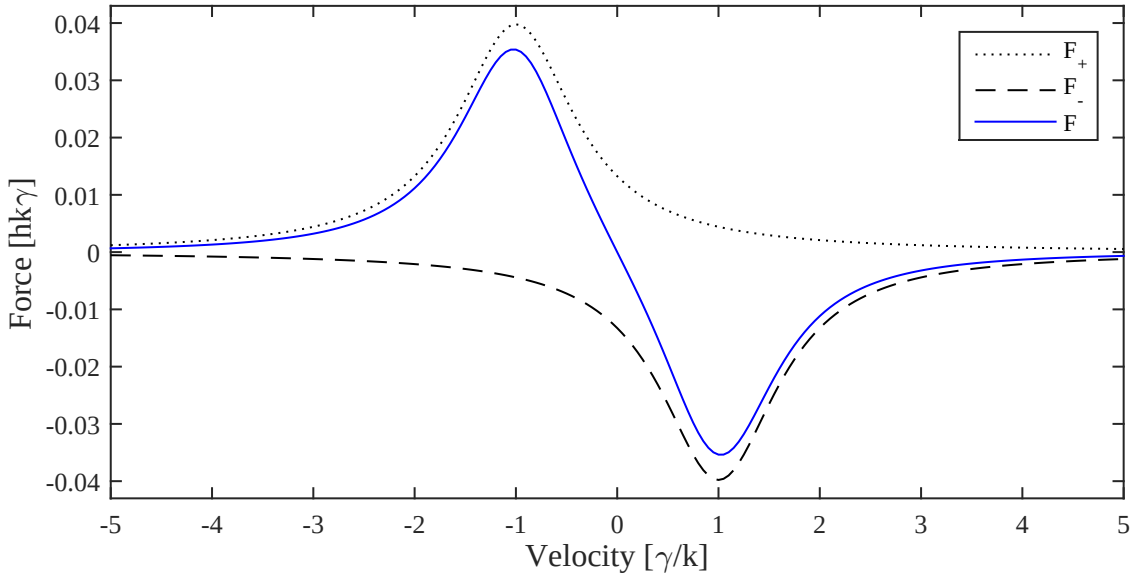

Figure 3.3: Forces on the atom in the one dimensional optical molasses depending on its velocity. Shown are the forces for the two counterpropagating laser beams F_+ (dotted) and F_- (dashed) for $\delta = \gamma$ and $s_0 = 1$. The solid (blue) line displays the sum of the two.

derived from eq. 3.36 to be

$$\begin{aligned}\vec{F} =& \vec{F_+} + \vec{F_-} \\ =& \frac{\gamma\hbar\vec{k}s_0}{2}\left[\frac{1}{1+s_0+(2(\delta-\vec{k}\cdot\vec{v})/\gamma)^2} - \frac{1}{1+s_0+(2(\delta+\vec{k}\cdot\vec{v})/\gamma)^2}\right]\end{aligned} \tag{3.40}$$

which can be approximated by

$$\vec{F} \approx \frac{8\hbar k^2 \delta s_0 \vec{v}}{\gamma(1+s_0+(2\delta/\gamma)^2)^2} := -\beta\vec{v}. \tag{3.41}$$

Cooling in one dimension can be realized by choosing a negative detuning $\delta < 0$. This results in a damping force for the atoms in the dimension of $\vec{k}$, since atoms with a non zero velocity interact stronger with the laser beam which propagation direction opposes their propagation direction. This setup is therefore called optical molasses (OM) and the used principle Doppler cooling. A plot of the force can be seen in figure 3.3. The force $\vec{F}$ is approximately linear for $|\vec{v}| < \gamma/k$ in this case. For comparison of OM performance we define the capture velocity v_c as the highest velocity which can be cooled.[1] In figure 3.3 we can estimate the capture velocity to

[1] The term 'capture velocity' might be misleading in the context of an OM since this system does not provide capture of atoms but rather their cooling. The term is defined here since it is denoted by the light forces, but it only applies in its actual sense for the magneto optical trap which is introduced later.

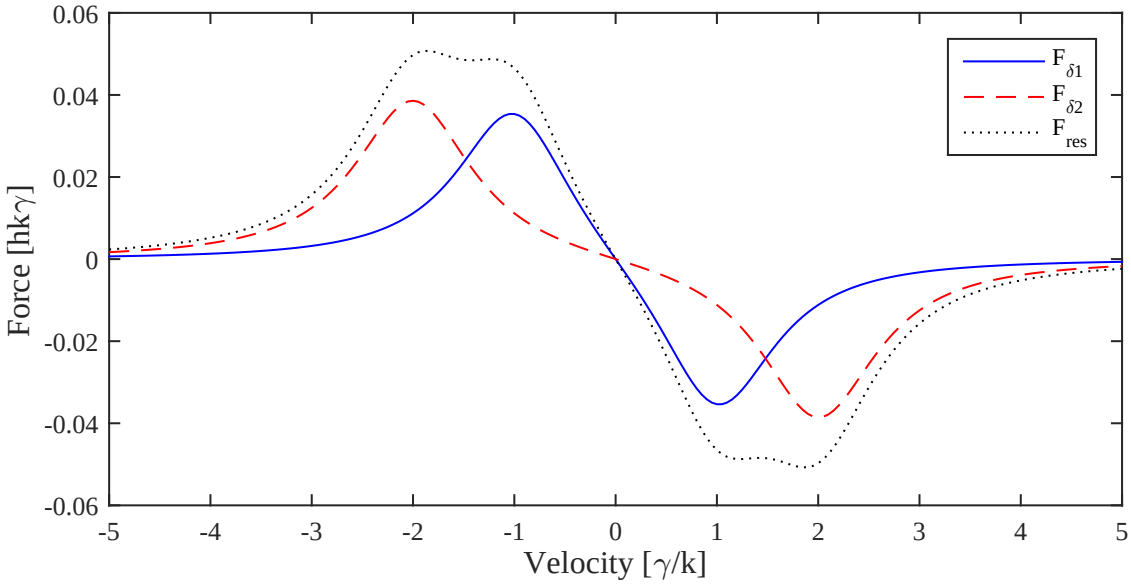

Figure 3.4: Force on the atom in 1D OM depending on its velocity. Previously calcualted force with $\delta_1 = \gamma$ is represented by the solid (blue) curve ($F_{\delta 1}$). The force $F_{\delta 2}$ corresponding to two counterpropagating laser beams with a detuning of $\delta_2 = 2\gamma$ is shown by the dashed (red) curve. The addition of the two yields the dotted (black) curve for F_{res}.

be $v_c = \gamma/k$.

The shape of the curve depends strongly on the detuning δ as can be seen in figure 3.4. In this figure the force due to a higher detuned OM with $\delta_2 = 2\gamma$ is displayed by the dashed (red) curve. The slope at $v = 0$ is not as steep as for $\delta_1 = \gamma$ (solid curve) but the capture velocity is higher. Shown by the dotted (black) curve is the force resulting from an addition of the OM with small detuning and the twice as far detuned OM.

This result should motivate the introduction of a second farer detuned trapping laser beam into the OM as it enables the increase of the capture velocity. The optical molasses extended to three dimensions enables us to cool atoms inside it but not to restore cold atoms into the center, therefore the atoms are not trapped [20].

3.2.2 Principle of a Magneto-Optical Trap

A magneto-optical trap (MOT) uses the cooling force of an optical molasses and superposes it with a position dependent energy shift. It harnesses the previously introduced frequency shifts resulting in a velocity and position selective force which enables trapping. In order to understand the underlying principle it is helpful to reduce the trap to one dimension first.

A constant field gradient is realized by an external magnetic field with a zero-

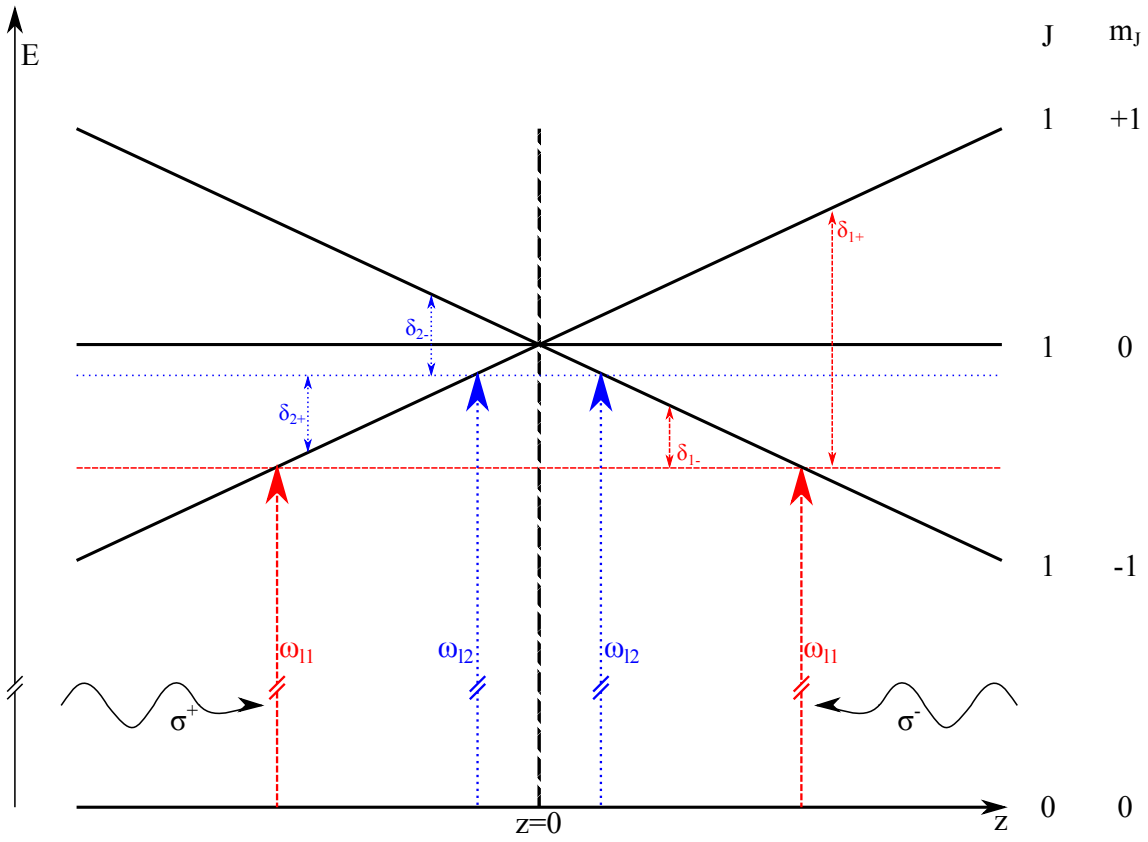

Figure 3.5: Principle of a MOT reduced to 1D. The solid lines represent the magnetic substates, splitted up in energy by the magnetic field gradient due to the Zeeman effect. The two thin horizontal lines display the two laser frequencies as they are seen by an atom at rest in the trap's center. The dotted (blue) line corresponds to a small detuning close to the atoms resonance. Two dotted (blue) arrows from the ground to the excited state show, at which position the atom becomes resonant with the laser light. Small dotted (blue) arrows from the laser frequency to the energy of the excited state represent the detunings δ_{1+} and δ_{1-}. Same for the other laser beam shown by the dashed (red) lines and arrows. Here the laser frequency ω_{l2} is farer detuned. Atoms at a position $z > 0$ are closer to resonance with the σ^- beam and therefore experience a force towards the center of the trap.

crossing at the center of the trap. The Zeeman effect therefore causes the energy levels of the observed atom to split up depending on position. As an example we take a look at a transition $|g\rangle \rightarrow |e\rangle$ with $J_g = 0$ and $J_e = 1$. The excited level will under presence of the magnetic field split up into its substates denoted by m_0, m_1 and m_{-1}, the ground state remains unchanged since $m_g = m_0$ is the only substate and the energy shift is zero for this state.

Additionally two red-detuned, counterpropagating lasers aim to excite the atoms

to $|e\rangle$ serving as the optical molasses. The polarization of the beams is fixed to σ^+ for one and σ^- for the opposing beam. Since the polarization of the light denotes the transition which can be driven ($\Delta m = -1$ for σ^--light and $\Delta m = +1$ for σ^+-light) the laser particulary addresses atoms which are counterpropagating the direction of light and therefore gives them a momentum kick towards the center.

Figure 3.5 shows the principle of a 1D MOT. In this figure a second farer detuned laser beam is introduced into the MOT as well. This laser becomes resonant with the atoms at farer distances of the center (or higher velocities).

A confinement of the atoms inside the center is achieved. In order to evaluate the force on each atom in the MOT all frequency shifts have to be taken into account. Comparable to the optical molasses, two forces corresponding to the two laser beams act on the atom (single frequency case), yielding

$$\vec{F} = \vec{F_+} + \vec{F_-} \tag{3.42}$$

with

$$\vec{F_\pm} = \hbar\vec{k}\gamma\frac{s_0/2}{1 + s_0 + (\frac{2\delta_\pm}{\gamma})^2}. \tag{3.43}$$

The total detuning $\delta_\pm$ can be split up into δ_D and δ_Z:

$$\delta_\pm = \delta + \delta_{D\pm} + \delta_{Z\pm} = \delta \mp \vec{k}\cdot\vec{v} \pm \frac{\mu'}{\hbar}B \tag{3.44}$$

Depending on the choice of laser beam the atoms experience a deceleration and can effectively be cooled. Expanding this to three dimensions, three orthogonal laser beams pairs intersect in the center and two copper coils in anti-helmholtz configuration generate a quadrupole magnetic field. More information on these traps and their setup can be found in [27],[28] or [20].

For the double frequency case the force in eq. 3.43 is obtained with the scattering rate of eq. 3.31 or eq. 3.34.

Similar to the approximation in eq. 3.41 we can obtain an expression for the force in eq. 3.43

$$\vec{F} = -\beta\vec{v} - \kappa\vec{r} \qquad \text{and} \qquad \kappa = \frac{\mu'}{\hbar k}\frac{\partial B}{\partial x}\cdot\beta \tag{3.45}$$

with κ being the damping coefficient for the position $\vec{r}$. Taking a closer look on this approximation it represents a harmonic oscillator with the spring constant κ and the damping rate $\Gamma = \beta/m$. The oscillation frequency is given by $\omega = \sqrt{\kappa/m}$.

We can now classify the behaviour of our trap by comparing ω and Γ. Typical values for our system are damping rates of $\Gamma \sim 100$ kHz and oscillation frequencies ω of a few kHz. Like in an ordinary harmonic oscillator the motion of the atoms is overdamped if $\Gamma > \omega$ resulting in a rapid decay into the steady state without oscillations. For our application this would stand for a fast damping of the atom's motion into the center of the MOT without oscillation towards the outskirts of the trapping region.

Furthermore the trap can be characterized regarding its performance in capturing. The capture efficiency of a MOT is defined as the ratio of atoms being trapped inside it over the number of atoms passing the trap. In most applications a high capture efficiency is desirable.

Besides its capture efficiency the capture radius is a variable which mainly dictates the performance of a MOT. It should give a quantity over which spatial size the MOT forces extend. In [4] this value was defined as the position where the force drops almost to zero for atoms at rest. This can be visualized as the maximum distance an atom of zero velocity can have in order to still be trapped by the MOT.

The size of the trapped cloud deviates from the capture range and can be estimated by its temperature via

$$k_B T = m v_{rms}^2 = \kappa z_{rms}^2, \tag{3.46}$$

whereas the minimum temperature is given by the recoil temperature $T = \frac{\hbar^2 k^2}{2mk_B}$. The cloud has therefore a minimum size of

$$z_{rms,min}^2 = \frac{\hbar^2 k\gamma}{16 m\mu' A} \frac{(1+s_0+(2\delta/\gamma)^2)^2}{\delta s_0} \sim \frac{(1+s_0+(2\delta/\gamma)^2)^2}{\delta s_0} \tag{3.47}$$

which grows with s_0 and δ.

The density n of the MOT is defined as usual as the number of atoms N per volume: $n = N/z_{rms}^3$.

3.3 Atom Optical Manipulation of Argon Isotopes

3.3.1 Level Scheme of Argon

Atmospheric argon contains many different isotopes, some of them are listed in table 3.1 with their for ATTA most relevant features. From this we can easily see that measuring ^{39}Ar atoms is a tough nut to crack. Although argon is the third most abundant gas in earth's atmosphere with roughly 1 %, the challenge lies in the extremely low relative abundance of ^{39}Ar/Ar [29].

isotope	mass [u]	relative abundance	I	$\tau_{1/2}$
^{36}Ar	35.968	0.003365(30)	0	stable
^{37}Ar	36.967	no natural ab.	3/2	35 d
^{38}Ar	37.963	0.000632(5)	0	stable
^{39}Ar	38.962	$8.23{\cdot}10^{-16}$	7/2	268 a
^{40}Ar	39.962	0.996003(30)	0	stable

Table 3.1: List of relevant argon isotopes and their most relevant features. Taken from [4].

In order to define the requirements of the laser setup we need to examine the level structure of argon first. In this thesis the Paschen-Notation will be used for

description of the spectroscopic states. This notation is widely used in science and specifies a state by the general quantum number n of the excited electron minus the general quantum number of the highest ground state electron n_e, the angular momentum l of the excited electron and the total angular momentum $J = j + l + s$ with s the spin of the electron and j the total angular momentum of the body. The index q enumerates the states according to their energy and contains all other quantum numbers. This results in a notation $(n-n_e)l_q(J)$, whereas the ground state is noted as 'ground state' because for this we would get $n - n_e = 0$ [30]. Information on the notation specifically for argon can be found in [31].

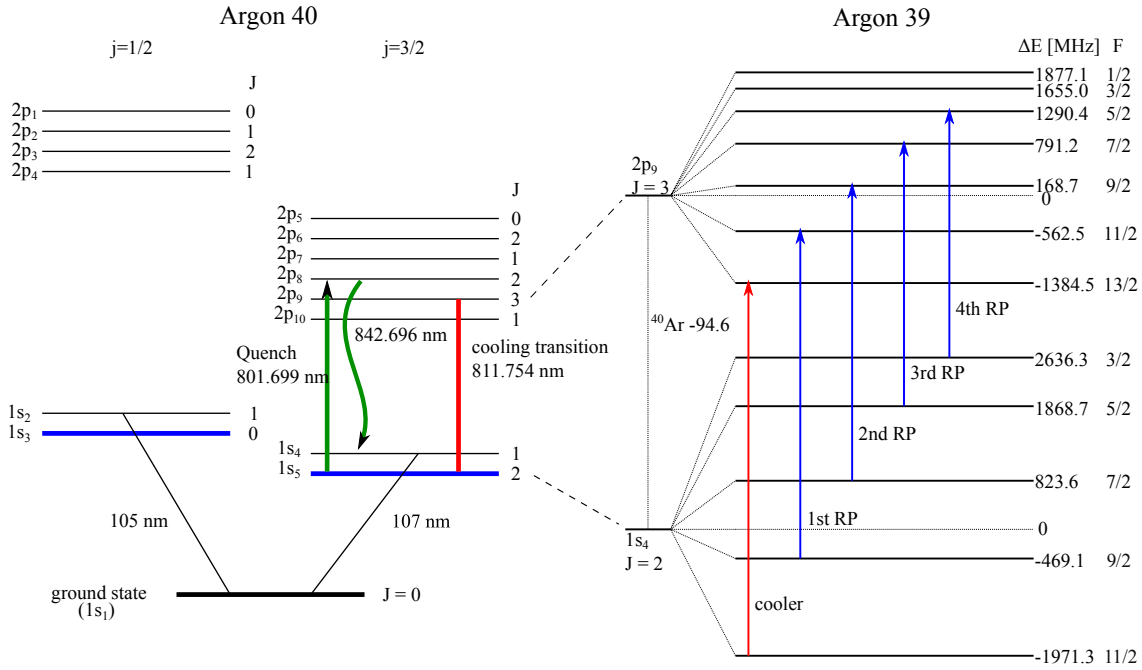

Figure 3.6: Energy spectrum for Argon: relevant transitions are marked with arrows, metastable states are highlighted in blue. Adapted from [32].

Figure 3.6 shows an excerpt of the energy spectrum for ^{40}Ar (representative for all isotopes of even mass number) and ^{39}Ar (for isotopes of odd mas number with nuclear spin I). For the operation of Doppler cooling a closed cycling transition is demanded since this method requires a huge amount of absorption-emission cycles in order to maximize the scattering rate and the force in eq. 3.36. Argon is a noble gas, therefore all electron shells are closed in the ground state $[1s^1 2s^2 2p^6 3s^2 3p^6]$ and reaching an excited state requires a high energy or a small wavelength $\sim$100 nm. Currently there is no laser or optics available for such wavelengths so a RF discharge source transfers a fraction of the atoms to a metastable state which can be adressed by laser light [31].

These states are marked in blue in figure 3.6. As the laser cooling transition $1s_5(J = 2)$ to $2p_9(J = 3)$ is chosen (a more extensive transition scheme can be found in appendix A). With a lifetime of 38 s the $1s_5(J = 2)$ metastable state is

suitable as the lower state of our cycle. Since selection rule $\Delta J = 0, \pm 1$ also applies in the Paschen notation, the $J = 3$ state can only decay back to $J = 2$ closing the transition.

Another excitation from the metastable state is used in the experiment as a quench, getting its name from the way it is quenching atoms out of the cooling cycle. This can be achieved by driving the $1s_5(J = 2) \rightarrow 2p_8(J = 2)$ transition. From the higher state the atoms can decay under emission of a 843 nm photon to the $1s_4(J = 1)$ state from which they can only decay back to the ground state being then lost for our lasers. After scattering a couple of quench photons the atom will eventually decay back to the ground state.

The level scheme gets more complicated for ^{39}Ar due to its nuclear spin of $I = 7/2$. The quantum number J does no longer fully describe the system and we need to introduce the new quantum number $F = J + I$. This splits the spectrum in the substates corresponding to F. The $1s_5(F = 11/2) \rightarrow 2p_9(F = 13/2)$ transition is chosen for cooling since the excited state can only decay back to the ground state due to the selection rule $\Delta F = 0, \pm 1$. However, the other levels are so close that a saturation broadened laser beam can excite other transitions as well. Because of this effect and in order to increase the ratio of atoms in the $F = 11/2$ state, new laser frequencies are introduced, the so-called repumpers [31].

3.3.2 Interaction of Argon with Light and Magnetic Fields

In the general case the force acting on atoms is given by eq. 3.43 so we have to find the argon-specific values for the variables in this equation in order to make well-grounded theoretical predictions. Taken from [20] the spontaneous decay rate for our chosen transition $1s_5(J = 2) \rightarrow 2p_9(J = 3)$ is

$$\gamma = 2\pi \cdot 5.87 \text{ MHz}. \tag{3.48}$$

A derivation of the saturation intensity for σ^+/σ^- polarized light is given in [4] and obtains the result of

$$I_s^\sigma = \frac{\pi h c \gamma}{3\lambda^3} = 14.4 \text{ W/m}^2. \tag{3.49}$$

It is important to note that the isotopes differ substantially under B-field influence due to their variance in nuclear spin. In the course of this thesis experiments are exclusively conducted on ^{38}Ar which has no nuclear spin therefore the quatum number J is suitable and fully describes the system.

Eq. 3.39 shows that the detuning δ_Z depends on the Landé-factor g_J which can be calculated (see [4]) or measured whereas the experiment yields for our states of interest $1s_5(J = 2)$ and $2p_9(J = 3)$ values of $g_2 = 1.5008(2)$ and $g_3 = 1.3335(1)$. Regarding a transition which is adressed by σ^+ polarized light we get a frequency shift of

$$\delta_Z^+ = \frac{1}{\hbar}[\Delta E(3,3) - \Delta E(2,2)] = (3g_3 - 2g_2)\frac{\mu_B B}{\hbar} = 1 \cdot \frac{\mu_B B}{\hbar}. \tag{3.50}$$

Correspondingly we can find an expression for a transition adressed by σ^- polarized light $(J = 2, m_J = 2) \rightarrow (J = 3, m_J = 1)$

$$\delta_Z^- = (1g_3 - 2g_2)\frac{\mu_B B}{\hbar} = -1.67 \cdot \frac{\mu_B B}{\hbar}. \tag{3.51}$$

These shifts have to be taken into account for the absolute detuning in eq. 3.44.

3.3.3 Numerical Integration of the Scattering Force inside a MOT for ^{38}Ar

Together with the results from the previous section, the scattering rates derived in eq. 3.20, 3.31 and 3.34 can be used for the simulation of atom trajectories inside the MOT. In order to obtain these trajectories a numerical integration of the scattering force needs to be performed. In this thesis we exclusively observed the isotope ^{38}Ar, therefore the ^{38}Ar specific values for δ_Z^-, δ_Z^+, γ and I_s are used (see 3.3.2). The ATTA MOT magnetic field is generated by anti-Helmholtz coils at a current of 10.7 A which corresponds to a magnetic field gradient of ~ 10 G/cm for the chosen geometry [33]. With a power of ~ 12 mW and a diameter of 32 mm the on-resonance saturation parameter for the MOT beams is $s_{01} \approx 1.0$.

Figure 3.7 shows the trajectories for the single frequency case. The detuning is chosen to be -8 MHz (current measurement detuning). It can be seen, that the capture velocity is 30 m/s.

The double frequency configuration is displayed in figure 3.8 and figure 3.9. The second laser beam is of the same power and same diameter as the original trapping beam, therefore the on-resonance saturation parameters are equal $s_{01} = s_{02} = 1.0$. The detuning is chosen to be $\delta_2 = -15$ MHz in both figures. The difference between these two is the used definition of the scattering rate for the numerical integration. For the calculation of the trajectories in figure 3.8 the time-dependent scattering rate in eq. 3.31 was used. Figure 3.9 uses the time-independent scatterring rate of eq. 3.34. Comparing the two figures they look very alike, being a direct validation of the time-independent approximation. They differ slightly in the capture velocity being 35 m/s for figure 3.8 and 36 m/s for figure 3.9. However, in both cases the capture velocity increases.

Besides the capture velocity, the simulations show the increase in capture range directly. For the double frequency cases, with a higher detuning $\delta_2 = -15$ MHz, the scattering processes (indicated as change in velocity) start already at a farer distance from the center.

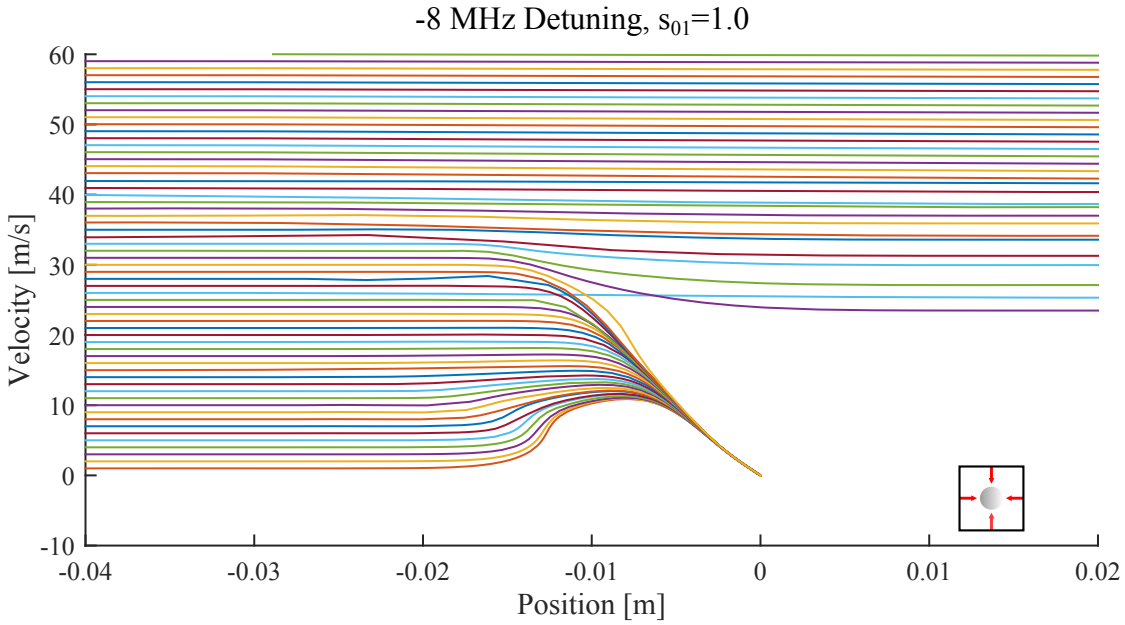

Figure 3.7: Numerical solution of the atom trajectories of ^{38}Ar inside a single frequency MOT. $\delta_1 = -8$ MHz, $s_{01} = 1$, $\frac{dB}{dz} \approx 10$ G/cm. Capture velocity $v_c = 30$ m/s. Small icons displayed in the graph should indicate whether the single or double frequency MOT is shown.

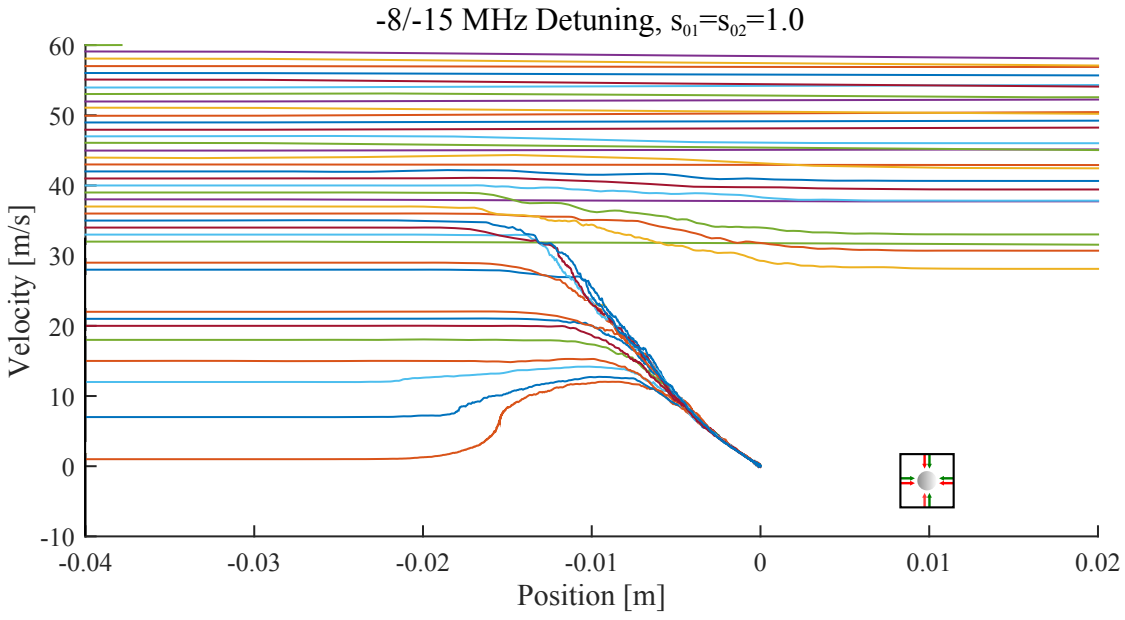

Figure 3.8: Numerical solution of the atom trajectories of ^{38}Ar inside a double frequency MOT with time-dependent scattering rate (eq. 3.31). $\delta_1 = -8$ MHz, $\delta_2 = -15$ MHz, $s_{01} = s_{02} = 1$, $\frac{dB}{dz} \approx 10$ G/cm. Capture velocity $v_c = 35$ m/s.

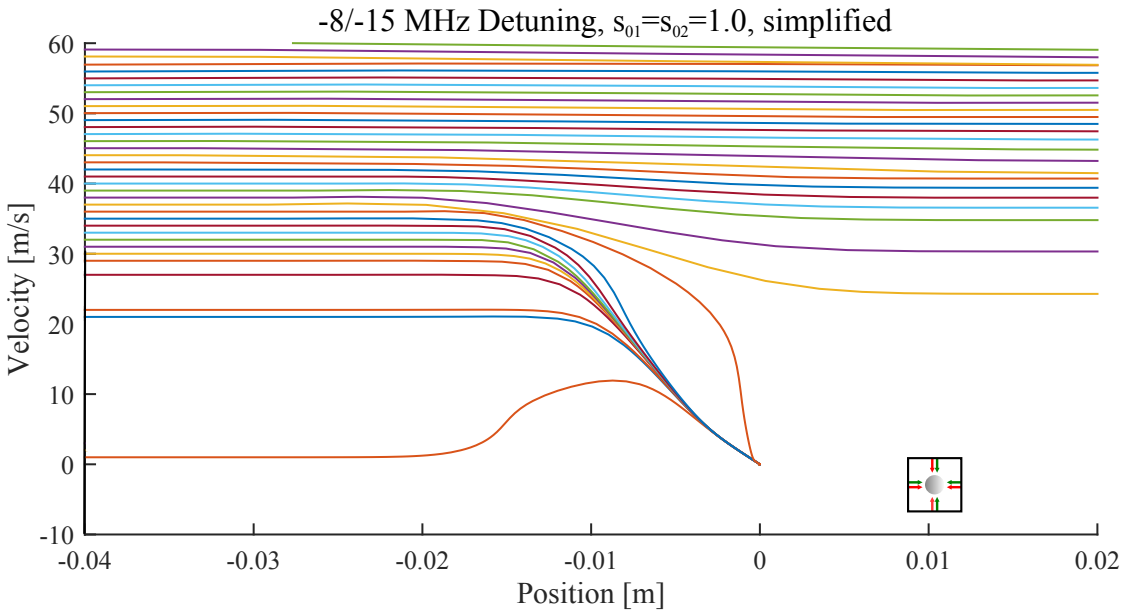

Figure 3.9: Numerical solution of the atom trajectories of ^{38}Ar inside a double frequency MOT with time-independent scattering rate (eq. 3.34). $\delta_1 = -8$ MHz, $\delta_2 = -15$ MHz, $s_{01} = s_{02} = 1$, $\frac{dB}{dz} \approx 10$ G/cm. Capture velocity $v_c = 36$ m/s.

4 Experimental Setup

Atom Trap Trace Analysis (ATTA) aims to determine the concentration of a specific isotope inside a sample by measuring its relative abundance inside extracted gaseous probes. This method has the ability to examine tracers of extremely low concentration. For our desired isotope ^{39}Ar the relative abundance is only $^{39}\mathrm{Ar}/\mathrm{Ar} \approx 8 \cdot 10^{-16}$ [4]. A sample which is degassed from an ice or water probe contains a whole variety of possible isotopes of argon and therefore only a tiny fraction ^{39}Ar. ATTA utilizes the isotope shift of the atomic transition frequency to specifically address only one isotope by narrowband laser light tuned to its internal resonance. Confining the tracer atoms in a MOT requires many light scattering processes which is the key mechanism to identify the isotopes. A non-resonant atom like ^{40}Ar scatters light from the laser beams resonant to ^{39}Ar with a non-zero probabilty that is still not negligible due to its high abundance, but inside the trap multiple photons need to be scattered, making a capture of the wrong isotope impossible. Therefore one isotope can be trapped with vanishing effects for the other isotopes which are not resonant with the laser. The fluorescence light from the MOT can be used to identify the capture of an atom. If we now count the atoms which are captured per time (count rate) from the sample and compare it to the corresponding count rate for an atmospheric argon sample we can conclude the relative concentration of this isotope inside the sample.

4.1 Atom Optical Tools in the ATTA Setup

Since our desired isotope has an extremely low relative abundance, capturing many atoms in order to get a feasible count rate is very challenging. The atoms need to be vertically and longitudinally slow in order to be trapped inside a MOT. Therefore a number of reasonable atom optical tools for manipulation of the argon beam is installed. In this chapter we want to briefly introduce these to make clear which laser frequencies are required to operate the ATTA machine.

Figure 4.1 shows the full apparatus with all its gadgets. The atom beam emerges from the source on the left side of fig. 4.1 and is directed towards the MOT on the right side. Gas samples are connected to the apparatus through the argon inlet where the gas flow towards the source can be regulated. Excited to the metastable state by the source, the atoms pass a transversal cooling stage (collimator) and are focused into the MOT by the magneto-optical lens (MOL). The ^{40}Ar quench reduces the high background of metastable ^{40}Ar. During their path through the Zeeman slower (ZSL) the atoms are longitudinally cooled so that they can be caught by the MOT directly behind it. An additional laser can be used to observe the ^{40}Ar beam cross section

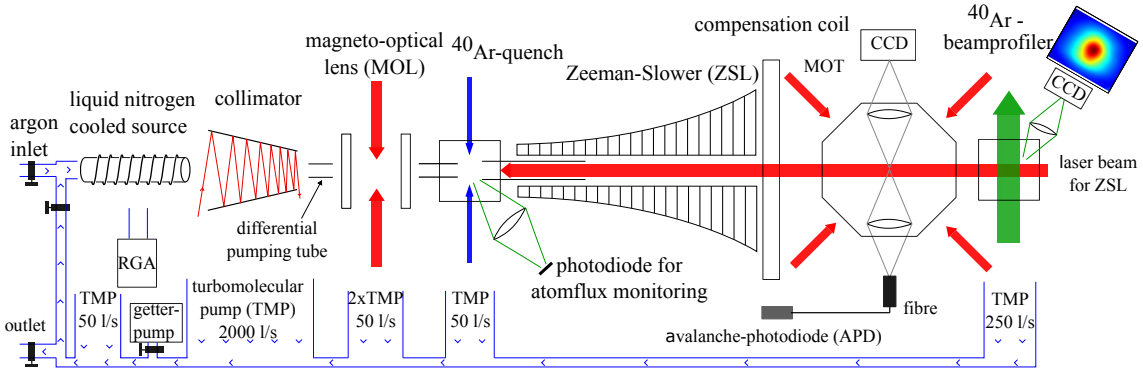

Figure 4.1: Scheme of the ATTA apparatus in Heidelberg. The flux of the atoms is directed from the source on the left side towards the MOT chamber on the right side. The figure includes the atom optical tools as well as the vacuum setup. Adapted from [4].

in the machine. In order to have a sufficient argon flux, the pressure in the source chamber is 10^{-5} mbar, but towards the end of the apparatus and especially inside the MOT chamber a high vacuum is indispensible since collisions with background gas influence the MOT lifetime radically. Therefore the pressure inside the MOT chamber is decreased by a differential pumping stage and a turbomolecular pump (TMP) directly behind the MOT chamber. For the measurement of small samples i.e. ocean water, the apparatus can be operated in the recycling mode. In this case the outlets of the TMPs are connected to the argon inlet in front of the source. A getter pump prevents a rapid pressure increase by atoms which were outgased from the chamber walls or entered via microscopic leaks by absorbing any gaseous components except for noble gases and methane. This way our argon sample can be recycled constantly [32].

Metastable Argon Source

As already discussed in the previous section a suitable cooling transition is found from the metastable state $1s_5(J = 2)$ to $2p_9(J = 3)$. Since argon is a noble gas, exciting an atom with a laser to the metastable state requires a small wavelength of 107 nm (UV range), which can not provided by currently available laser sytems. The implemented metastable argon source excites a fraction of the atoms to this state by stimulating collisions with electrons and ions. An inductively coupled plasma is generated by a properly designed copper coil directly at the argon inlet. Inside the hot plasma many fast charged particles clash with the argon atoms and excite them to any possible state. Some of these states are only short-lived and decay immediately. A fraction of the atoms ($\sim 10^{-4}$) end up in the metastable state $1s_5$ by relaxation or direct excitation. Liquid nitrogen cooling of the source decreases the velocity of the atoms and also increases the fraction of atoms in the desired state [31].

Collimator

The metastable atoms still have a vast velocity spread around $v_z \approx 240$ m/s but are fortunately addressable by laser light now [4]. Directly behind the source the collimator is installed as a transversal cooling stage for the atom beam. It consists of two long, nearly parallel mirror pairs which are slightly tilted so that a laser beam can be reflected along the wide side of the mirrors, crossing the atom beam multiple times. The angle between laser light wavevector and atom propagation direction is chosen in such a way that the laser is at any point resonant with the atoms cooling transition. The precise adjustment of the mirror angle enables transversal cooling throughout the extent of the collimator [20]. The detuning of the laser has to be chosen corresponding slightly positive with $\delta_c = +4.6$ MHz. Directly behind the source, the atoms which are in the desired metastable state are distributed over all possible hyperfine states. The usage of repumpers inside the collimator enables us to pump the atoms efficiently into the $F = 11/2$ substate to decrease the leaks into other states [31],[34].

Magneto Optical Lens

This tool is essentially a two-dimensional MOT but owes it's name to the way it is used: like a lens for atoms. Two coils in anti-Helmholtz configuration with the symmetry axis overlying the atom beam generate a quadrupole magnetic field which transversal component has a constant gradient over the extent of the laser beams. Four red-detuned ($\delta < 0$) laser beams cross the atom beam from all transversal directions so that the atoms experience a force towards the point of zero magnetic field which overlies the center longitudinal symmetric axis of the apparatus. Although the collimator already cooled the transversal velocity component, the MOL reduces the transversal spread even further so that the atoms are effectively focused into the MOT center. The velocity spread in transversal direction is especially dominant when the atomic beam is longitudinally cooled by the Zeeman slower. The laser beams used are of the same frequency as the lasers for the realization of the 3D MOT in order to reduce the number of AOMs and keep the setup as simple as possible. An additional frequency shift compensating the Doppler shift can be introduced by variation of the angle at which the laser and the atoms intersect [35].

^{40}Ar Quench

Inside the MOT chamber the fluorescence light of single atoms is recorded by a very sensitive avalanche photodiode (APD) in order to identify the capture of an atom. The APD signal increases as the fluorescence of the trapped atom is scattered onto the photodiode. A captured atom therefore stands out as a spike indicating a suddenly higher amount of photons. However, a continuous argon flux flows through the experimental chamber which mainly consists of ^{40}Ar atoms which scatter photons but are not captured. Although the probability of a scattering event to happen is

small, the high relative abundance of ^{40}Ar increases the number of scattered photons per time noticeably, causing a background on the APD signal. This complicates the definite detection of single ^{39}Ar atoms. This problem is addressed by a laser beam sited directly behind the MOL, which is tuned to the quench transition in ^{40}Ar (see chapter 3). The APD signal looses its background offset and single atoms stand out more distinct [32].

Zeeman Slower

The Zeeman slower is elaborately explained in [33], for this thesis only essential points will be discussed. This tool is a standard device for longitudinal deceleration of an atomic beam without changing the cooling frequency in order to compensate for the varying Doppler shift. It utilizes the Zeeman effect by changing the energy splitting such that an atom which is resonant to the laser light of fixed detuning and polarization stays at any point of the slower resonant. The copper coils which are generating this B-field are specifically designed for our purpose and extend over 1.8 m (see appendix B). The laser beam longitudinally overlies the atomic beam all the way inside the slower with its detuning chosen such that atoms of a maximal initial velocity of $\sim$200 m/s can be cooled down to a desired velocity. The laser light is strongly red detuned with $\delta_Z = -746.2$ MHz. As the atoms are slowed down, the Doppler shift decreases and the B-field needs to compensate for this by increasing the magnetic shift. Therefore the field is chosen to increase towards the end of the slower. The laser beam needs to be resonant to the longitudinally fast atoms at the start of the slower. As the atoms are longitudinally cooled they undergo a random walk in the transversal directions. If we would tune the Zeeman slower to cool the atoms down to zero longitudinal velocity, their transversal spread would dominate the propagation of the beam behind the slower. Since the atoms need to overcome $\sim$10 cm to reach the center of the MOT they would be likely to hit a wall before arriving in the area of the trapping beams. Therefore the Zeeman slower is built to cool the atoms to $v_z \approx 40$ m/s. Additionally, they are cooled further in the proximity of the MOT by another red-detuned laser.

Atom Beam Imaging

Directly behind the MOT the atomic beam intersects a sheet of light at a 45° angle. This laser beam is tuned to the resonance of ^{40}Ar stimulating absorption and emission of photons by the atom beam (quench, ZSL and MOT need to be turned off). A camera underneath the experimental chamber observes the fluorescence light, such that a beam profile can be obtained. This tool enables us to monitor the quality and position of the atom beam and testing and optimizing source, collimator and MOL [32].

Magneto-Optical Trap

The heart of the ATTA apparatus is its MOT. The concept of a MOT was introduced in chapter 3. Although MOTs are commonly used to confine a high number of atoms ($\sim 10^6$), they are also a suitable tool for the capture of single atoms. Considering the cooling process, several laser frequencies are necessary for an operation of the trap. Inside the trap the atoms need to scatter as many photons as possible, therefore we need to keep the atoms in the cooling cycle for a long time and ensure that the scattering rate is high. ^{39}Ar atoms are lost due to collisions with background gas or because of leaks to other hyperfine states introduced by off-resonant excitation. To compensate for the latter, additional laser beams, the repumpers, are introduced into the chamber addressing transitions to bring the atoms back into the cooling cycle. The current setup enables the provision for three repumper frequencies, see also figure 4.2. Only two are necessary in the MOT for the proper detection of single atoms, the third repumper is only used in the collimator. Another laser that enters the chamber through the MOT fiber is a quench for ^{38}Ar, which acts exactly like the ^{40}Ar quench but only with a shifted frequency to compensate for the isotope shift. This laser allows for conduction of measurements on a ^{38}Ar MOT by implementing a fast emptying of the trap.

Defining the requirements for the lasers in the ATTA apparatus was the first step towards the design of our laser setup. The overall goal of the experiment is to capture the highest possible amount of ^{39}Ar atoms inside the MOT. A handy extra is the ability to address other argon isotopes as well. The optimization of laser setup parameters by the observation of ^{39}Ar is not feasible. Due to its low abundance the number of atoms in the sample is very low and iteration of parameters to yield the highest signal would take too long. Therefore our setup should be designed to not only observe ^{39}Ar, but also the more abundant isotopes ^{38}Ar and ^{40}Ar. In the future it would be desirable to be also able to observe an isotope of odd mass number since they have a nuclear spin. Observing for example ^{37}Ar would help us understanding the effects of the lasers onto ^{39}Ar better, especially for such that are only necessary due to the hyperfine level structure of ^{39}Ar, like the repumpers. However, as can be seen in table 3.1, ^{37}Ar is not produced naturally but only synthetically as a sideproduct in nuclear explosions. Besides this, the lifetime of ^{37}Ar is only 35 days short making the measurement with ATTA very challenging.

4.1.1 Required Laser Frequencies for the Operation of ATTA

Extracted from the previous section, a list of all required laser frequencies is displayed in table 4.1 with their frequency shift relative to the ^{39}Ar cooling transition or other transitions as the quench. Each frequency is denoted by an abbreviation which either is defined by the atom optical element they are used for or the name of

name	frequency shift towards $1s_5 \rightarrow 2p_9$ cooling trans. in ^{39}Ar [MHz]	frequency shift relative to other trans. [MHz]	optical tool
COL	+4.6	-	Collimator
MOT	-8.2	-	MOT, MOL
ZSL	-746.2	-	ZSL
Booster	-26.2	-	MOT
1. RP	-675.5	-	MOT, Collimator
2. RP	-1237.1	-	MOT, Collimator
3. RP	-1659.7	-	Collimator
4. RP	-1928.1	-	Collimator
^{40}Ar Quench	-	+0 for ^{40}Ar quench trans.	^{40}Ar Quench
^{38}Ar Quench	-	+0 for ^{38}Ar quench trans.	MOT
BI	-	+0 for ^{40}Ar cooling trans.	Beam Imaging

Table 4.1: List of required laser frequencies and their detuning relative to a chosen transition.

the corresponding transition frequency. Table 4.1 also shows in which atom optical tools the frequencies are needed, for example the repumpers (RPs) are necessary for the operation of the MOT but also for the collimator.

4.2 Design and Realization

Given the requirements from table 4.1 and the material from the previous ATTA laser setup the laser frequencies are generated as shown in figure 4.2. Doppler-free saturation spectroscopy of the cooling transition inside a argon filled cell obtains the precise frequency of this transition in ^{40}Ar. A diode laser (Toptica DL Pro), which serves as master, can now be locked to this transition giving the system a frequency reference.

The frequency shift towards other isotopes of argon is overcome by locking two other lasers (Toptica TA 100) to a defineable offset from the Master which will be called Slave 1 (Cooler) and Slave 2 (RP). In order to do so, the slave and the master are superposed, creating a beat signal which an offset lock utilizes for locking. With this procedure the frequencies of the slaves are fixed to a widely tuneable offset relative to the ^{40}Ar reference. Minor frequency shifts can be introduced by acousto-optical modulators (AOMs) in double-pass configuration. Currently ^{40}Ar, ^{38}Ar, ^{36}Ar and the isotope of major interest ^{39}Ar can be addressed. Another spectroscopy cell is used to lock a home-built external cavity diode laser (ECDL) to the quench transition in ^{40}Ar. With an AOM in single pass configuration the necessary frequency shift towards the ^{38}Ar quench is generated.

The concrete realization of the required powers is however more difficult. Taken

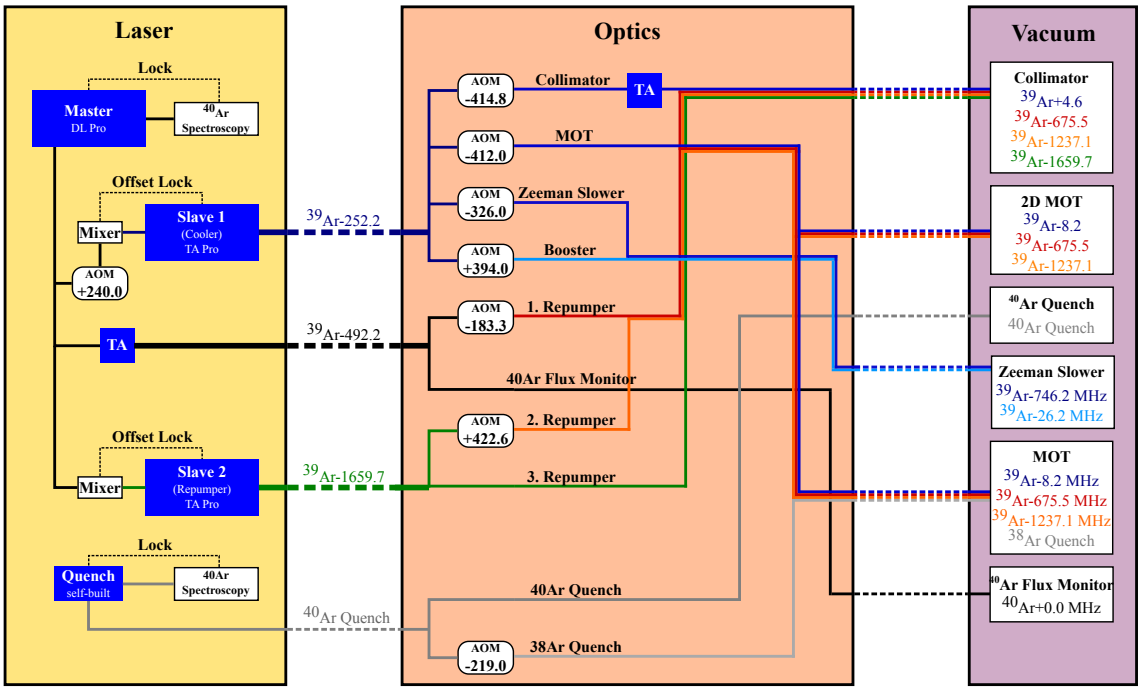

Figure 4.2: Realization of the required laser frequencies for the operation of ATTA. The laser setup is divided into three modules: laser, optics and vaccum. On the left side the laser module is displayed. It features the four lasers which are used to generate the basic frequencies, which are the master (Toptica DL Pro) locked onto the cooling transition in ^{40}Ar, the two slaves (Toptica TA 100) locked via an offset lock each and the ^{40}Ar quench (self-built). The master passes a TA to increase its output power. These four lasers enter the optics module in the middle where the laser beams are splitted. Each required laser frequency is generated by AOMs in double-pass configuration (except for ^{38}Ar quench, which is single pass). Additionally the power of the collimator is boosted with a TA. Through fibers the laser beams enter the vaccum system and therefore the atom optical tools. A scheme of the actual optics setup can be found slightly modified in appendix C.

from the previous setup, ATTA provided a commercial ECDL (Toptica DL Pro) and one self-built ECDL. These lasers are a handy tool when it comes to generating a narrowband laser beam. More information on these can be found in [36] or [37]. They generate a single mode laser beam by frequency selective feedback of an ordinary diode laser due to a grating. The ECDLs in use are built in the Littrow configuration where the first order diffraction from the grating is coupled back to the laser [36]. This frequency selective feedback reduces the linewidth by two orders of magnitude. They provide a linewidth of ∼100 kHz and and a widely tuneable frequency range of few 10 GHz. Despite all their assets their useable output power is not satisfying

being only about 10–100 mW.

4.2.1 Tapered Amplifiers

Since ECDLs do not provide enough output power, using tapered amplifier diodes (TAs) is often the method of choice to upgrade laser intensities if the broad light background from the chip itself is not disturbing. These chips enable amplification of the seeding beam up to 2 W while maintaining all its properties [38]. This way a narrow-linewidth single mode laser with high output power (atop a broad but less high background) can be realized by a combination of ECDL and TA.

The TA itself consists of a small mount providing heat dissipation underneath a tiny semiconductor chip with specifically etched waveguides atop of it. Delicate bond wires which are linked to a larger, flat connector supply the chip with uniform electrical pumping. Incoming light first passes a short, straight waveguide section that ensures the excitation of only one mode ($\sim$0.5 mm long) and is then amplified by a tapered passage ($\sim$2 mm long) [39]. A rough sketch of this geometry can be seen in figure 4.3 (right). The inlet of the chip is $\sim$1-3 μm wide and the outlet $\sim 200\mu$m, therefore inserting seed light to the input facet requires finely adjustable optomechanics. High currents of 2–2.5 A running trough the chip demand of a heat sink and temperature control. Commercial TA chips including all necessary add-ons like optomechanics, voltage supply and temperature control are offered by many companies to a noticeable higher price than a home-built setup would cost. Currently the setup is using two self-built TAs additional to two commercial TAs (Toptica TA 100).

Before taking the chip into operation some inevitable preparations have to be made and precautions need to be taken. An extended report on how to handle TAs is given in [39] here we want to shortly point out the most important information and transfer it to our application. TA chips are infamously delicate and various dangers might harm the diode like too high seed power, spikes in the driving current or even outgassing from silicone-based heat paste. It is important to remember the deadly effect of retro-reflections to the chip so a Faraday Isolator should be placed directly behind the TA module at any time. Inserting seed in the turned off TA chip can also cause damage, therefore the TA current should only be off if it is not seeded. Besides, the temperature regulation is crucial since the chip experiences high currents which dissipate heat in the TA accelerating the degradation process. After long operation times at high currents it is even possible that the bonding wires of the chip burn which happened to the chip shown in figure 4.3 (left). High laser intensities might also attract small particles just like an optical tweezer therefore a shielding should always protect the whole amplifier. Figure 4.4 shows a chip with a dust particle burned on it. In any way the diode has a finite lifetime even if extreme caution is exercised.

Even with seed the TA also acts as a common laser diode when current is applied bringing about a background to the output light called amplified spontaneous emission (ASE) which is emitted from both sides of the chip. The ASE light is a

pedestal to the amplified light of ∼4 nm linewidth and 1 % power but it can be reduced to less than 0.2 % of the amplified power by coupling the TA output into a single mode fiber [40]. The sensitive anti-reflection coating is essential to the performance of the TA because it suppresses the amplification of ASE light. Due to that, a damaged coating can cause higher background and hinders the mode matching of seed and input facet. Taking a closer look at the ASE we can differentiate if the chip is nicely seedable or not. A TA chip which shows a strongly non-gaussian ASE beam shape is tough to seed. Most of the older chips showed deformed ASE modes of high intensity which might be an indication for degradation of the anti-reflection coating.

Meeting all of the requirements in order to ensure a long lifetime of the chip, we can now start to reach a high performance of the amplifier. In order to get the highest amplification possible, the seed laser beam profile should perfectly match the size and shape of the tapers inlet (mode-matching).

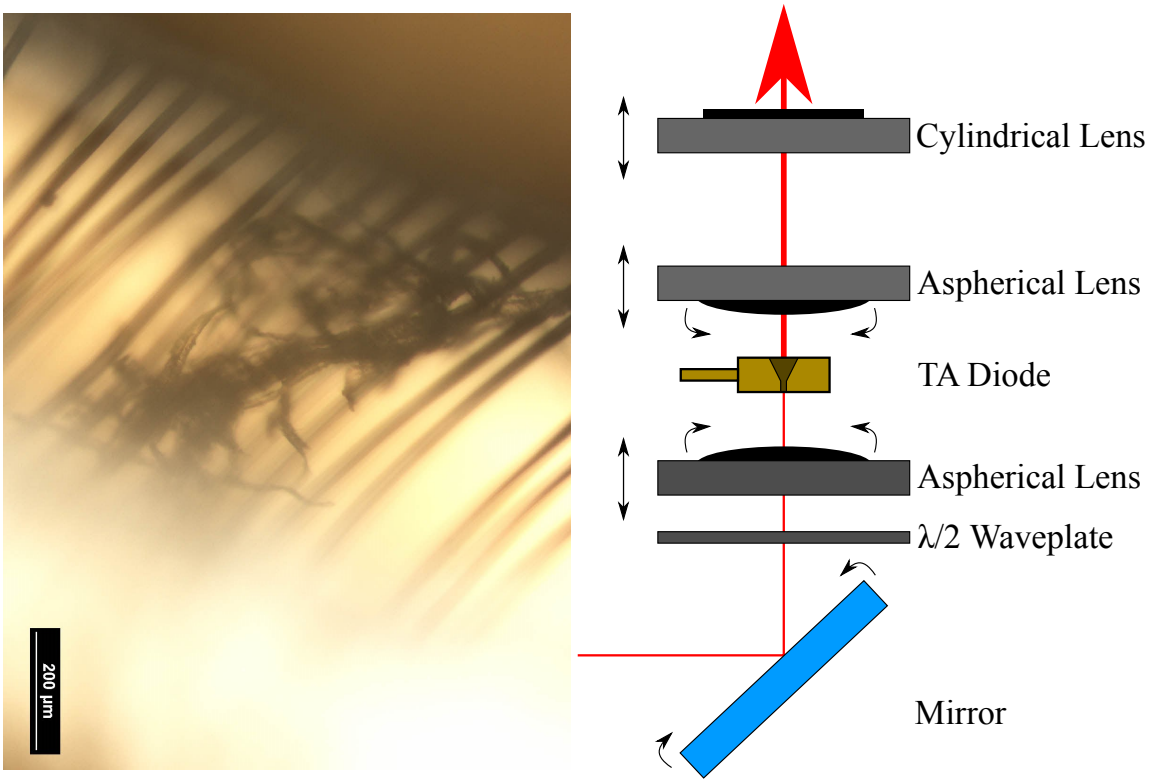

Figure 4.3: Left side: Bond wires of an old TA chip. Some of them were destroyed during the running time. Right side: Simple TA optics sketch: Straight arrows indicate mobility in z-direction, bent arrows show degrees of freedom in xy-plane.

Our current self-built design has the chip screwed on a copper mount which itself is placed on a large aluminum heat sink. A cage system serves as a mount for the optomechanics providing xy-confinement while maintaining z-mobility. The cage

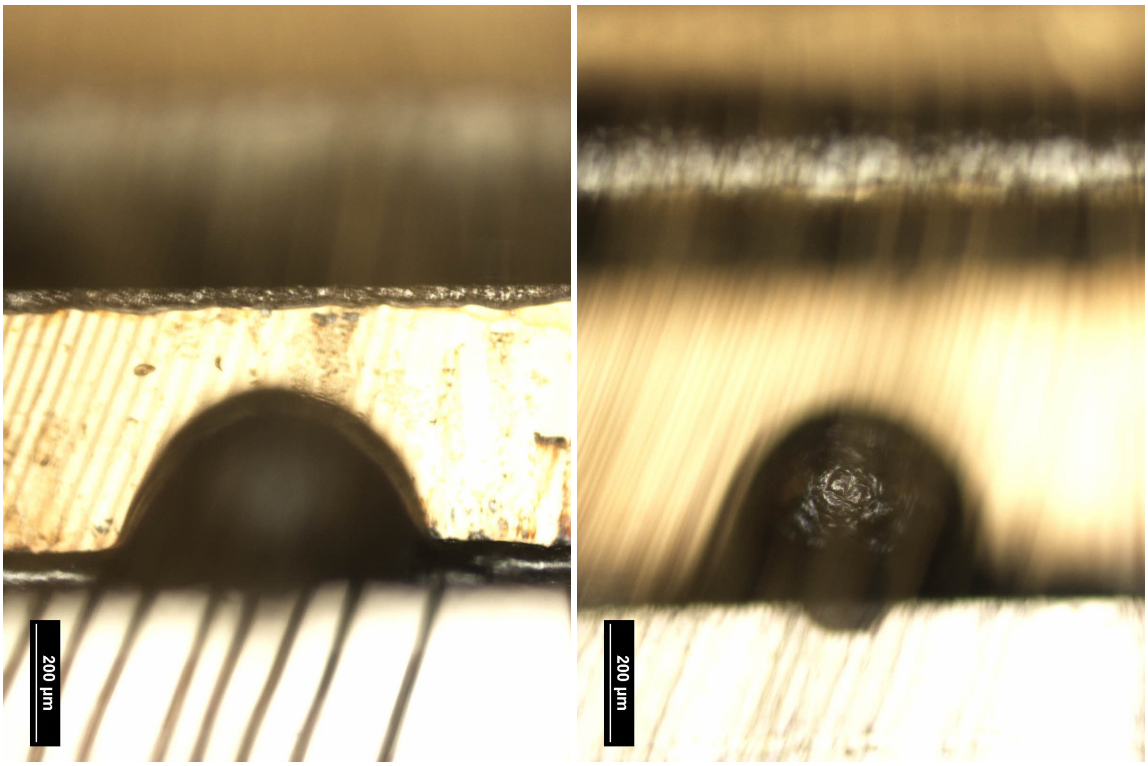

Figure 4.4: Broken TA chip with dust praticle burned onto its surface.

rods pierce the TA mount in a way that the center of the cage system overlies with the chip waveguide. For focusing the seed light onto the rear facet of the diode an aspheric lens is placed close to the chip. Since the chip has a favored polarization direction, the polarization of the incoming light can be changed by a rotatable $\lambda/2$ plate directly in front of the first asphere. An additional mirror angled 45° relative to the propagation direction of the seed coming from the fiber serves for extra tuneability to facilitate all degrees of freedom. Aspheres can be slightly tilted in xy-direction with micrometer screws and delicate z-positioning can be achieved by an additional micrometer screw. The z-position of the cylindrical lens can only be coarsely adjusted by sliding it on the cage system rods. Details of this setup can be found in [41] or [42].

Observing the backtravelling ASE, we overlie the incoming seed with it and try to match the beams as good as possible. This way we ensure that the seed exactly hits the input facet. Since the seed is coupled to the TA via a fiber the size of the seed beam can be slightly tuned by the choice of laser beam coupler which needs to be optimized for every chip. While monitoring the output power of the TA, the positions of the first asphere, mirror and seed coupler are optimzed for highest output intensity. The polarization of the seed is optimized by turning the $\lambda/2$ waveplate.

However, the system contains some major drawbacks that are mainly caused by the cage system itself. In the orignal setup the cage rods could not be fastened to the copper mount generating major instabilities of the seed beam position. This

problem was solved by designing new copper mounts with smaller holes so that the rods fit snugly through and screw threads for fastening. Still it is possible that the rods are not perfectly parallel which complicates the z-movement considerably. A new TA design could reduce the number of degrees of freedom and therefore the instabilities.

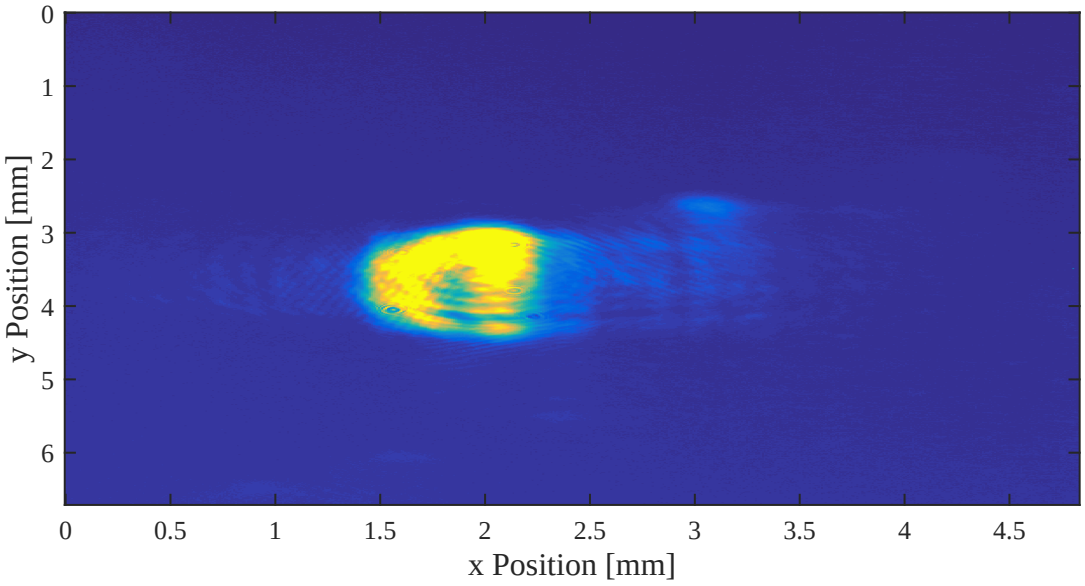

Figure 4.5: Typical beam shape of the amplified light from a TA at 1.6 A current.

The outcoming amplified laser beam is highly astigmatic and asymmetric, especially the vertical direction of the beam is strongly diverging. Therefore a second asphere behind the chip corrects the divergence and a cylindrical lens behind it shapes the beam spherical. Since the output light of a TA departs significantly from a gaussian TEM_{00} profile as can be seen in figure 4.5, coupling efficiencies of only 40 % – 50% can be reached [38],[39]. Because the astigmatism of the output beam varies with TA current it is necessary to do the final alignment at the desired operation current.

Eventually we used two self-built TAs to boost the power of the master and collimator and finally reached the required laser intensities.

4.3 Operation of the ATTA Machine

After the laser setup was finished and ready for operation, the system was extended to monitor important parameters: laser frequencies and powers as well as environmental parameters affecting the apparatus. This should confirm the stability of the apparatus' performance at any time during a measurement.

Photodiodes for the monitoring of laser power were attached behind mirrors which reflected the laser beam of interest. Since the reflectivity of the mirrors is $\sim 99\%$ for our wavelength, $\sim 1\%$ of the laser power transmits through the mirror onto the photodiode. Additionally, a Fabry-Perot Interferometer (FPI) was set up behind one MOT fiber to observe shifts in frequency or power of the repumpers and the cooler. The stability of the quench and master lock as well as the offset locks for the two slave lasers were monitored. A newly designed temperature control for the lab was set up by Sven Ebser which also enabled the observation of room temperature and humidity. In order to stabilize their output power, the two self-built TAs are connected to a photodiode which controls the current of the amplifier.

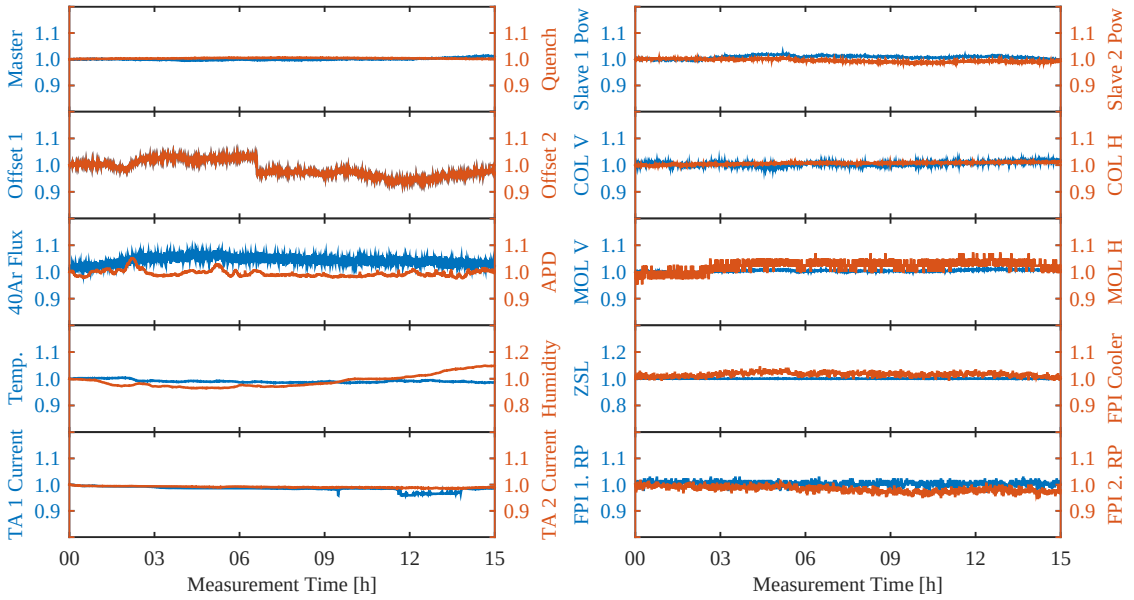

Figure 4.6: Monitoring data obtained during a measurement. Each measured value is divided by the mean value of this parameter for the observed time span. The x-axes display the measurement time in hours, whereas the various y-axes display the normalized values of the denoted parameters. The monitoring system was initialized in [32].

Figure 4.6 shows the monitoring data obtained during a measurement done with the new laser setup. It can be seen that most parameters are stable whereas some underlie minor variations. Fluctuations of $\sim 10\%$ can in some cases not be prevented. Still, results like these in figure 4.6 validate the stability of the system which motivated us to measure samples.

In order confirm the ability to measure actual environmental samples we first tested the machine with samples of known ^{39}Ar concentration. The samples examined were specifically produced from a mixture of dead argon [43] (no ^{39}Ar inside, 0% modern argon (pm Ar)) and atmospheric argon (100 pm Ar). For our test run one

dead sample, one containing 33 pm Ar and one containing 66 pm Ar were measured. Additionally, one already dated groundwater sample from a previous measurement [12] was analyzed. The reference is obtained by measuring atmospheric argon.

Previously published results [12] were generated in throughput configuration, in which the sample is pumped out of the apparatus after passing it once. Every ^{39}Ar atom has therefore only one chance to be counted. In order to obtain a reliable atom number, measurement times are >10 hours long, which requires large sample sizes which are mostly hard to come by for ocean water.

The recycling configuration enables the concentration measurement for small samples by reusing the sample permanently. The outputs of the pumps are connected to the inlet of the source causing the sample to cycle inside the chamber. Problematic about this configuration is that gas particles adsorbed by the chamber walls are kicked out by fast argon atoms of the sample which hit the walls. This causes a constant outgassing and therefore an increase of sample size. A getter pump prevents the destruction of the vacuum by pumping out everything except for noble gases and methane. This way the sample is not affected and unwanted gas gets pumped out.

Besides other gases also argon is outgassed from the chamber. During the first setup of the experiment, the ATTA team was forced to introduce highly ^{39}Ar enriched samples into the chamber to obtain first knowledge on the apparatus. This way the performance of atom optical tools addressing ^{39}Ar like MOT, collimator and Zeeman slower could be optimized. Due to these samples a high amount of ^{39}Ar atoms is absorbed by the chamber walls and is constantly sputtered out while the running source creates fast argon atoms.

In the throughput configuration this is not a problem, since the gas from the apparatus is constantly pumped out. However, as the sample cycles in the recycling mode, the sample starts to get contaminated with the ^{39}Ar atoms from the apparatus.

This contamination limits the measurement time in the recycling mode and manipulates every measured concentration. The increase in time of the total counted ^{39}Ar atom number N for the recycling configuration can be split up in two causes. Due to the sample which is cycling in the apparatus N increases linearly in time, since every atom can be measured during each cycle. The number of atoms in a sample is denoted by its concentration c. However, our apparatus runs on a specific counting efficiency which is defined by the count rate λ. This value is defined as the number of atoms counted by the apparatus per hour for a sample of $c = 1$, a sample containing 100 pm Ar. The number of counted atoms due to the sample is therefore $N_{sample}(t) = c\lambda t$ ([t]=h).

Additionally, the contamination of the apparatus constantly introduces new ^{39}Ar atoms into the sample, therefore the measured concentration increases with time. A model describing this was introduced before in [44] and can be seen as an accelerated motion with the contamination acceleration a. The value of a determines the number of atoms which are extracted from the machine per time. Still the count rate λ defines the number of measured atoms, therefore we obtain $N_{cont}(t) = \frac{1}{2}a\lambda t^2$ after

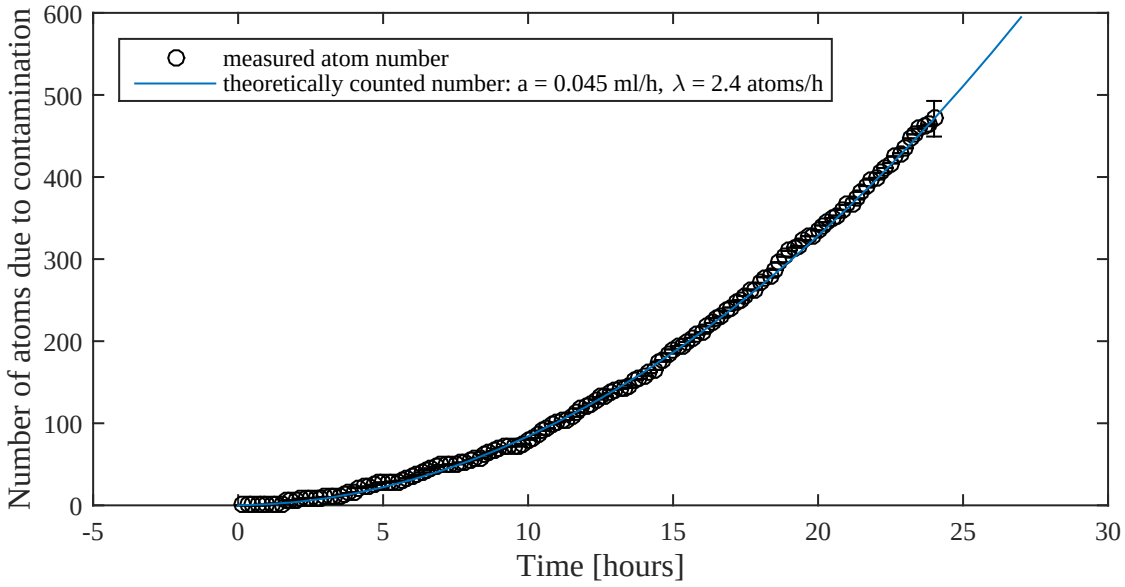

Figure 4.7: In recycling configuration measured contamination of a dead argon sample over time. Number of measured atoms shown by (black) circles, the solid (blue) curve displays the theoretically counted atom number for a count rate of $\lambda = 2.4$ atoms/h and a contamination acceleration of $a = 0.045$ ml STP/h. The error of the total atom number in the end is given by its squareroot (Poisson).

integration. Taking both parts into account we get the total counted atom number at measurement time t:

$$N(t) = \frac{1}{2}a\lambda t^2 + c\lambda t + N_0, \tag{4.1}$$

whereas N_0 is the atom number in the beginning of the measurement. We can rewrite N_0 as the number of contamination atoms which are not counted due to a time delay in the start of the source and the start of the measurement [1]. This delay is defined as t_0 therefore $N_0 = \frac{1}{2}\lambda a t_0^2$ and we finally get the number of counted atoms

$$N(t) = \frac{1}{2}a\lambda(t + t_0)^2 + c\lambda t - \frac{1}{2}a\lambda t_0^2. \tag{4.2}$$

The contamination acceleration is given in ml STP h^{-1} since the value of a increases with decreasing volume [ml STP]. For larger sample sizes the contamination plays a smaller role since the number of atoms inside the sample is higher.

The value of a was newly determined by measuring the contamination of a dead sample. We introduced a small volume of dead argon ($V = 59$ μl STP) into the

[1] The time of the measurement start is defined by the time data acquisition begins. Starting the source also triggers the generation of contamination atoms. Between these two times contamination atoms are generated but are not counted.

chamber and measured the number of ^{39}Ar atoms in recycling configuration. Figure 4.7 shows the number of counted atoms over measurement time. Since the sample contains no ^{39}Ar, the concentration c is zero and all of the atoms counted are due to contamination from the machine. Eq. 4.2 simplifies to

$$N(t) = \frac{1}{2}\frac{a}{V}\lambda(t+t_0)^2 - \frac{1}{2}\frac{a}{V}\lambda t_0^2 = \frac{1}{2}\frac{a}{V}\lambda((t+t_0)^2 - t_0^2). \tag{4.3}$$

From the total number of counted atoms in figure 4.7, the measurement time t and the time delay t_0 we can calculate the new contamination acceleration to be

$$a = \frac{2NV}{\lambda((t+t_0)^2 - t_0^2)} = 0.045(5) \text{ ml STP h}^{-1} \tag{4.4}$$

with the current count rate $\lambda = 2.4(1)$ atoms/h. This count rate was obtained from several reference measurements of 100 pm Ar in throughput configuration. The from these values calculated atom number per time is displayed by the blue curve in figure 4.7. The theoretical data overlies the measured data points nicely and we can therefore assume that the newly calculated contamination acceleration accurately describes our system.

Shortly before the measurement, the big turbopump directly at the source chamber was replaced by a new one. Since this pump was a victim of the previously mentioned enriched samples, the change to a new pump decreased the contamination accelereation from $\sim$0.05 ml STP h^{-1} [44] to the new value of $a = 0045(5)$ ml STP h^{-1}.

The determination of the contamination effect enables us to correct the measured concentration of the mixed samples. From eq. 4.2 we can derive the actual sample concentration c to be

$$c = \frac{N(t)}{\lambda t} - a\frac{(t+t_0)^2 - t_0^2}{2Vt}. \tag{4.5}$$

Figure 4.8 shows preliminary results for the concentrations for the previously mentioned mixed samples and the sample which was already measured in 2013. The data points displayed on the y-axis were obtained by counting the atom number in recycling configuration and calculation of the concentration c with eq. 4.5. Values on the x-axis refer to known mixed concentrations or previously measured ones.

Both figures 4.8 and 4.7 show that the ATTA machine obtains reasonable results and can therefore be used for dating. The newly set up laser system works as expected and long and stable measurement cycles can be realized. The apparatus is able to measure concentrations in recycling configuration, paving the way for measurements with small sample sizes.

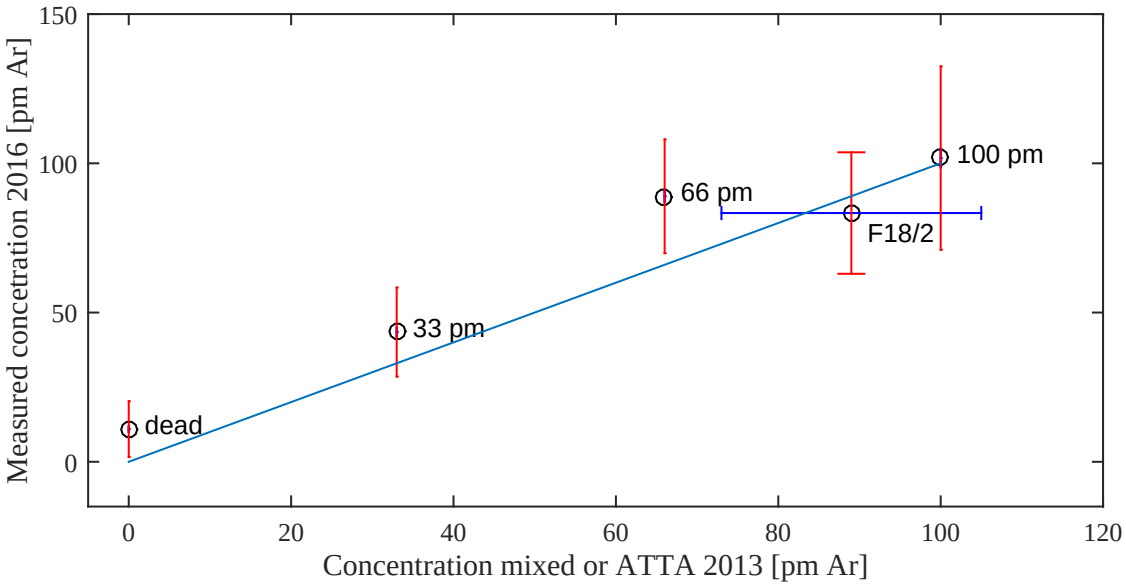

Figure 4.8: In recycling configuration measured concentrations of mixed samples and one groundwater sample. The concentrations are already corrected by the contamination calculated from $a = 0.045(5)$ (see figure 4.7). The 100 pm Ar data point is the mean calculated from six different measurements, weighted with inverse of the error for this measurement. For the other points only one measurement was conducted.

5 Characterization of the Single and Double Frequency Magneto Optical Trap

This chapter aims to present and analyze experimental data generated at the ATTA MOT. First we examine the influence of the detuning of the current setup on the number of captured atoms per time. The introduction of a second MOT trapping frequency is believed to yield a higher capture efficiency. Under variation of the detuning of first and second frequency the behavior of the system is studied.

5.1 Current Status

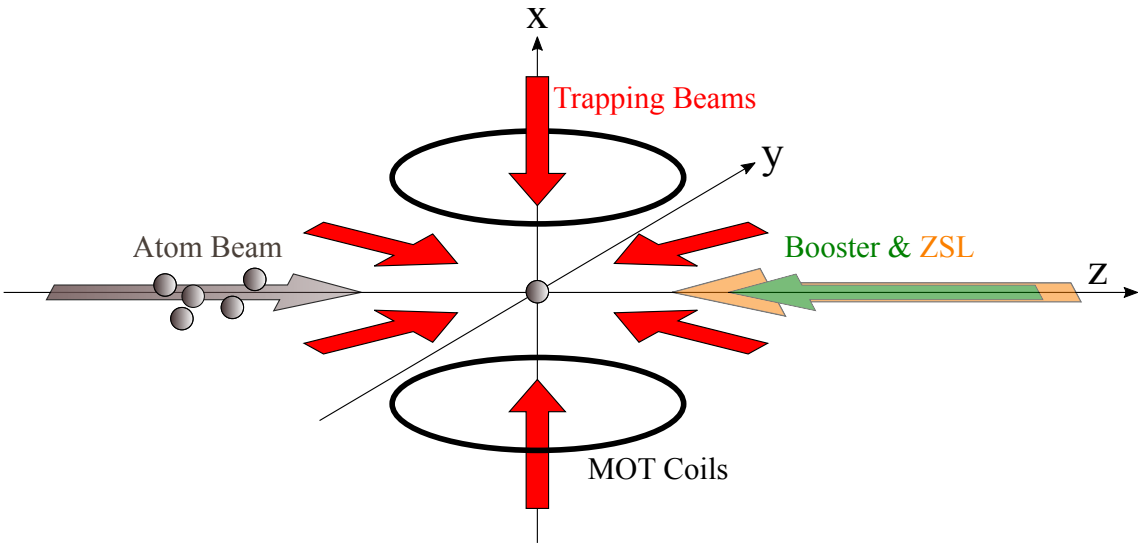

Figure 5.1: Scheme of the ATTA MOT setup with the geometry of the trapping beams (red), Zeeman slower laser (orange) and booster (green). Atoms enter the MOT from the left side (grey).

The trap geometry realized at the ATTA apparatus is shown in figure 5.1. On the left side slowed atoms emerge from the Zeeman slower into the MOT region. Copper coils in anti-Helmholtz configuration are placed above and below the center of the chamber to generate the required magnetic quadrupole field. Outside the chamber, along the y-axis, detection instruments are placed in order to conduct measurements. A CCD camera for observing a large trapped cloud is installed

in positive y-direction whereas on the opposite side a multi-mode fiber connected to a very sensitive avalanche photodiode (APD) collects fluorescence light. The APD observes only a small spatial region directly in MOT center which reduces the background and enables the detection of single atoms. Three laser beams which are retro-reflected by mirrors outside the chamber serve for the obligatory trapping lasers which we call MOT beams.

This setup would already be sufficient to trap atoms, however given our MOT detuning of $\delta_1 = -8.2$ MHz most atoms would still escape the trap since they leave the slower with an approximate longitudinal velocity of $v_z = 36$ m/s. This final velocity is deliberately chosen as a reasonable compromise between longitudinal cooling and transversal divergence of the atom beam [33]. This ensures that the transversal velocity of the atoms does not dominate the propagation between ZSL and MOT region. For the purpose of specifically slowing longitudinally fast atoms, the booster laser beam is introduced. The booster counterpropagates the atomic beam with a detuning sufficiently larger than the MOT detuning with $\delta_b = -26.2$ MHz. Together with the trap B-field it therefore acts like a second Zeeman slower. This way the velocity of the the atoms can be decreased to match the MOT capture velocity directly in the vicinity of the trap.

δ_1 [MHz]	δ_b [MHz]	s_{01}	s_b
-8.2	-26.2	1.0	1.1

Table 5.1: Overview of the currently set MOT parameters.

5.2 Measurement Scheme

We conducted experiments on the single and double frequency MOT with the objective of enhancing the total ^{39}Ar count rate. Unfortunately, the natural abundance of this argon isotope is extremely low resulting in count rates of only a few atoms per hour for atmospheric samples. Optimizing the signal of a ^{39}Ar-MOT would therefore be a very long, unsufficient and unsatisfying process. In order to generate a trapped atomic cloud with a higher density where changes on the setup are more visible we choose to perform the experiment on ^{38}Ar atoms, which are by a factor of 10^{12} more abundant. Once the capture efficiency of the ^{38}Ar-MOT is optimized the knowledge can be transferred onto ^{39}Ar atoms. All presented measurement data were generated by experimenting with the ^{38}Ar-MOT.

As the atoms are spatially confined inside the trap by laser light they scatter photons repeatedly. The number of fluorescence photons therefore correlates to the number of atoms in the MOT and can be quantitatively monitored with a CCD camera. Keeping in mind the scattering rate introduced in chapter 3, eq. 3.20, fluorescence light intensity does not only depend on the quantity of atoms captured, N, but also detuning δ and intensity $I(s_0)$ of the trapping beams. Just

optimizing the MOT parameters to yield high intensity fluorescence would therefore not necessarily achieve a higher capture efficiency.

The for this thesis newly implemented measurement scheme aims to avoid these problems by introducing two sets of MOT parameters. In the loading mode the frequency of the MOT light can be changed as well as the frequency and the intensity of the additional laser. After a definable time the system switches to the detection mode in which the second laser is shut off and the MOT frequency is adjusted to a pre-set value. Shortly after this the camera is triggered for one picture. With this setup it is possible to make changes that do not affect the fluorescence signal at the moment the data is taken.

As already explained in the previous section, most frequencies required for the operation of the apparatus are attained by passage of the laser beams through AOMs. These are controlled by one AOM driver each. The driver uses a voltage controlled oscillator (VCO) which generates a frequency depending on the applied voltage. For the operation of an AOM there are several available prospects provided by the driver, like turning it on and off via a TTL signal. During the time when 5 V are applied, the connected AOM is switched on and the respective laser beam can enter the apparatus through a fiber, otherwise the beam is blocked. Furthermore we can control the frequency of the AOM by applying a voltage between -10 V and 10 V to the driver corresponding to a $\sim$40 MHz detuning range.

For realizing the double frequency MOT we actually need an additional laser beam inside the MOT fiber with variable detuning and power which is mostly independent from the rest of the laser setup. Since we exclusively observe the argon isotope ^{38}Ar, which has no hyperfine structure, the necessity for repumpers is obsolete. This enables us to reuse the second repumper beam for this second trapping laser since its frequency can be changed (together with the 3rd RP) independently from the trapping beams with an offset lock (Slave 2, see figure 4.2) and it is already coupled into the MOT fiber. Note that changing the repumper frequencies inside the MOT affects the repumper beams for the collimator in the same way so that optimum performance is here not longer guaranteed. However, blocking the other repumpers and the MOL prevents unwanted effects to happen on the atomic beam and we can be sure that our MOT can now be operated as a double frequency MOT. Power can be varied by changing the relative power of the repumper beams with a $\lambda/2$ waveplate and polarizing beam splitter combination in front of the fiber.

Going back to the measurement scheme we now address the quench, second repumper and MOT AOM driver independently by one function generator each (Agilent 33250A). The camera trigger is taken from the quench function generator internal trigger. In order to avoid confusion with the original purpose of the second repumper laser beam it will be denoted as second frequency (or 2nd frequency) from now on.

Figure 5.2 shows a schematic time diagram of the function generator outputs. The sequence starts with the loading mode, indicated by the rising edge of the quench function generator voltage (orange). This switch of the master signal triggers the second frequency (blue) and MOT (purple) pulses. Considering the TTL signals of

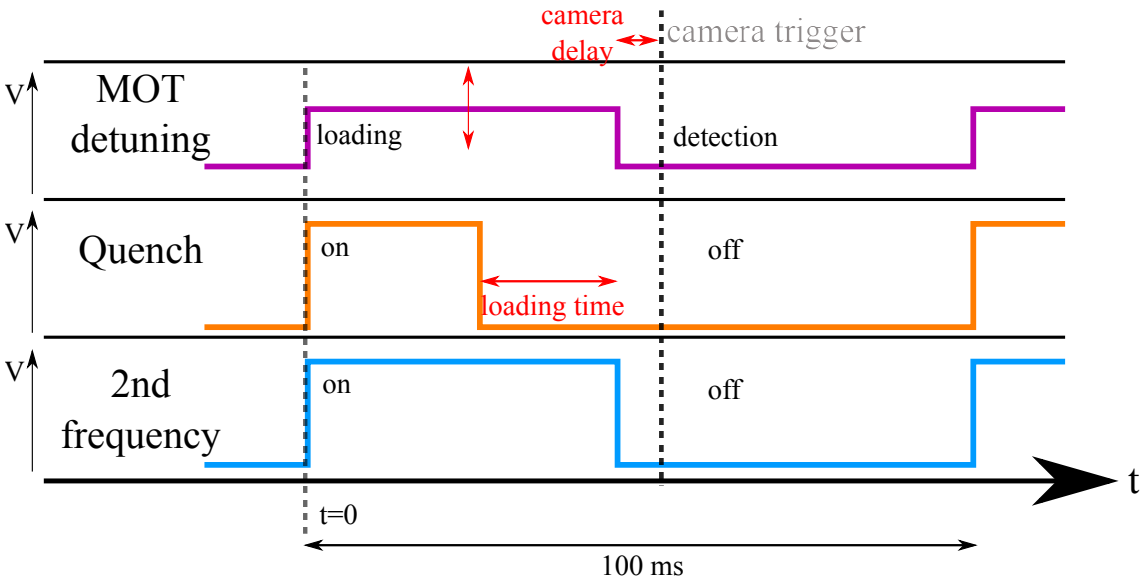

Figure 5.2: Schematic of a measurement sequence. The quench (orange) serves as a master and triggers all other function generators. Second frequency (blue) and MOT detuning (purple) have a fixed pulse time of 50 ms whereas the quench pulse time is variable. The camera triggers with the falling edge of the quench synchronizing signal (not shown) and is indicated by the dotted line. Delay time of the camera (typically $\sim 20\mu$s) and loading time (0 – 50 ms) are shown in red, not to scale. The vertical arrow across the loading mode MOT detuning voltage indicates the tuneability of this value.

quench and 2nd frequency they are both switched on in the beginning. The MOT AOM driver is not externally turned on and off but the applied voltage shifts the VCO frequency so that the detuning δ_1 (first frequency) can be controlled. The quench light is pumping the ^{38}Ar atoms back to the ground state and therefore actively keeps the trap empty [45]. As soon as the quench pulse ends, the loading of the trap begins until the 2nd frequency is switched off and the MOT changes to detection frequency (shown here by a lower voltage). This event defines the beginning of the detection mode.

The camera is triggered by the falling edge of the quench function generator synchronizing signal with a variable delay to the detection mode switch. In figure 5.2 this is indicated by a black, dashed vertical line. The loading time of the trap is given by the time interval between turning off the quench and switching to detection mode and can be tuned by shortening the quench pulse. This way the loading time can be varied from 0 ms to $<$ 50 ms (the quench needs to be switched on in the beginning of every sequence to totally empty the MOT). One sequence of loading, picture taking and emptying the trap is fixed to a frequency of 10 Hz.

It is important to note that also during the detection mode the loading processes

in the trap continue. However, the delay of the camera is chosen to be very short ($\sim 20\mu s$) and these effects can therefore be neglected for the fluorescence image.

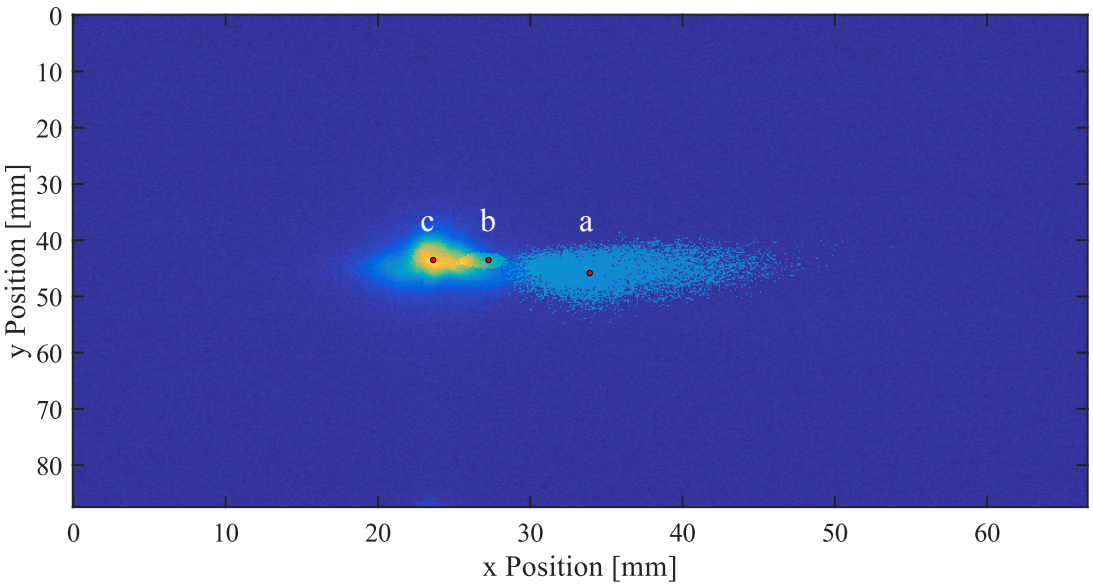

Figure 5.3: Loading of the MOT: Pictures taken with the CCD camera outside the chamber after 2 ms (a), 6 ms (b) and 10 ms loading time (c). Marked is the center of the cloud.

Before this measurement scheme is applied to observe various MOT configurations, we take a closer look whether this new tool is a useful and reliable one. It is necessary that the cloud is at any time fully visible by the camera. This is especially important for MOT loading experiments since the cloud might slightly shift during the loading process. Also the distinction between loading and detection mode needs to be clear and the choice of the detection frequency should not affect relative differences between two signals.

Taking pictures of the atom cloud after certain loading times enables us to reconstruct the spatial position and dimension of the cloud. Figure 5.3 shows the position and density of the trapped atom cloud after 2 ms, 6 ms and 10 ms loading time. It can be seen that the position changes slightly within the range of the camera detection window. Taking a longer loading time, the trapped cloud gets more dense and brighter which directly correlates to more atoms being inside it. The shift in position is caused by the way the atoms interact with MOT laser beams and booster. Since most atoms have a longitudinal velocity sufficiently higher than the MOT capture velocity, they scatter light from the booster until they are slow enough to be captured. They escape the center of the trap first and are then pushed back into the MOT region and captured. Although the position of the cloud shifts slightly it is always close to the center of the camera window and we can assure that the pictures taken will be reliable.

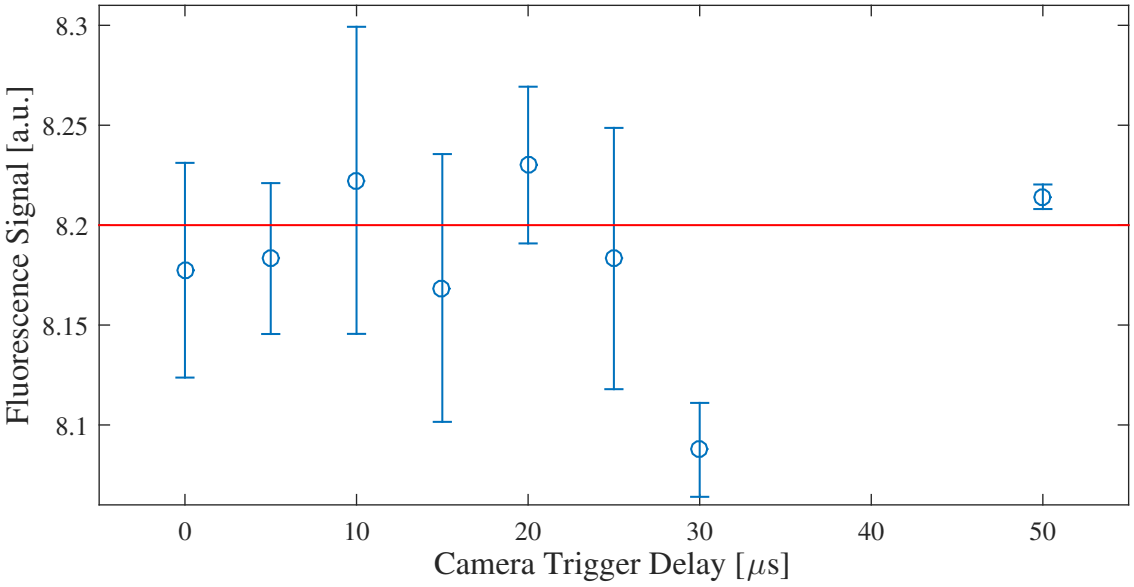

Figure 5.4: Fluorescence of the cloud over camera trigger delay: Loading time was chosen to be 8 ms, two frequencies. The solid line (red) is a guide to the eye.

In order to examine whether the AOM drivers are switching the measurement modi fast enough, the shutter of the camera can be set to an arbitrary time delay. Changing this in an interval of 0 to 50 μs showed no considerable effect on the atomic fluorescence intensity as can be seen in figure 5.4. It shows the fluorescence of the cloud over camera delay. The errors shown correlate to the error of the mean from three pictures. Examining the fluorescence signal we can see that almost all data points lie within their errors on one line of constant signal. For the value at 30 μs this is not true, it deviates from the other data possibly due to a systematical measurement error. Still we can assume the change between the modi to be faster than the camera trigger timescale. However, to be very sure that the switch does not affect camera pictures, the delay was set to 20 μs for all pictures.

Additionally, the effect of the detection frequency on the fluorescence signal was analyzed. For the single and double frequency case each the MOT fluorescence signal was measured twice. Whereas the MOT loading and second frequency detuning stayed the same, we varied the detection frequency of the MOT. It showed that the ratio of two signals at different measurement setups was not affected by the detection frequency chosen. Anyways, the detection frequency was not changed over the course of the measurement and was set to $\delta_d = -8.0$ MHz.

5.3 Single Frequency MOT

With the implemented measurement scheme we first like to study the behaviour of a single frequency MOT. This allows us to get a deeper understanding of the current system and also to check the agreement of theory and experiment. It is necessary to remark that the booster is inside the MOT chamber at any time and not blocked nor controlled by a function generator. This ensures that the system is as close to the current measurement laser setup as possible. For a better evaluation of the data ten measurement cycles/pictures are taken into account per data point. A statistical error is displayed in each figure which is computed as the error of the mean from the ten frames. It is essential to know that some measurements were not taken on the same day. Various changes on the apparatus might affect the absolute value of fluorescence so that every day a reference curve similar to figure 5.5 was taken which serves for comparison between data obtained at diverse times and as an absolute reference for all loading curves.

Besides the daily fluctuations of the apparatus, the fluorescence signal of the MOT underlies steady vacillation which occur due to drifts in the trapping beam polarization. When adjusting the polarization it is always paid attention that the fluorescence is kept at an uncritical point where small changes do not have a strong effect. Still a longtime drift can not be prevented. This additional error is hard to observe and not included in the displayed data but its existance has to be kept in the back of our minds. Other systematic errors include fluctuations of laser intensity and frequency as well as variations in the source performance.

Figure 5.5 shows a typical loading curve of the ATTA MOT with a detuning of $\delta_1 = -8.0$ MHz and $s_{01} = 1.0$. These parameters are the current system settings (the detuning differs slightly from the previously chosen detuning of $\delta_m = -8.2$ MHz).

The curve (and also the later curves) shows an offset that can be explained by the corrections done on the data before displaying it in a figure. After every measurement (like one loading curve) background data was taken in ten frames. Here background refers to a signal with no atoms in the chamber, whereas the argon flux was cut-off by closing a valve behind the MOL. At 0 ms loading time atoms are present in the MOT chamber and although they are not captured they scatter light from the laser beams into the camera which generates a signal higher than the background signal.

In an usual loading process the captured atom number N is described by the ordinary differential equation

$$\frac{\mathrm{d}N}{\mathrm{d}t} = R - \alpha N - \beta N^2, \tag{5.1}$$

depending on the loading rate R and the linear loss coefficient α for one-body losses and the two-body loss coefficient β [46]. Eq. 5.1 suggests that the beginning of the loading process can be approximated by the linear function $N = R \cdot t$. Therefore R can be directly extracted from the loading curve as the slope at very short times.

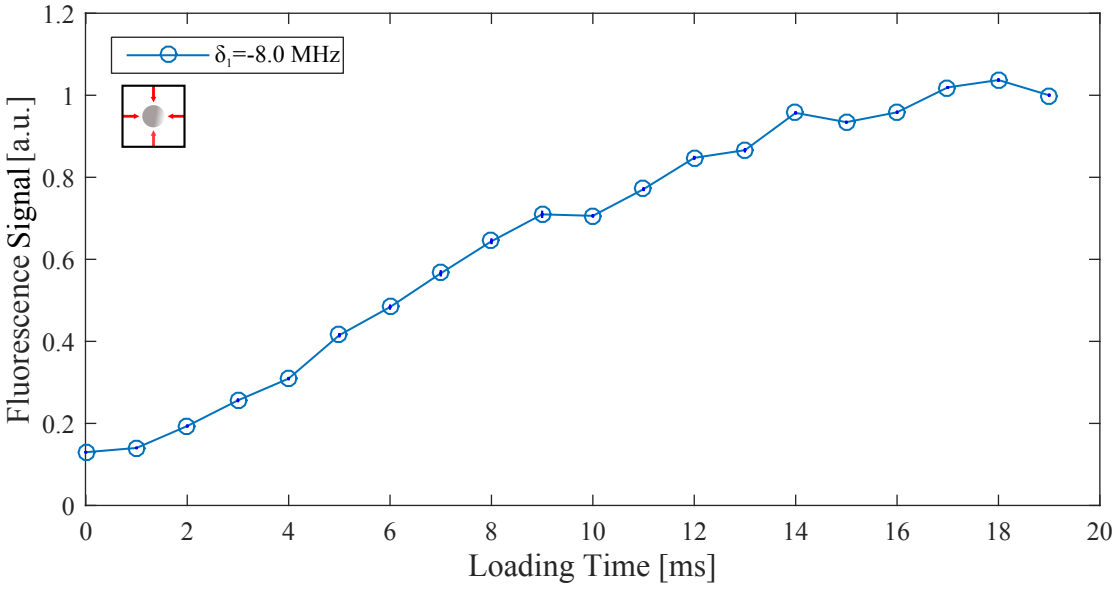

Figure 5.5: Loading curve: Fluorescence signal over loading time for the single-frequency MOT with $\delta_1 = -8.0$ MHz, $s_{01} = 1.0$. Small icons displayed in the graph should indicate whether the single or double frequency MOT is shown.

Figure 5.5 seems to exhibit a slightly different rising process. This effect might be caused by the booster as suggested in [32]. As already pointed out before, the current MOT detuning is not high enough to directly capture the atoms from the ZSL. The atoms first pass trough the MOT center without being captured while experiencing a decelerating force from the booster. Before the atoms exit the trapping beam region they reach the capture velocity and are trapped. Due to this, it takes longer than in an ordinary MOT until the atoms are captured. This expresses in the slowly increasing atom number in the beginning.

Another explanation is that the loading rate is affected by the way the measurement scheme is designed. Keep in mind that a flux of argon atoms is constantly flowing through the trap and just the ^{38}Ar quench prevents them to be captured. In this setup the quench actively keeps metastable atoms out of the MOT region by exciting them to a state where they will eventually decay back to the ground state, making them unaccessible for the cooling laser. As soon as the quench laser is switched off, metastable atoms can enter the trapping region where the MOT beams are constantly present. The diameter of the beams which enter the chamber through the MOT fiber is 32 mm, therefore this applies also to the quench. While the quench is in the chamber, it therefore deexcites all atoms within a sphere of 16 mm radius.

The capture range of the trap is defined by the force acting on the atoms and was calculated in [4] to be $\sim$ 10 mm in longitudinal direction for a detuning of $\delta_1 = -8$ MHz. As soon as the quench light is turned off, the atoms need to cover

a distance of ∼6 mm in order to reach the trapping region. Given this distance the atoms would need to have an average velocity of 3 m/s in order to cause a loading delay of 2 ms. This seems a bit slow but considering that the booster already cooled the atoms (the B-field extends over $\sim$ 50 mm) this might be a reasonable velocity. Since the atoms are not of uniform velocity some might reach the trap faster than others, resulting in the slow rise of fluorescence in figure 5.5.

Usually the loading starts as soon as the trapping beams are switched on and the trap can be directly loaded by atoms which are within the capture range of the MOT. This results in a linear increase in the beginning.

The linear regime starts only after 3 ms and at ∼17 ms N converts into a steady state in which the loading rate compensates the losses. This presents in the constant fluorescence signal. It is important to note that changes on the setup affecting the loading rate should show their strongest effects in the linear regime. Since the loading process is dominated by R this is the parameter we want to optimize. When capturing ^{39}Ar the MOT is mostly filled with only one atom setting two-body losses to zero.

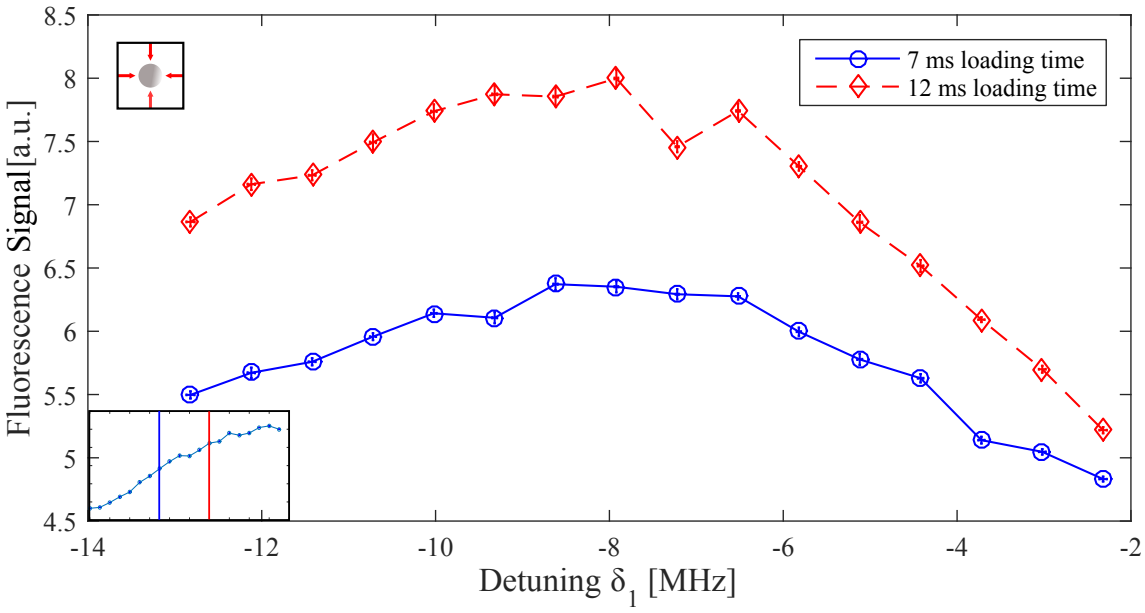

Figure 5.6: Fluorescence signal over detuning of the laser beam relative to resonance frequency of the transition. Measured for 7 ms loading time, shown by the solid curve (blue), and 12 ms shown by the dashed (red) curve. In both cases $s_{01} = 1.0$. The icon in the lower left corner displays the loading time in figure 5.5.

The force transferred by a laser beam onto an atom crucially depends on its detuning as shown in eq. 3.43. In order to find out which detuning is most suitable for capturing many atoms we measure the fluorescence signal of a cloud after several ms loading for different detunings δ_1. Figure 5.6 shows the cloud fluorescence over

detuning δ_1 for two loading times, 7 ms and 12 ms. We can see that for both curves the signal decreases on either side of the maximum at $\delta_1 \approx -8$ MHz. The upper, dashed (red) curve referring to a loading time of 12 ms shows a stronger arch whereas the lower, solid (blue) curve measured at 7 ms loading time appears to be more flat.

Let us first examine the solid (blue) curve for a loading time of 7 ms. Here we are in the regime of short times and small N, therefore two-body losses are not strongly influencing the signal yet. The curve decreases very symmetrically since the loading rate, which is mainly dictating the atom number for these times, is dominated by the detuning δ_1. Since the atoms emerging from the Zeeman slower have a certain velocity distribution, there is an optimal detuning which serves best for capturing atoms of the most occuring velocity. Figure 5.6 suggests that this detuning is $\delta_1 = -8$ MHz. This is caused by the booster, which is already optimized to this frequency. Previous analysis of the trap found $\delta_m = -8.2$ MHz to be the a suitable detuning together with a coil current of I =10.7 A, being a well trade-off between capture of fast atoms and high scattering rate for detection [33],[32].

Taking a closer look on the dashed (red) curve it reveals a strong decrease towards the right side of the plot, whereas the left side seems to be simply an upward shifted copy of the corresponding solid part. The change of detuning does not only affect the loading rate R which dominates the blue curve but also the strength of two-body losses that have a heavy effect at higher loading times. While the trap captures more atoms, the cloud gets continuously denser whereas a critical density is reached when losses counterbalance the number of incoming atoms. The detuning has influence on the size of the cloud in which an increasing detuning yields a bigger MOT as derived in eq. 3.47. For very small detunings the cloud shrinks causing the density n to increase if N stays constant. The loss coefficient β grows also, since the atoms are more endangered by collisions between each other as n gets bigger. A rapid reduction of the fluorescence signal can be observed.

At its maximum the dashed (red) curve is a factor of 1.27 times higher than its solid (blue) counterpart. Comparing this to the ratio of MOT fluorescence signal at 7 ms and 12 ms loading time taken from figure 5.5, which obtains a factor of 1.26, the two measurements show good agreement.

Another parameter that has strong effects on the fluorescence signal is the on-resonance saturation parameter s_{01}. For the data shown in figure 5.7 the saturation intensity was changed under observation of the cloud fluorescence. The current function generator setup does not allow for the change of intensities of this laser beam since this would require a fourth function generator so that the intensity had to be tuned directly in front of the fiber monitoring the power on a FPI. Problematic about this procedure is that not only the MOT power in the loading sequence changes but also for the detection. This purges the benefit of an independent detection sequence but still figure 5.7 shows the effect of s_{01} on the scattered light intensity.

As the force on the atoms increases approximately linearly with s_{01} for $s_{01} < 1$, see eq. 3.43, the loading rate and therefore the fluorescence signal should behave the same. This increase is sketched by the solid straight curve (red) in figure 5.7. Due to the fact that the detection intensity changes as well the curve displays a different

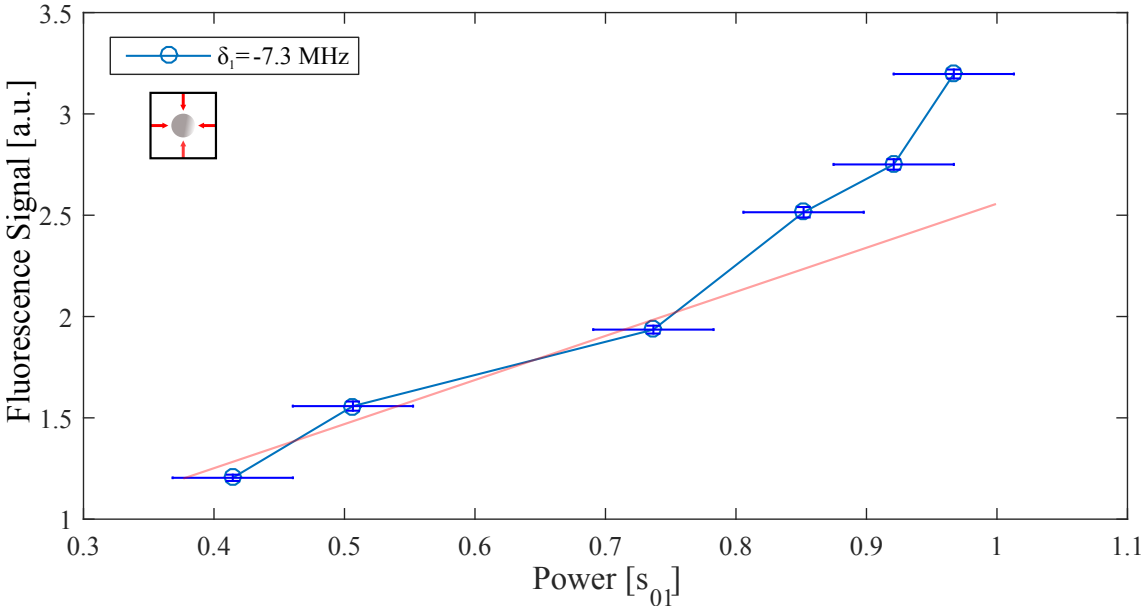

Figure 5.7: Fluorescence signal of the cloud over laser power at a detuning of $\delta_1 = 7.3$ MHz. The solid straight line (red) displays a possible linear increase of the signal.

rise. The scattering rate of the trapped atoms at the moment of the camera trigger increases with power, resulting in a steeper slope than we would expect. If the power grows further the force should saturate resulting in a saturation of the fluorescence signal for high intensities. Unfortunately this can not be observed since the intensity of the detection beams also increases.

5.4 Double Frequency MOT

The introduction of a second frequency into the MOT chamber is believed to be one possible way to increase the loading rate of our atom trap and therefore obtaining a higher count rate for the ^{39}Ar ATTA.

Figure 5.8 shows three loading curves for different detunings of the second frequency while one being the reference of the current single frequency system. All of the curves exhibit the same rising anomaly as the one displayed in figure 5.5. They start to evolve independently after 4 ms with the separation between single and double frequency curve growing in time until all saturate after ∼17 ms loading. Finally the data for the double frequency case presents a signal a factor of ∼1.2 times higher than that for the single frequency setup.

Primarily a second detuning $\delta_2 > \delta_1$ generates a trap which allows for the capture of fast atoms that could not be sufficiently cooled by the booster to be captured by δ_1. The capture velocity increases with the detuning as can be seen in figure 3.4. A

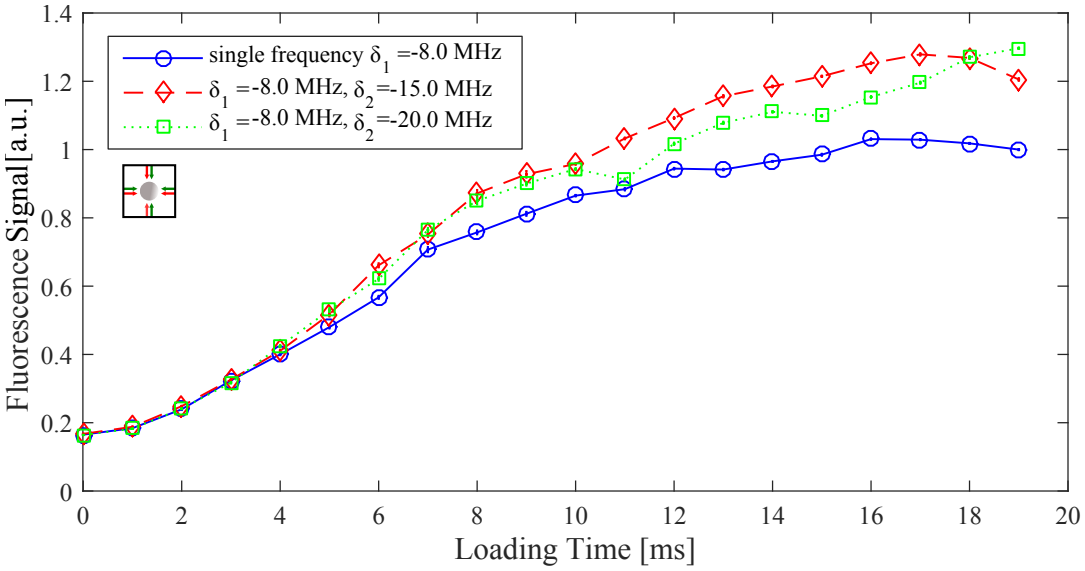

Figure 5.8: Loading curves for different detunings. Shown by the solid (blue) curve is the loading behaviour for the single frequency case from fig. 5.5 with $\delta_1 = -8.0$ MHz and $s_{01} = 1.0$. The second frequency is introduced with a detuning of $\delta_2 = -15.0$ MHz, shown by the dashed (red) curve, and $\delta_2 = -20.0$ MHz, shown by the dotted (green) curve. For both δ_2 the power was set to $s_{02} = 0.6$.

higher detuning enables the compensation of a bigger Doppler shift and with that the effective deceleration of a fast atom. Therefore the loading rate increases. In a simplified picture where the forces of the two traps just add up, and $\delta_1 < \delta_2 < \delta_b$, we can imagine the behavior of the atoms to be like this: The atoms are cooled by interaction with the booster until they are slow enough to be captured by the second frequency. They scatter the second frequency light until they reach the capture velocity of δ_1 and enter the narrow trap. Inside this trap they experience a higher scattering rate due to the more resonant laser frequency.

In reality interference effects of the laser beams need to be taken into account, as can be seen in eq. 3.31 for the scattering rate in a double frequency configuration. The statement that a second high detuning allows for the capture of fast atoms still holds true. Besides that, a high second detuning generates a spatially wider (eq. 3.47) and therefore less dense cloud enabling the reduction of two-body losses.

Taking a closer look on the regime of small loading times we can observe the same non-linear rising process between all three curves in figure 5.8. Previously, when analyzing the data for the single frequency curve, we assumed this to be caused by the interaction of the atoms with the booster. Another approach was that the process is caused by the delay due to the flight time from the edge of the quench region towards the MOT capture region. As already pointed out, a higher detuning should increase the capture range of the MOT as it was already shown in [4]. Extracted from [4], the trap radius should be ∼20 mm for a detuning around

-20 MHz. Since the radius of the laser beams is the limitation for this quantity, the capture radius for the second frequency MOT should be $\sim$16 mm (equal to laser beam radius). This would disprove the idea that the time of flight is causing the loading process in the beginning, since for this case both quench radius and capture radius are equal and the time of flight should therefore be zero. Still the atoms are not directly captured, because this would relate to a linear increase at the start. Thus this anomaly seems to be caused by the booster-atom interaction. The deceleration of the fast atoms is achieved by scattering light from the farer red detuned booster until they reach the capture velocity of the trap. This displays in the slow rising of the curves. Even for the double frequency MOT the booster still serves its duty, since both $\delta_2 < \delta_b$.

In the linear regime from 4 ms to 9 ms the single and double frequency MOT loading curves show a different behaviour. For this time interval, we do not have to consider the two different second frequency detunings seperately, since they display the same rise. However, the single frequency curve is clearly distinguishable from the others and lies at any point underneath those. With increasing time, the single and double frequency curves split up stronger. This indicates a higher loading rate R_2 for the double frequency than for the single frequency MOT R_1. Since in this time regime the atom number and MOT density is not very high, atom losses play only a minor role. The atom number can be approximated by $\frac{\mathrm{d}N_{1,2}}{\mathrm{d}t} = R_{1,2} \cdot t$ and we can compare the slopes for single and double frequency curves. Considering only the time span from 4 ms to 9 ms we can extract from the figure $R_2 \approx 0.1$ and $R_1 \approx 0.07$ which would result in $R_2 \approx 1.4 \cdot R_1$. The loading rate is therefore increased by a factor of 1.4 with the introduction of the second frequency.

From 9 ms on the curves flatten. Losses now hinder the loading of more atoms and the increase of atom number is not linear anymore. Loading still continues until the losses compensate the loading rate $R = \alpha N_s + \beta N_s^2$ (eq. 5.1 for the steady state where $\frac{\mathrm{d}N}{\mathrm{d}t} = 0$) and the atom number saturates to N_s. It can be clearly seen that for the double frequency case the steady state atom number $N_{s,2}$ is higher than for the single frequency case $N_{s,1}$. This is caused by the higher loading rate and possibly also by the increased MOT size compared to single frequency. The smaller density decreases the loss factor β and therefore enables the loading of more atoms.

We can also observe that the double frequency curves separate whereas the $\delta_2 = -15.0$ MHz curve lies slightly above the $\delta_2 = -20.0$ MHz data. It might be that the smaller second frequency detuning enables the capture of more atoms because it works better in cooperation with the booster than a higher detuned frequency. Regarding a possible longtime drift of the MOT fluorescence between the measurements of the two curves they are well comparable, anyhow both double frequency loading curves show a clear distinction from the single frequency case.

It is still questionable if the stronger fluorescence signal is only achieved by the higher laser intensity present in the MOT beams. If so, the insertion of the second frequency would cause a gain even if the two detunings are chosen to be equal. In order to investigate this, we set δ_2 to the same value as δ_1 and took a loading curve. The result is shown in figure 5.9 whereas the solid (blue) curve again displays the

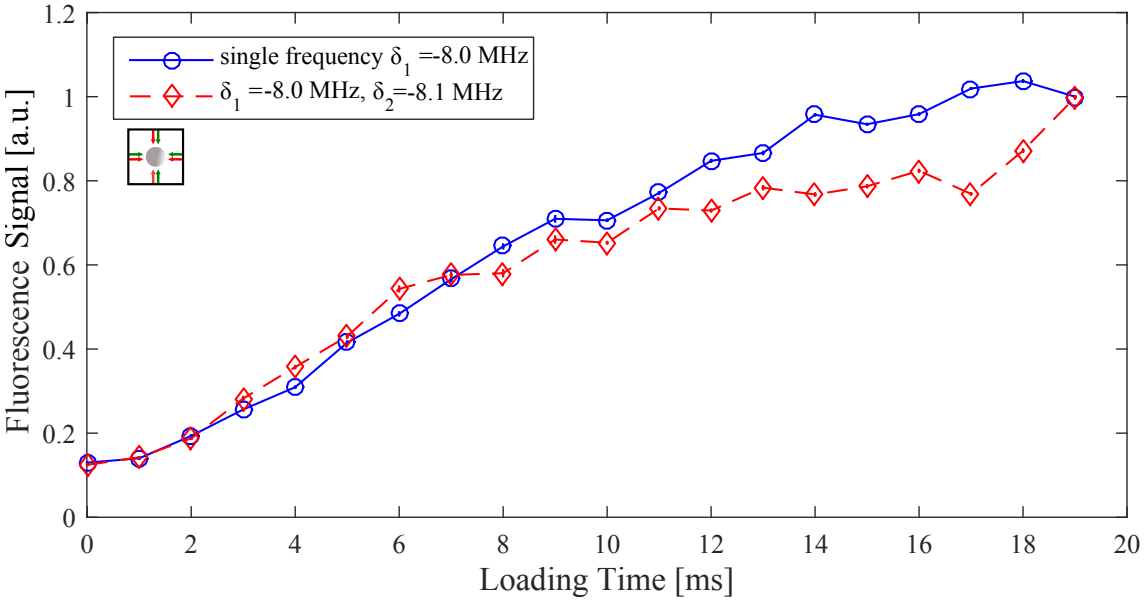

Figure 5.9: Loading curves for the single frequency case (solid, blue) and a double frequency configuration (dashed, red) whereas $\delta_1 = -8.0$ MHz and $\delta_2 = -8.1$ MHz, $s_{02} = 0.6$, $s_{01} = 1.0$.

single and the dashed (red) curve the double frequency configuration. It can be seen that in both cases the loading starts very similar until after 11 ms the blue curve overtakes the red one resulting in a noticeable gap between the two. The similarity of the curves in the linear regime correlates to the loading rates for the two cases being equal. This would mean that a second laser beam does not directly produce a higher loading rate but only if the detuning is chosen right. At first glance this seems to not match the expected forces inside the MOT since according to eq. 3.43 a higher intensity should increase the scattering rate, and therefore the light force.

Besides this, the saturation regime for longer loading times seems to behave not as expected. If the loading rates are equal for the two curves they should also behave the same for times when losses are getting more important. In figure 5.9 it can be seen that the losses for the double frequency case are larger resulting in a stronger flattening.

It might be that the higher power of the same deuning brings about other effects which were not considered before. In the very beginning of the thesis we made the approximation of low intensities in order to simply add up the forces from two opposing beams. High power inside the MOT beams facilitates stimulated emission and can therefore introduce additional heating effects which increase the losses in a dense trapped cloud. In the case we observed in figure 5.9 these higher losses might cause the dashed curve to flatten sooner and saturate to a lower atom number.

On the other hand, the transition linewidth is also influenced by the laser power.

Eq. 3.20 can be rewritten as

$$\gamma_p = \frac{s_0}{1+s_0} \cdot \frac{\gamma/2}{1+(2\delta/\gamma')^2} \tag{5.2}$$

with the linewidth $\gamma' = \gamma\sqrt{1+s_0}$ of the transition. This new atomic transition linewidth enlarges for bigger saturation parameters resulting in an effect called power broadening. The current single frequency setup features a saturation of the cooling transition of $s_{01} \approx 1.0$, the insertion of the 2nd repumper increased this to $s_{01}+s_{02} \approx 1.6$. The corresponding linewidths are $\gamma_1' = 8.4$ MHz and $\gamma_2' = 9.6$ MHz. The concept of the MOT relies on the Zeeman effect, whereas B-field and laser polarization is chosen such that atoms mostly scatter photons from a beam that accelerates them towards the center of the trap whereby they are effectively cooled. A broader linewidth of the atoms might cause them to also experience the opposite beam as resonant and scatter light coming from it. A momentum kick towards the outside direction is therefore transferred onto the atom and the cloud heats up. Especially a dense MOT might suffer from an increasing loss rate due to this broader linewidth.

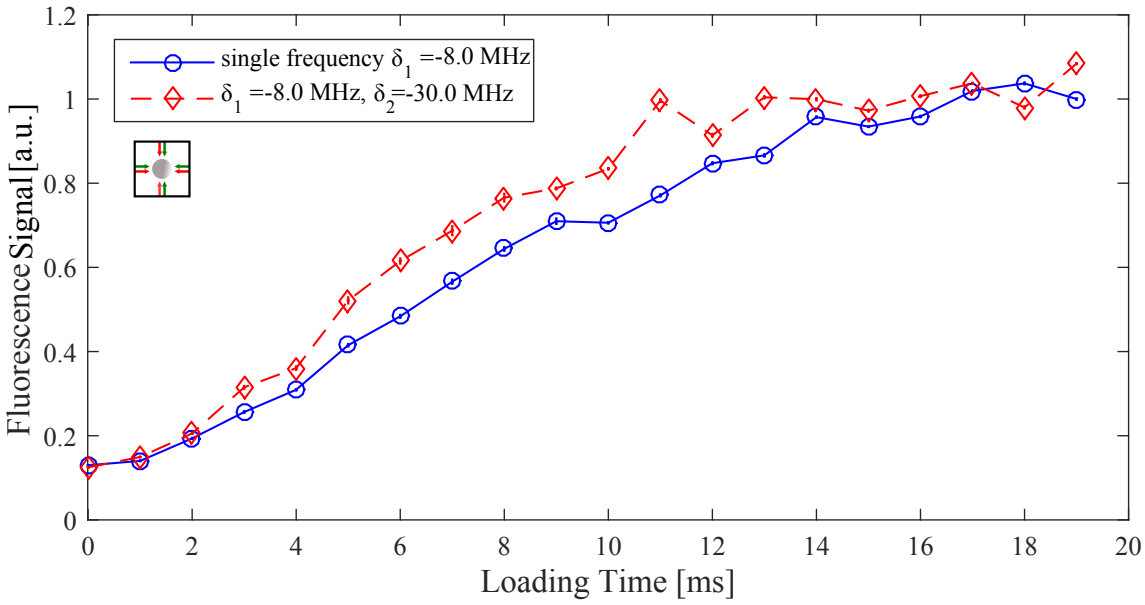

Figure 5.10: Loading curve with a high second frequency detuning of $\delta_2 = -30.0$ MHz (dashed, red), $s_{02} = 0.6$, $s_{01} = 1.0$. As a reference the single frequency data is shown by the solid curve (blue).

The situation is again different for a detuning δ_2 which is chosen to be comparable to the booster detuning $\delta_b = -26.2$ MHz as displayed in figure 5.10. Keep in mind that the geometry of our MOT setup causes an intersection angle of 45° between the horizontal trapping lasers and the propagation direction of the atom beam, whereas the booster counterpropagates the atom beam yielding an intersection angle of 180°. Therefore the detuning of the trapping beams relative to the longitudinal

velocity is lowered by a factor of $\cos(45°) = 0.71$ and $\cos(45° + 90°) = -0.71$ respectively (see figure 5.1). The booster detuning is experienced by atoms at rest to be 26.2 MHz since $\cos(180°) = -1$. In order to compare second frequency detuning and booster detuning for figure 5.10 we need to consider the experienced detunings $\delta_b = 26.2$ MHz and $\delta_2 = -0.71 \cdot 30.0$ MHz$= 21.2$ MHz.

Looking at the behaviour at small loading times it seems that the second frequency (dashed, red) enables a faster capture here. This is displayed in the rise at 3 ms. Still the loading process does not show a linear increase in the beginning which might be caused by the interaction with the booster as already explained before. The slightly steeper rising in 5.10 compared to the previous double frequency curves could be caused by the higher second detuning applied here. It enables the capture of fast atoms directly as they reach the trapping region first after turning off the quench.

After the separation from the single frequency curve after 3 ms the double frequency loading curve increases faster than its counterpart until at 6 ms a relative distance between the two curves of a factor of $\sim$1.3 is established. The gap reduces towards higher loading times until both curves saturate to almost the same MOT fluorescence signal. Considering the linear part of the signal between 5 and 9 ms the slopes of two are equal. This means that for both cases the loading rates are the same. Nonetheless the double frequency curve has an offset which is caused by the faster increase of atom number at short loading times.

Still the double frequency curve should saturate to a higher atom number in the end, because the cloud is more extensive for the double frequency case with a higher detuning, as can be derived from eq. 3.47. This results in a smaller density and therefore in a decrease of the two-body loss coefficient β. This would cause $N_{s,2}$ to grow, even if the loading rate R_2 is the same. Contrary to our expectations the dashed curve saturates approximately to the same value as the solid curve. This could be because the second frequency not only captures the fast atoms with $v_z \leq v_{c2}$, but also interacts with the very fast atoms which have a longitudinal velocity bigger than the capture velocity, and focuses them to the MOT center where they can collide with the already trapped atoms. This might lead to a higher one-body loss especially when the MOT density is high.

In comparison, a second frequency with a smaller second detuning, which is higher than the original MOT trapping beams detuning does yield a higher capture efficiency even after saturation. Considering figure 5.8 –5.10 it seems that for enhancement of the capture efficiency a detuning δ_2 between -10 and -25 MHz is a reasonable choice.

Next we would like to take a closer look onto the dependency of the capture efficiency on the relation between the two detunings. Figure 5.11 shows the MOT fluorescence signal over the detuning δ_1 for different settings of δ_2. All of the curves were taken after 7 ms loading time since here direct changes on the loadingrate R can be seen. The lowest, solid curve (blue) is the reference of a single frequency MOT taken from figure 5.6. After the launch of the second frequency the maximum of the curves is still at $\delta_1 \approx -8$ MHz. The three graphs present a very similar arch while being slightly shifted on the y-axis, whereas the data of the double frequency MOT

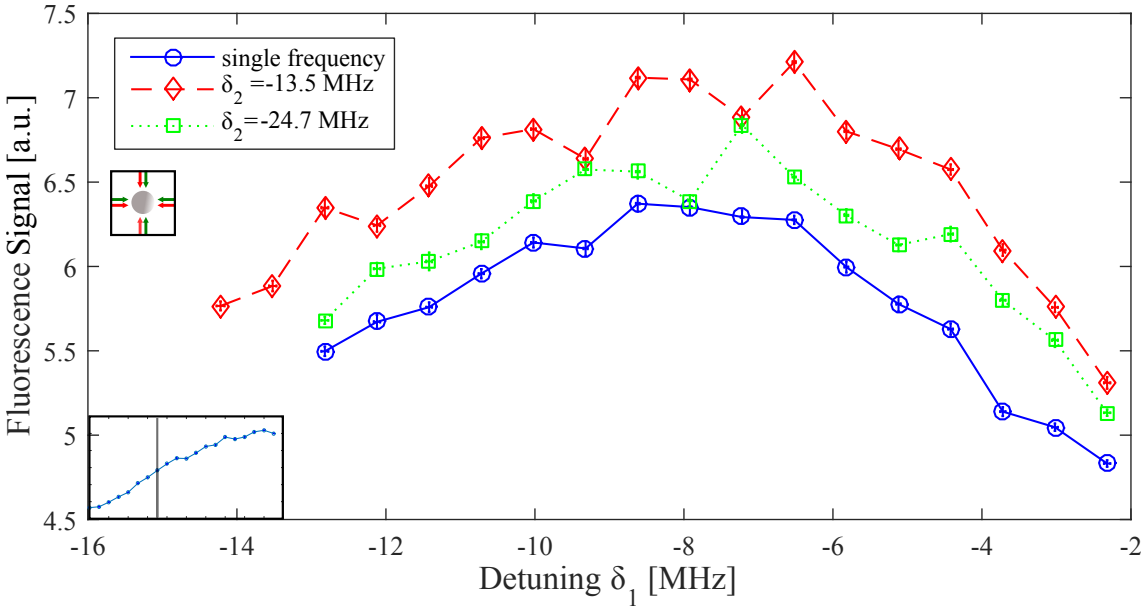

Figure 5.11: MOT fluorescence signal over detuning of the first frequency δ_1 for three different setups with $s_{01} = 1.0$. The solid (blue) curve displays the previously shown single frequency data as reference. Shown by the dashed (red) curve is the signal for $\delta_2 = -13.5$ MHz and by the dotted (green) curve for $\delta_2 = -24.7$ MHz. It is $s_{02} = 0.4$ for both. All data was taken after 7 ms loading time.

shows a higher total fluorescence signal originating from an enhanced loadingrate. Towards the wings of the curves the relative distance between them stays constant which is a sign for the capture efficiency being governed by the loading rate and not two-body losses which depend on δ_1 and δ_2. For a detuning of $\delta_2 = -13.5$ MHz the double frequency signal is $\sim$1.2 times higher than the single frequency signal at the maximum. For a detuning of $\delta_2 = -24.7$ MHz the enhancement is still $\sim$1.05 which suggests that $\delta_2 = -13.5$ MHz yields a higher capture efficiency than a higher second detuning agreeing with the results from figure 5.8, although this statement has to be taken with a pinch of salt considering the instability of the signal.

Finally we want to again observe the influence of the saturation parameter on the fluorescence signal. For the second frequency this experiment can be conducted in the desired sense since the second laser frequency is turned off during the detection process and a change in its power s_{02} can therefore not affect the magnitude of fluorescence light observed by the camera. As already introduced in the previous section, we expect the signal to saturate for $s_{02} \gg 1$ because the scattering rate reaches a maximum for infinetely high intensities. Figure 5.12 shows the fluorescence signal of our ^{38}Ar MOT for variable power of the second frequency beam. Going from zero intensity towards higher intensity the signal first rapidly increases and then starts to flatten. This shows a direct validation of the previously introduced

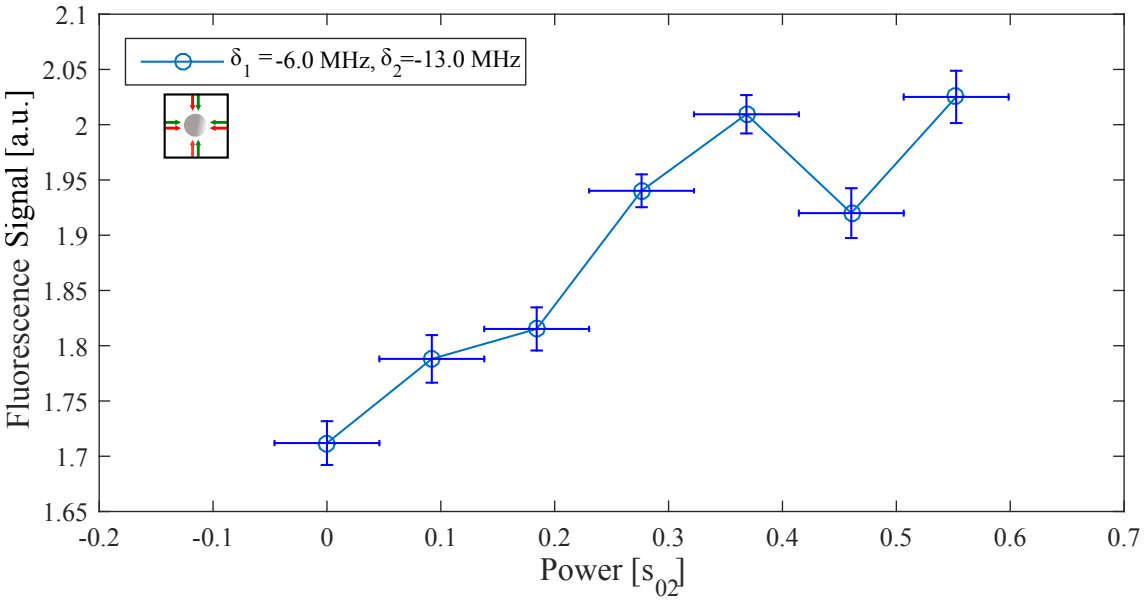

Figure 5.12: Power dependency of the MOT capture efficiency taken under variation of the intensity of the second laser frequency. The detunings were set to $\delta_1 = -6.0$ MHz and $\delta_2 = -13.0$ MHz. Loading time 7 ms, $s_{01} = 1.0$.

theoretical process.

6 Conclusion and Outlook

This chapter should give a short summary of the previously presented work on the ATTA machine. Since two experimental topics were adressed in the course of this thesis, the summary is divided into the corresponding two parts.

Laser Setup

At the beginning of this thesis, the plan for a new laser setup was already elaborated. The concrete setting started with reused optics and optomechanics from the previous setup together with some new components (Toptica DL Pro, new AOMs, new TA diodes). With the use of fibers, the laser components are now decoupled from the optomechanics setup. Additionally, the whole laser table is (and was already before) spatially separated from the vacuum chamber, whereas the laser light enters the experiment by fibers. These steps together with a newly designed temperature control increased the stability of the system significantly.

Stray light protected photodiodes were applied behind selected mirrors for observation of laser power of the reflected laser beam. Besides that, laser powers and frequencies inside the MOT fiber can be monitored with a FPI. Eventually the laser system provides the necessary laser frequencies and intensities for the operation of the ATTA machine and also the ability to monitor the whole system (see figure 4.6).

One major drawback of the previous setup was the low TA amplification factor. During this thesis the problem was tried to be solved by slight improvements on the TA design which were the insertion of a new copper mount and a new temperature control. The stability of the output was strongly improved due to the modifications. New TA chips ensure a high performance and stable operation.

With the new laser setup it was possible to continue measuring samples for days. The recycling measurement with a dead sample of small volume lasted 24 hours. From the resulting counts we determined the contamination acceleration of our apparatus to be $a = 0.045(5)$ ml STP/h. Besides that, a first study on samples measured in recycling configuration could be made. Compared to previous measurements conducted on groundwater [12], the recent experiments show similar preliminary results while decreasing the probe volume strongly. The samples of known concentration fit nicely to their measured concentration. This shows that dating of small ice and ocean water samples in recycling configuration is possible with ATTA.

Double Frequency MOT

In this thesis a new measurement scheme for the observation of the ATTA MOT was set up. It characterizes the MOT by measuring fluorescence light of the trapped atoms. Two different sets of parameters allow for the variation of trapping laser frequencies during one mode while maintaning the detection properties in the other mode.

This enabled us to investigate the behaviour of our current system. We confirmed the presently chosen detuning of $\delta_m = -8.2$ MHz to be the optimum for a high capture efficiency in cooperation with the booster. It is important to note that the B-field of the trap was not changed, since the measurement scheme relies on the benefit that the parameter values can be changed very fast. The magnetic field can only be tuned slowly and its optimization is therefore not practical for this measurement scheme.

First studies on a double frequency MOT with ^{38}Ar have been conducted. The second laser frequency was introduced through the same fiber as the first MOT frequency keeping position, size and polarization of the beams the same at all times. The introduction of a second frequency of proper detuning enhanced the loading rate of our trap. Besides this, the total atom number saturated to a higher value for the double frequency MOT due to the increased trap size. The enhancement in loading rate lies at a factor of $\sim$1.2 for a second frequency δ_2 between first MOT frequency $\delta_m = -8.2$ MHz and booster $\delta_b = -26.2$ MHz.

For the case of both detunings being equal no gain could be seen, the signal for two laser beams rather showed a decrease compared to the single frequency case at long loading times. This result confirms the assumption that the second frequency needs to be more red-detuned in order to achieve an increase in capture efficiency. A second detuning which was farer detuned than the booster showed a stronger increase in the beginning correlating to a faster loading, but no gain at higher loading times. In this case the loading rates for single and double frequency MOT were the same. In order to optimize the cooperation with the booster the detuning of the second frequency should therefore be chosen to be smaller than the booster detuning.

Outlook

Still the current TA design is not the optimum. Too many unnecessary degrees of freedom complicate the adjustment and endanger the stability of the amplifier. Currently a new ATTA branch opened featuring the new OpTTA (Optimizing Trap Trace Analysis) experiment. OpTTA aims to address questions about the ATTA machine that are still unanswered and might be sufficiently tackled by introducing ^{39}Ar enriched samples into the experimental chamber. For the first machine 'ArTTA' (Argon Trap Trace Analysis), this is not possible since enriched samples would contaminate our vacuum and future measurements with small sample sizes would be strongly determined by contamination background. The OpTTA team is presently

working on a completely new design of TAs adapted from that presented in [39]. This design reduces the optomechanics of the TA to a minimum while still providing the necessary alignment. Parallel to this, OpTTA seeks to study the metastable argon source since its full potential is not tapped yet.

In order to gain an improvement on the ^{39}Ar count rate, the effects of the double frequency MOT on this isotope should be investigated. For this application OpTTA would be an ideal solution since measurements with ^{39}Ar enriched samples can be done. This way the count rate increases and effects can be seen more easily. It would also be interesing to observe the effects the magnetic field has on the capture efficiency of a double frequency MOT. For the single frequency case this was already observed before [32], [33]. Besides the magnetic field, the effects of the booster should be studied further. When a second frequency is being fully implemented it might be that the booster is not longer needed or not with the current detuning. The optimal combination of second frequency detuning and booster detuning is likely not to be the same as for booster and MOT. However, the interaction of the booster and the second frequency is not clear and should be further investigated. After the effects on ^{39}Ar are clear, the double frequency MOT could become a standard tool at the ArTTA apparatus. For this case another laser beam would have to be generated since the second repumper which was used for the measurements in this thesis is necessary for the operation of ArTTA with ^{39}Ar. It would be the next step to observe the effect of a second frequency on the single atom detection of ^{39}Ar. Here the cloud never gets dense and we mostly have only one atom in our trap. Therefore two-body losses do not occur.

Appendix A

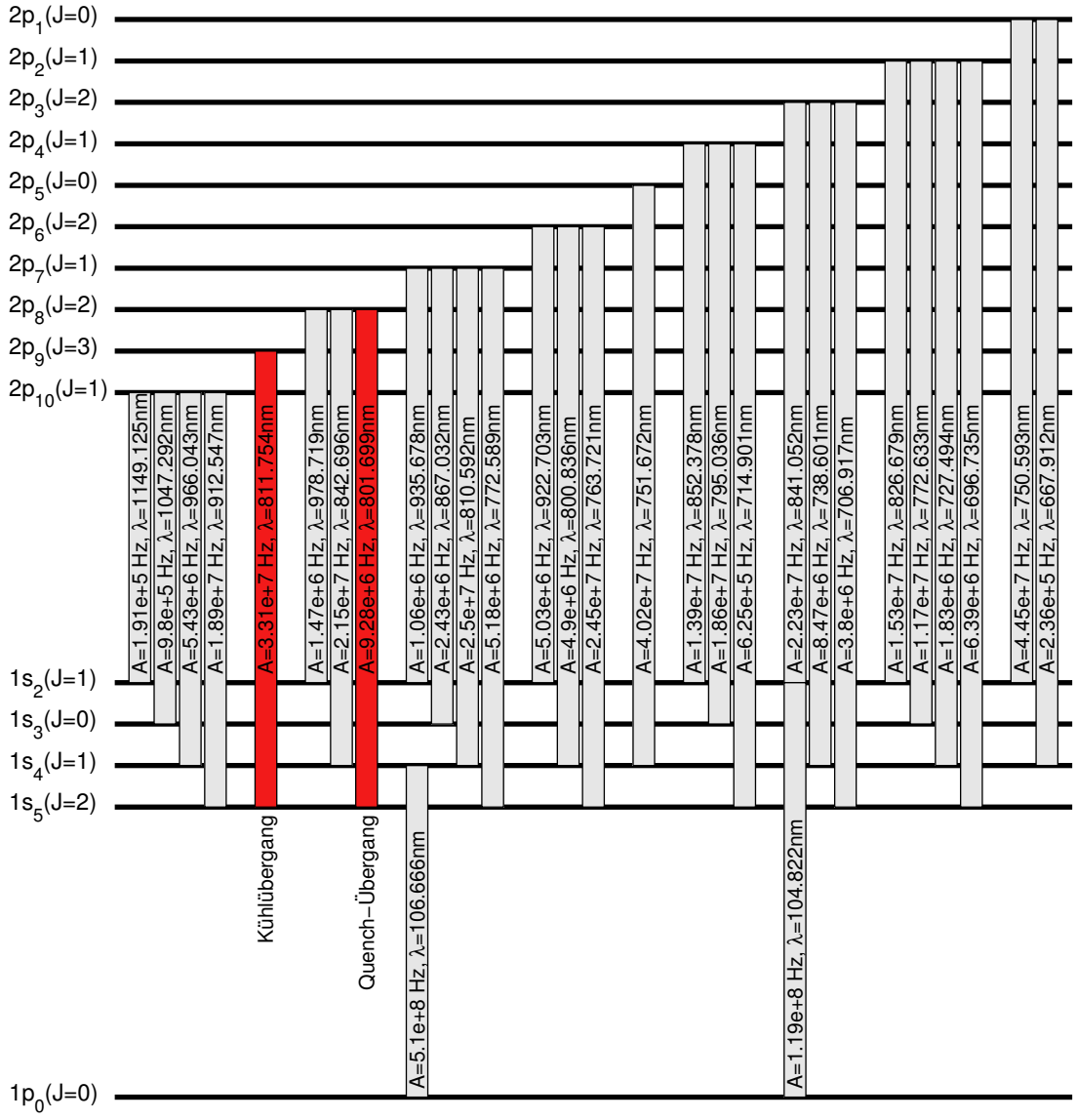

Figure 6.1: A detailed scheme of the transitions in ^{40}Ar. Taken from [32].

Appendix B

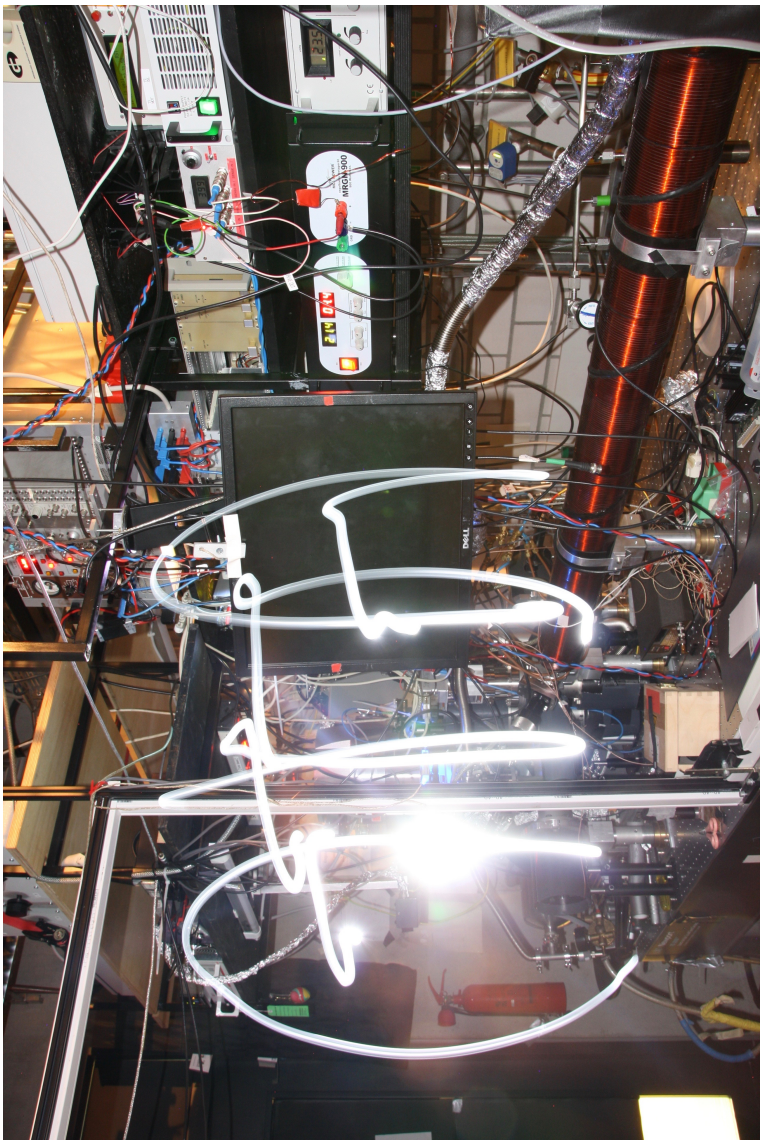

Figure 6.2: Image of the ATTA machine, shown in red is the Zeeman slower's copper coil. Arty flashlight writing 'ATTA' done by the author.

Appendix C

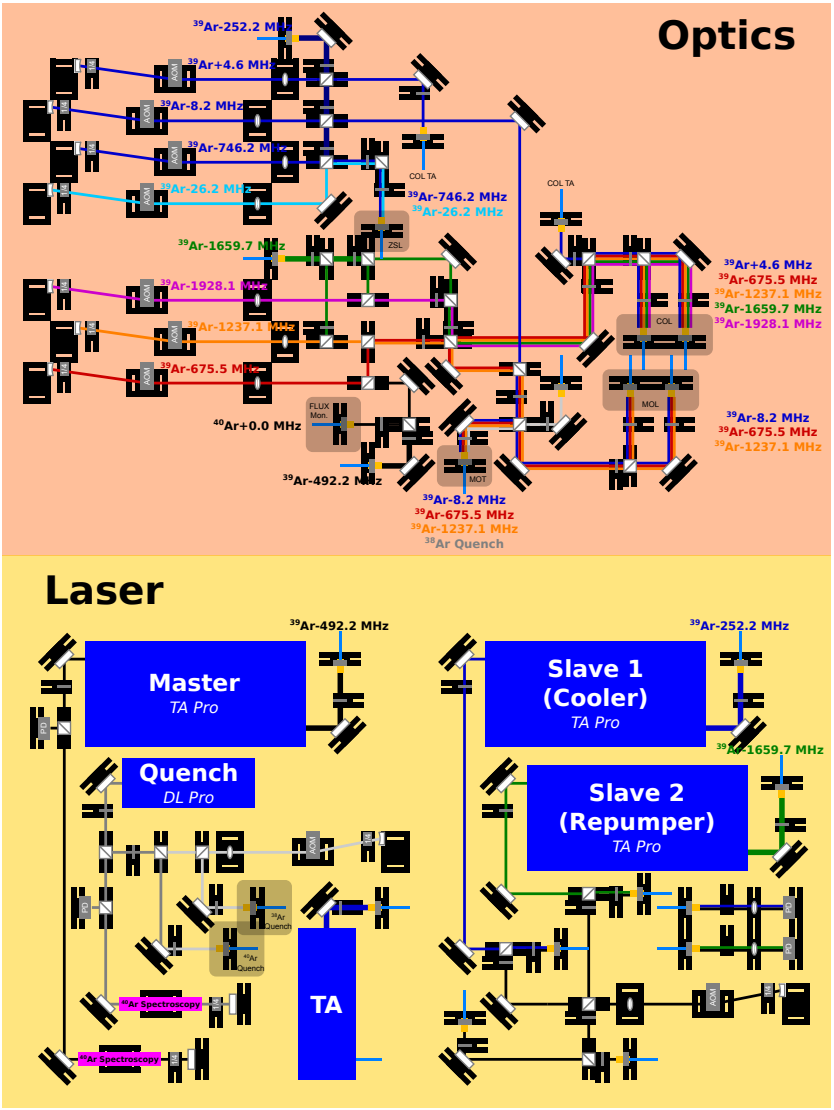

Figure 6.3: Setup of the new ArTTA laser system with only commercial laser solutions. Similar to current ATTA system with a TA Pro as master, instead of DL Pro/ TA combination and DL Pro instead of self-built quench ECDL.

Bibliography

[1] *World Health Organization: Water Resources*. Website. online `http://www.who.int/water_sanitation_health/resources/en/`; 29.05.2016.

[2] *The United Nations Inter-Agency Mechanism on all Freshwater related Issues*. Website. online `http://www.unwater.org/`; 29.05.2016.

[3] Charles R. Fitts. *Groundwater Science*. 2. Auflage. Amsterdam, Boston: Academic Press, 2013. ISBN: 978-0-123-84705-8.

[4] Florian Ritterbusch. *Dating of groundwater with Atom Trap Trace Analysis of* ^{39}Ar. PhD Thesis. Universität Heidelberg, 2013.

[5] J.A. Corcho Alvarado et al. *Constraining the age distribution of highly mixed groundwater using 39Ar: A multiple environmental tracer (*$^{3}H/^{3}He$, ^{85}Kr, ^{39}Ar, *and* ^{14}C*) study in the semiconfined Fontainebleau Sands Aquifer (France)*. In: *Water Resources Research* 43.3 (2007).

[6] Gholam A. Kazemi, Jay H. Lehr, and Pierre Perrochet. *Groundwater age*. John Wiley & Sons, 2006.

[7] P. Collon, W. Kutschera, and Z.-T. Lu. *Tracing noble gas radionuclides in the environment*. In: *arXiv preprint nucl-ex/0402013* (2004).

[8] Donald Porcelli. *Noble gases in geochemistry and cosmochemistry*. 1. Auflage. 2002.

[9] H.H. Loosli. *A dating method with* ^{39}Ar. In: *Earth and Planetary Science Letters* 63.1 (1983), pp. 51–62.

[10] P. Collon et al. *Development of an AMS method to study oceanic circulation characteristics using cosmogenic* ^{39}Ar. In: *Nuclear Instruments and Methods in Physics Research Section B: Beam Interactions with Materials and Atoms* 223 (2004), pp. 428–434.

[11] W. Jiang et al. *An atom counter for measuring* ^{81}Kr *and* ^{85}Kr *in environmental samples*. In: *Geochimica et Cosmochimica Acta* 91 (2012), pp. 1–6.

[12] F. Ritterbusch et al. *Groundwater dating with Atom Trap Trace Analysis of* ^{39}Ar. In: *Geophysical Research Letters* 41.19 (2014), pp. 6758–6764.

[13] H.H. Loosli et al. *Ten years low-level counting in the underground laboratoryin in Bern, Switzerland*. In: *Nuclear Instruments and Methods in Physics Research Section B: Beam Interactions with Materials and Atoms* 17.5-6 (1986), pp. 402–405.

[14] D. Acosta-Kane et al. *Discovery of underground Argon with low level of radioactive ^{39}Ar and possible applications to WIMP dark matter detectors*. In: *Nuclear Instruments and Methods in Physics Research Section A: Accelerators, Spectrometers, Detectors and Associated Equipment* 587.1 (2008), pp. 46–51.

[15] J. R. Tuniz et al. *Accelerator Mass Spectrometry - Ultrasensitive Analysis for Global Science*. Boca Raton, Fla: CRC Press, 1998. ISBN: 978-0-849-34538-8.

[16] P. Collon et al. *^{81}Kr in the Great Artesian Basin, Australia: a new method for dating very old groundwater*. In: *Earth and Planetary Science Letters* 182.1 (2000), pp. 103–113.

[17] Anika Frölian. *Optisches Pumpen über das transiente 2p6-Niveau zur Erhöhung der Dichte von metastabilem Argon in einer RF-Gasentladung*. Bachelor Thesis. Universität Heidelberg, 2015.

[18] Maurus Hans. *Optisches Pumpen zur Erhöhung der Dichte von metastabilem Argon in einer RF-Gasentladung*. Bachelor Thesis. Universität Heidelberg, 2014.

[19] Zhongyi Feng. *Observation and Characterization of the Bichromatic Force on Metastable Argon-40*. Master Thesis. Universität Heidelberg, 2014.

[20] Harold J. Metcalf and Peter van der Straten. *Laser Cooling and Trapping*. Springer, 2012.

[21] *Isidor Isaac Rabi*. Website. online `https://en.wikipedia.org/wiki/Isidor_Isaac_Rabi`; 18.05.2016.

[22] Karl Blum. *Density Matrix Theory and Applications*. 3rd ed. 2012. Berlin Heidelberg: Springer, 2012.

[23] Marlan O. Scully and M. Suhail Zubairy. *Quantum Optics*. 6th ed. Cambridge: Cambridge University Press, 2008.

[24] Wolfgang Demtröder. *Experimentalphysik 3*. Springer, 2010.

[25] B.H. Bransden and C.J. Joachain. *Physics of Atoms and Molecules*. 01. Aufl. Amsterdam: Pearson Education, 2003. ISBN: 978-0-582-35692-4.

[26] Peter F. Bernath. *Spectra of Atoms and Molecules*. New York: Oxford University Press, 1995.

[27] Steven Chu. *The manipulation of neutral particles*. Nobel lecture. 1998.

[28] William D. Phillips. *Laser cooling and trapping of neutral atoms*. Nobel lecture. 1998.

[29] Tim Sharp. *Earth's Atmosphere: Composition, Climate and Weather*. Website. online `http://www.space.com/17683-earth-atmosphere.html`; 18.04.2016.

[30] Mark Csele. *Fundamentals of Light Sources and Lasers, Chapter 3 Notes*. Website. online `http://archive.is/pwve`; 18.04.2016.

[31] Florian Ritterbusch. *Realization of a collimated beam of metastable atoms for ATTA of Argon 39*. Diploma Thesis. Universität Heidelberg, 2009.

[32] Sven Ebser. *Optimierung und Stabilisierung von ^{39}Ar-ATTA bis hin zur erstmaligen Anwendung auf die Datierung natürlicher Wasserproben*. Diploma Thesis. Universität Heidelberg, 2012.

[33] Christoph Kaup. *Single-Atom Detection of ^{39}Ar*. Diploma Thesis. Universität Heidelberg, 2011.

[34] J. Welte et al. *Towards the realization of atom trap trace analysis for ^{39}Ar*. In: *New Journal of Physics* 12.6 (2010), p. 065031.

[35] Joachim Welte. *Atom Trap Trace Analysis of ^{39}Ar*. PhD Thesis. Universität Heidelberg, 2011.

[36] C.J. Hawthorn, K.P. Weber, and R.E. Scholten. *Littrow configuration tunable external cavity diode laser with fixed direction output beam*. In: *Review of scientific instruments* 72.12 (2001), pp. 4477–4479.

[37] L. Ricci et al. *A compact grating-stabilized diode laser system for atomic physics*. In: *Optics Communications* 117.5 (1995), pp. 541–549.

[38] Y. Xiong et al. *Design and characteristics of a tapered amplifier diode system by seeding with continuous-wave and mode-locked external cavity diode laser*. In: *Optical Engineering* 45.12 (2006), pp. 124205–124205.

[39] J.C.B. Kangara et al. *Design and construction of cost-effective tapered amplifier systems for laser cooling and trapping experiments*. In: *American Journal of Physics* 82.8 (2014), pp. 805–817.

[40] D. Voigt et al. *Characterization of a high-power tapered semiconductor amplifier system*. In: *Applied Physics B* 72.3 (2001), pp. 279–284.

[41] Matthias Henrich. *Design and Realization of a Laser System for ATTA of Argon 39*. Diploma Thesis. Universität Heidelberg, 2010.

[42] Maximilian Prüfer. *Aufbau eines temperaturstabilisierten optischen Verstärkers*. Project Report. 2013.

[43] H. O. Back et al. *First large scale production of low radioactivity argon from underground sources*. In: *arXiv preprint arXiv:1204.6024* (2012).

[44] Sven Ebser. *Dating with Atom Trap Trace Analysis of ^{39}Ar*. Talk. at TANGR 2015, Heidelberg.

[45] C.F. Cheng et al. *Normalization of the single atom counting rate in an atom trap*. In: *Optics letters* 38.1 (2013), pp. 31–33.

[46] K. Sengstock and W. Ertmer. *Laser manipulation of atoms*. In: *Advances in Atomic, Molecular, and Optical Physics* 35 (1995), pp. 1–44.

Acknowledgments

Diese Arbeit wäre ohne die Unterstützung vieler Menschen nicht möglich gewesen und jede*r Einzelne verdient ein großes Dankeschön zum Abschluss. Besonders bedanken möchte ich mich bei:

- Markus K. Oberthaler, der diese Arbeit betreut und ermöglicht hat und immer wieder motivierende Worte gefunden hat.

- Selim Jochim dafür, dass er der Zweitkorrektur zugestimmt hat.

- Werner Aeschbach für die Mitbegründung von ATTA in Heidelberg und für seine positive Einstellung zu jeder Zeit.

- Stefan Beyersdorfer und Florian Ritterbusch für die schöne und hilfreiche Zusammenarbeit mit dem Institut für Umweltphysik.

- Meinen ATTA-Kollegen Sven Ebser und Zhongyi Feng die mich ganz wunderbar im Team aufgenommen haben und eine ganz großartige Betreuungsarbeit geleistet haben. Danke für euer massives Korrekturlesen und das Interesse für ATTA, das ihr in mir geweckt habt. Danke auch an die neue ATTA-Generation, vor allem Andreas Kamrad fürs Lesen dieser Arbeit.

- Allen Matterwavern! Ihr seid eine außergewöhliche Gruppe und euer Zusammenhalt und euer gebündeltes Wissen hat mich jeden Tag mehr beeindruckt. Danke für das schwesterliche Teilen der Laborausstattung (Der Agilent-Tower wäre ohne euch nicht möglich gewesen!) und Hilfe bei jeglichen Fragen. Ich bin fest davon überzeugt, dass wir die beste KIP-Weihnachtsfeier aller Zeiten organisiert haben!

- Christiane und Dagmar, die ihr Organisationstalent immer wieder effektiv eingebracht haben. Danke für die Hilfe bei diversen Haushiwi-Angelegenheiten!

- Meiner Pubquiz Gang, Robin and his Hoodies, Kartoffel"käfer", Octittagon, Rrrrrawberries... -wie ihr auch heißt! Danke, dass ihr mich immer wieder ins Leben integriert habt. Ich bin so glücklich jeden einzelnen von euch getroffen zu haben! XOXO

- Paul Heeren, der sich jeden Abend (mehr oder weniger geduldig) meine aufgeregten Erzählungen aus dem Labor angehört hat. Ich bin unendlich froh, dass es dich gibt.

- Meiner Familie in Ostfriesland (und in Speyer) für das unerschütterliche Bodenständig-, Entspannt- und Offensein. Ganz besonders danke ich Meta und Melle Ringena, die niemals aufgehört haben mich zu unterstützen und mir beigebracht haben, dass man Alles schaffen kann, was man sich vornimmt. Ihr habt mir immer freie Hand bei allen meinen Entscheidungen gelassen, was bestimmt nicht immer ganz einfach war. Danke für Alles.
- Allen Menschen, die mich gefördert, gefordert und unterstützt haben.

Erklärung:

Ich versichere, dass ich diese Arbeit selbstständig verfasst habe und keine anderen als die angegebenen Quellen und Hilfsmittel benutzt habe.

Heidelberg, den (Datum) .....